Advanced Modeling of Nanoparticle Nucleation
Towards the simulation of particle synthesis

A DISSERTATION
SUBMITTED TO THE FACULTY OF THE GRADUATE SCHOOL
OF THE UNIVERSITY OF MINNESOTA
BY

Jun Liu

IN PARTIAL FULFILLMENT OF THE REQUIREMENTS
FOR THE DEGREE OF
Doctor of Philosophy

Prof. Sean C. Garrick

November, 2012

Acknowledgements

I am grateful to my advisor, Prof. Sean Garrick, for the support and guidance without which this dissertation would never be possible. The last four years at the Computational Transport Phenomena Laboratory are fulfilled with challenges and opportunities, which are unforgettable in the years to come. I am truly indebted and thankful to my committee members: Prof. Peter McMurry, Prof. Steven Girshick, and Prof. Ellen Longmire. Any attempts to list their generous helps with which this dissertation and my life has been richly blessed would be hard to achieve in only a few words.

I wish to thank my colleagues in the lab for their help. There are many people who have eared my gratitude for their contribution to my time in graduate school. I gratefully acknowledge Dr. Guanghai Wang for his kind introduction to this field and continuous support during my years of study. I also wish to acknowledge Minnesota Institute of Supercomputing for providing the access and support to the nice and useful resources.

Most importantly, to my parents who love me unconditionally and provide examples of hard working, honest, responsible with pride, and inspired me by telling me to keep true to the dreams of my youth. Now I've achieved our dreams and I wish to dedicate this work to you all; to who have supported me through the darkest times and believed in me when I was doubtful. No words can express how grateful I am and how much I appreciate, that you have made the past a few years the best of my life.

Dedication

To all who have loved and supported me, my gratitude is beyond words

Abstract

Nanotechnology holds a lot of promise for the discovery of new phenomena, and many of the envisioned processes involve nanoparticles. These particles are found in chemical sensors, drug targeting and delivery, and one important application is motivated by the need of clean renewable energy sources. The very first step of gas-to-particle conversion as homogeneous nucleation in flow systems plays an essential role in a variety of natural and industrial processes of nanoparticle synthesis. In this work, nucleation processes of several metal materials and dibutyl phthalate (DBP) nanoparticles in laminar and turbulent flows are investigated via direct numerical simulations (DNS). The flows consist of condensing vapor diluted in argon or nitrogen issuing into a cooler particle-free stream. DNS facilitates probing the interactive effects of fluid dynamics and nucleation in an accurate manner. The fluid, thermal and chemical fields are governed by the Navier-Stokes, enthalpy, and mass transport equations. Nucleation is simulated via calibrated classical homogeneous nucleation models. Recently developed size dependent surface tension model offers increased accuracy in predicting metal particle nucleation. This approach is attractive in that it promises to be more accurate than the classical nucleation theory while maintaining much of its simplicity when coupling with fluid dynamics. The effects of flow turbulence on metal nucleation are also studied via fully resolved DNS to elucidate the effects of different stages of fluid mixing on metal particle nucleation. The effects of nucleation on fluid dynamics are investigated via DNS of DBP nucleation within both laminar and turbulent jet flows. The simulations provide a demonstration of how heat release affects the interactions of fluid dynamics and nucleation at different Reynolds numbers and particle formation rates. The results provide insights into the interaction of fluid, thermal transport and nanoparticle nucleation in various flows, which stimulate development of models that will allow engineers to optimize the fluid and thermal environments for industrial nanoparticle production. For brevity, specific conclusions are provided in each chapter.

Contents

List of Tables

List of Figures

Chapter 1

Overview

Nanotechnology spreads in various scientific and industrial applications, driven by the unique physical properties of nanoparticles due to their high surface-to-volume ratio [4, 5, 6, 7]. In a wide variety of nanoparticle synthesis techniques, the gas-to-particle conversion is favored because of its simplicity and broad applications [8, 9, 10, 11, 12]. The objective of this work is to obtain a more physically accurate understanding and description of nanoparticle nucleation in complex flows.

The first step is to examine variations of condensing materials' properties at micro-scale [13, 14]. For example, the surface energy of critical nuclei is not necessarily based on the bulk value of material's surface tension [15, 3]. Surface energy is a widely accepted concept in describing nanoparticle nucleation processes [16]. The second step is to probe the effects of fluid dynamics interacting with nucleation processes [17]. Homogeneous nucleation is sensitive to thermal and chemical variation and it is difficult to separate the individual effects of variables [18, 19]. Numerical techniques can provide insights into such processes and analyze the different stages of particle formation separately [20, 21]. More importantly, numerical methods can be used to characterize nucleation within different types of flows by elucidating the underlying dynamics, such as the effects of turbulent mixing and flow development [22, 23]. Recently, simulation has show promise in investigating such complex processes [24, 25, 26, 21]. Reynolds-average Navier-Stokes (RANS) simulation is a popular numerical method to calculate flow fields for particle-fluid systemsbecause of its high efficiency [27]. However, RANS equations are time-averaged and not able to capture evolutions of nanoparticle with respect to

time. Large eddy simulations (LES) have also been widely used to describe the process, however it cannot resolve the small scale processes which could be of great importance [28]. Direct numerical simulation (DNS) is favored because it is more accurate due to the lack of turbulence models [29, 30, 26]. This particular field sparks interests, not only because of its great importance to research investigations and industrial applications, but also since it shows a promising perspective to nanotechnology [6, 7].

In this work I will combine numerical methods with the currently available physical models to probe the formation of nanoparticles in complex flow systems via homogeneous nucleation. Specifically, the work consists of the following parts:

Chapter 2 is devoted to examine the size effects of surface tension on metal nucleation by introducing a recently developed calibration to the classical homogeneous nucleation model [15, 3].

Chapter 3 is focused on using the calibrated model to examine its effects on metal nanoparticles formation within laminar flows. Only homogeneous nucleation process is been considered and particles are formed at the critical particle sizes [22].

Chapter 4 establishes nanoparticles formation processes within turbulent flows using the calibrated model. The interplays between fluid dynamics, thermal and particle fields in nucleation flows are significant challenges and essential to assess the effect of fluid turbulence.

Chapter 5 examines effects of nucleation heat release on the homogeneous dibutyl-phthalate nucleation within laminar planar jets. Thermal-fluid coupling is critical to the fluid dynamics and nucleation interaction. However, it is usually neglected or decoupled in previous studies.

Chapter 6 examines the effects of heat release on dibutyl-phthalate homogeneous nucleation within turbulent planar jets. Simulations are carried out to study the development of flow turbulence, and evaluate the results of different stages of flow mixing.

Chapter 2

Effects of size-dependent surface tension on metal nucleation

Recent developments from several experiments show that size dependency of surface tension is essential in better describing the formation of small nanoparticles. A. A. Onischuk *et al.* (2006) derived a homogeneous nucleation rate expression for various metals that account for the effects of size-dependent surface tension on critical, or nucleating, diameter [3]. The surface tension for zinc is shown in Fig. 2.1. This is an important factor as metal nanoparticles find many industrial applications [31, 32].

The nucleation rate J, which is the number of critical clusters formed per unit volume and time, is given by

$$J = K_0 \exp\left(-\frac{W_{crit}}{k_B T}\right), \tag{2.1}$$

where K_0 is a pre-exponential factor, and W_{crit} is minimum work required to form critical nuclei. k_B is the Boltzmann's constant and T represents the temperature. In Gibbs theory of capillarity, W_{crit} is given by

$$W_{crit} = \frac{4\pi R_s^2 \sigma\left(R_s\right)}{3}, \tag{2.2}$$

where R_s is the critical radius of the cluster with size-dependent surface tension $\sigma(R_s)$. In classical nucleation theory (CNT), surface tension σ is usually adopted as the planar value σ_∞ without curvature effects been considered. However, the calibrations with

size and curvature effects of surface tension are necessary in quantitatively describing the nanoparticle formation processes more accurately. Account for the pre-exponential factor in a single-component system,

$$K_0 = 2R_e^2 \left(\frac{\rho Y_m}{m_m}\right)^2 \left(\frac{X}{m_m}\right)^{1/2}, \tag{2.3}$$

where R_e is radius of the an equimolar surface without size dependency of the surface tension, ρ is the fluid density and Y_m is the mass fraction of the condensing vapor,m_m is the mass per molecule. The parameter X is defined as

$$X = -\left(\frac{d^2W}{dg^2}\right)_{g=g_{crit}}, \tag{2.4}$$

where g and g_{crit} are numbers of condensing molecules in the cluster and critical nuclei, respectively. The reversible work needed to form a non-critical cluster is given by

$$W = \sum_i N_i^\beta \left(\mu_i^\beta - \mu_i^\alpha\right) - V^\beta \left(P^\beta - P^\alpha\right) + \gamma A, \tag{2.5}$$

where P and μ are pressures and chemical potentials of hypothetical homogeneous phases $\alpha(vapor)$ and $\beta(liquid)$ respectively. N_i^β and V^β are the number of molecules and volume of a cluster, γ and A are the surface tension and surface area of a non-critical cluster.

A. A. Onischuk *et al.* (2006) derived a homogeneous nucleation rate expression as a function of particle sizes [3]. The relation of surface tension $\sigma(R_s)$ on particle's radius R_s is given by the following differential equation

$$\frac{d\left[\ln \sigma(R_s)\right]}{d\left[\ln R_s\right]} = \frac{\left[2\delta(R_s)/R_s\right]\left[1 + \delta(R_s)/R_s + \frac{1}{3}\left(\delta(R_s)/R_s\right)^2\right]}{1 + \left[2\delta(R_s)/R_s\right]\left[1 + \delta(R_s)/R_s + \frac{1}{3}\left(\delta(R_s)/R_s\right)^2\right]}, \tag{2.6}$$

where the Tolman length $\delta(R_s)$ is defined as [15]

$$\delta(R_s) = R_e - R_s, \tag{2.7}$$

an empirical relation of $\delta(R_s)$ on particle size is given by

$$\delta(R_s) = \frac{A}{R_s} + B, \tag{2.8}$$

where A and B are constants, which depend on specific materials and are determined from experiments [3]. The size-dependent surface tension $\sigma(R_s)$ is then given by

$$\sigma\left(R_s\right) = \sigma_\infty \exp\left(-\frac{2\delta\left(2R_s\right)}{R_s}\left(1 - \frac{\delta\left(2R_s\right)}{R_s}\beta\right)\right), \tag{2.9}$$

where σ_∞ is the planar surface tension, which could be a function of temperature T, and the function β is given by

$$\beta = 1 - \frac{1}{2}\left(\frac{\delta_\infty \delta(1.5R_s)}{\delta^2(R_s)}\right). \tag{2.10}$$

The nucleation rate expression with size-dependent surface tension can now be derived as the detailed procedure is described by A. A. Onischuk *et al.* (2006)[3]. However, in the original article there is a mathematical omission when deriving the final result. The physical significance of the omission depends on the critical, or nucleating radius, and the metal under consideration. In the Eq. (44) of the paper by A. A. Onischuk *et al.* the authors reach the expression for homogeneous nucleation of

$$J = \left(\frac{\rho Y_m}{m_m}\right)^2 \sqrt{\frac{2m_m\sigma}{\pi}}\frac{1}{\rho}\frac{R_e}{R_S}\exp\left(-\frac{4\pi\sigma {R_s}^2}{3k_BT}\right), \tag{2.11}$$

the authors then proceed to utilize the correction factor of Reiss *et al.* and the Kelvin equation [33, 16],

$$K_R \approx \frac{1}{n_1\sqrt{k_BT\kappa V_g}} \tag{2.12}$$

where n_1 is the number concentration of nucleating species, $V_g = 4\pi R_e^3/3$ is volume based on the equimolar radius, and κ is the iso-thermal compressibility. The critical size of the nuclei is given by the Kelvin relation

$$\ln(S) = \frac{2\sigma m_m}{k_BT\rho_m R_S}. \tag{2.13}$$

The resulting equation should be

$$J = \frac{n_1}{2\pi R_S}\sqrt{\frac{3\ln S}{\rho\kappa}}\sqrt{\frac{R_S}{R_e}}\exp\left(-\frac{16\pi m_m^2}{3\rho^2\left(\ln S\right)^2}\left(\frac{\sigma}{k_BT}\right)^3\right). \tag{2.14}$$

Compared to Eq. (45) in A. A. Onischuk *et al.* (2006), a factor of $\sqrt{R_S/R_e}$ is missing[3]. Instead, their equation appears as

$$J = \frac{n_1}{2\pi R_s}\sqrt{\frac{3\ln S}{\rho\kappa}}\exp\left(-\frac{16\pi m_m^2}{3\rho^2\left(\ln S\right)^2}\left(\frac{\sigma}{k_BT}\right)^3\right). \tag{2.15}$$

This omission may be very important and its effect can be shown by considering Eq. (49) Onischuk *et al* (2006), rewritten slightly,

$$\frac{R_S}{R_e} = \left(1 + \frac{\chi}{R_S^2} + \frac{\delta_\infty}{R_S}\right)^{-1}. \tag{2.16}$$

Plots of R_S/R_e are shown for Zn, Mg, Ag, and Li in Fig. 2.2. It is only near the nucleating size that the ratio is significant. In the nucleation of zinc for solar thermal processing, for example, particles containing 60 molecules are not unusual [34]. The value is as high as $R_S/R_e = 100$, for all of the metals considered, which means that the correction, $\sqrt{R_S/R_e}$, could be significant in the modeling and simulation of metal nanoparticle formation and growth dynamics.

The comparison of the size-dependent surface tension nucleation model with physical data and other nucleation models for lithium are shown in Fig. 2.3(a). The scalar points represent the size-dependent surface tension nucleation model, and the prediction of both CNT and SNT are presented in the same figure. The circles show the physical data obtained from laminar diffusion chambers, which are the critical saturation ratios to reach certain transitional nucleation rate [1]. The results indicate the critical saturation ratio S verses temperature T to reach certain steady nucleation rate $J_s = 10^9/(cm^3 \cdot s)$. At $T \leq 1000K$, CNT fails to provide an accurate relation between the saturation ratio and temperature. For example, at $T \approx 900K$, the saturation ratio $S \approx 18$ required by CNT is one order of magnitude less than the physical data $S \approx 200$. The underestimation of required saturation ratio means less lithium nanoparticles are physically formed than predicted by CNT. At the above temperatures, SNT yields a better correlation with physical data since the critical conditions are chosen within the same range ([1]). At higher temperatures ($T > 1000K$), CNT gives an improved prediction where the SNT has a systematic drift of overestimating the saturation ratio. For example, at $T \approx 1100K$, though the available experimental results are limited, the prediction of S via SNT ($S \approx 30$) is about twice of the physical data ($S \approx 15$). The simulation data using size-dependent surface tension nucleation model show advantages in correlating with physical data. At higher temperatures ($T > 1000K$), the simulation results are close to what the CNT has predicted for the critical saturation ratios at certain temperature. At lower temperature ($T \leq 1000K$), the model predicts the correlation of S and T comparable to what the SNT has predicted.

Similar results are observed for zinc and magnesium nucleation. Zinc nucleation is shown in Fig. 2.3(b), where SNT is not available due to limited physical data. Magnesium nucleation is shown in Fig. 2.3(c), where CNT cannot be located within the same figure. Within the temperature range been considered for zinc ($650K < T < 750K$), CNT overestimated the required saturation ratio to reach nucleation rate $J_s = 10^{10}/(cm^3 \cdot s)$. For example, at $T = 700K$, CNT predicts $S \approx 10^3$, which is two orders of magnitude higher than actual physical data ($S \approx 10$). The simulation results using size-dependent surface tension nucleation model, on the other hand, correlates well with physical data within the same temperature range. Comparison of zinc and lithium nucleation shows that CNT underestimates the zinc nucleation rate and overestimates lithium nucleation rate. Previous research shows that for small particles ($d_p \sim 1nm$), zinc surface tension is overestimated ($\sigma_{Zn}(d_p, T) < \sigma_{Zn}(T)$), when lithium surface tension is underestimated ($\sigma_{Li}(d_p, T) > \sigma_{Zn}(T)$) ([3, 35]). The size-dependent surface tension is a critical for many metal nucleations in which particles being formed are of small sizes, such as lithium and zinc. For magnesium nucleation, SNT and the size-dependent surface tension nucleation model both provide satisfactory predictions of S verses T against physical data. However due to the limitations of SNT where a critical reference point of temperature T_{cr} and saturation ratio S_{cr} need to be indicated prior to calculations, the latter is computationally economic and efficient, and capable of being extended to a broad range of materials.

In this work the size-dependent surface tension nucleation model is evaluated by comparison with CNT and other available nucleation models. It promises to be more accurate in correlating the particle production rate with critical saturation ratios [3, 22]. B keeping the simple form of classical nucleation expression, it is also committed to compatibility, computational efficiency while maintaining the ease with which it can be implemented in computational fluid dynamics.

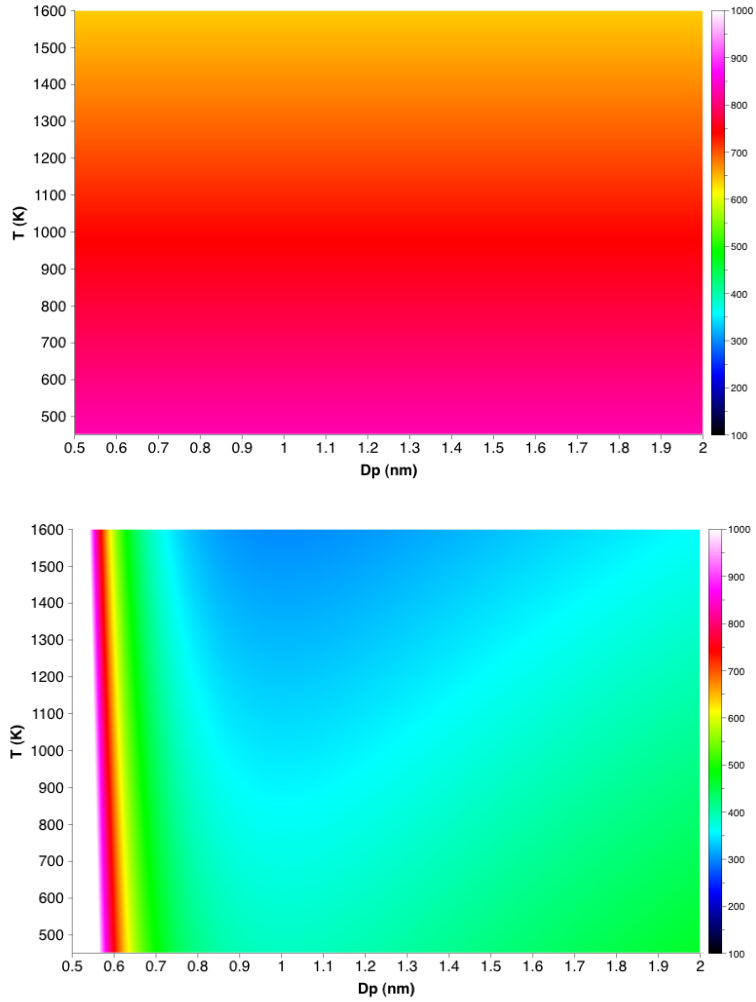

Figure 2.1: Surface tension of zinc nanoparticles varying with temperature and particle size. Left: size-independent; Right: size-dependent.

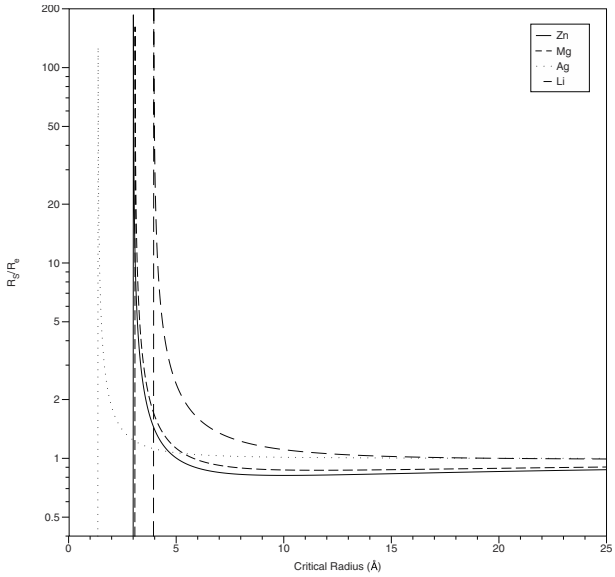

Figure 2.2: The ratio of R_S/R_e as a function of critical radius R_S for various metals.

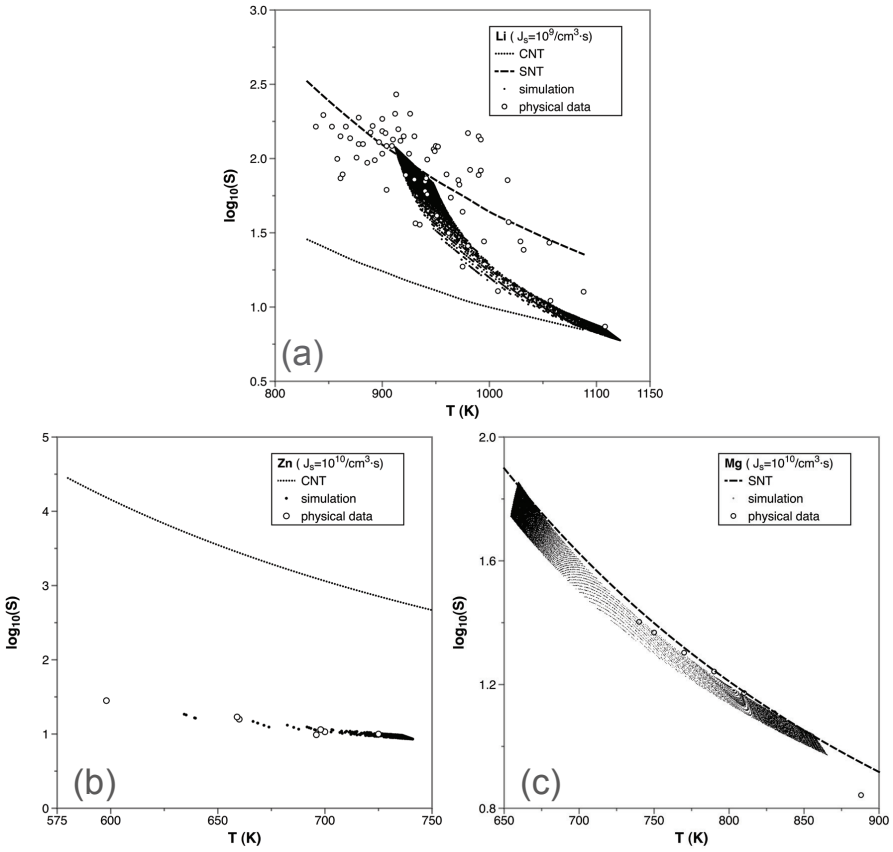

Figure 2.3: Vapor saturation ratio vs. temperature: (a) lithium; (b) zinc; and (c) magnesium. Comparison of simulation results, CNT, SNT and physical data [1, 2, 3].

Chapter 3

Metal particle nucleation in laminar jets

Recently developed surface tension model have taken size-dependency of surface tension into account, which offers significantly increased accuracy in modeling of metal particle nucleation. These models facilitate the probing the effects of fluid, scalar, and thermal transport on nucleation in an accurate manner. In this work we investigate the formation of metal nanoparticles in laminar flows. The flows consist of metal vapor diluted in argon issuing into a cooler argon stream. The fluid, thermal and chemical fields are obtained via solving the Navier Stokes, enthalpy, and mass-fraction transport equations while nucleation is simulated via a homogeneous nucleation model with size-dependent surface tension. This approach is attractive in that it promises to be more accurate than classical nucleation theory (CNT) while maintaining much of its simplicity when coupling with fluid dynamics. The results show that the size-dependent surface tension nucleation model is more accurate than CNT and agrees well with physical data. Physically, the sensitivity of the saturation ratio to changes in temperature is shown to be greater than its sensitivity to mass-fraction, highlighting the significance of differential molecular transport of energy and mass and the significance of non-unity Lewis numbers. More significantly, the size-dependent surface tension approach suggests that certain metals may have a maximum nucleation rate and further cooling — a strategy employed to increase particle nucleation rates — will actually decrease particle nucleation.

3.1 Introduction

The formation of particles from vapor is a challenging problem of interest to scientists and engineers working in a variety of areas and disciplines. [17, 36, 37, 38]. For example, the need for sustainable energy sources has motivated studies of metal nanoparticles synthesis for hydrogen production [5, 39, 40]. Aerosol technologies, or gas-phase synthesis have long been basic research tools to study gas-to-particle conversion, as well as a favored avenue for industrial manufacture of nanoparticles with optimized physical and chemical properties [41, 42]. The formation of particles is highly sensitive to local temperature and condensing vapor concentration. Classical nucleation theory (CNT) assumes a steady state rate of particle formation given the local vapor concentration and temperature. This rate is determined by the balance of molecular kinetic energy and the surface energy of a cluster being formed [43, 44]. CNT is attractive in part because it provides a simple expression based on thermodynamic properties that predicts nucleation rates. However, the accuracy of CNT is questionable as property values are extended from bulk down to molecular clusters without modification. Studies have shown the variation is significant for various materials. In flows with thermo-physical coupling – such as condensing nozzles – the interaction between surface tension, temperature and mass-fraction may be significant [45].

Previous research has shown that several material properties are strong functions of size when approaching the nano-scale [15, 46, 13, 47, 48, 49]. Recently, Onischuk, *et al.*(2006) evaluated the surface tension of several metal vapors as a function of particles' sizes from the nucleation rate and supersaturation ratio [3]. Their model is derived from physical data, based on the Tolman length/formula and suggests that the materials considered exhibit a strong dependence on particle radius when the sizes of particles being formed are in 0.5 to 1.5 nanometer range. Such models offer a promising path to probe the effects of transport – fluid, scalar, and thermal – on particle formation via numerical simulation. Though more detailed descriptions of the particle formation processes are available, coupling them with the underlying fluid dynamics is not straightforward. Approaches such as molecular dynamics or dynamic nucleation techniques are able to successfully describe nucleation processes at the molecular scale [20, 50]. These result in improved predictions/accuracy when compared to physical data as well as richer physics

as they benefit from the resolution of molecular-scale kinetics. However, the difficulty associated with extending the techniques to the length and time-scales present in practical systems renders them inadequate [51, 24, 52, 53].

In this work we utilize direct numerical simulation in conjunction with the recently-developed size-dependent surface tension model to predict the nucleation of metal nanoparticles in laminar flows [3, 35]. We simulate the nucleation of lithium, zinc, and magnesium nanoparticles and assess the aforementioned model against physical data, as well as the predictions of CNT and scaled nucleation theory. This allows the determination of the range of the physical applicability of the models as well as what they may suggest about the formation of particles in more complex flows.

3.2 Formulation

3.2.1 Fluid and scalar transport

The flows are governed by the compressible Navier-Stokes equations. the primary variables are the flow velocity $u_i(x_i, t)$, the fluid pressure $p(x_i, t)$, fluid density $\rho(x_i, t)$ and fluid enthalpy $h(x_i, t)$. These are obtained via

$$\frac{\partial \rho u_j}{\partial x_j} = 0, \tag{3.1}$$

$$\frac{\partial \rho u_i u_j}{\partial x_j} = -\frac{\partial p}{\partial x_i} + \frac{\partial}{\partial x_j}\left[\mu\left(\frac{\partial u_i}{\partial x_j} + \frac{\partial u_j}{\partial x_i}\right) - \frac{2}{3}\mu\delta_{ij}\frac{\partial u_k}{\partial x_k}\right], \tag{3.2}$$

$$\frac{\partial \rho h u_j}{\partial x_j} = \frac{\partial}{\partial x_j}\left(\frac{k}{C_p}\frac{\partial h}{\partial x_j}\right), \tag{3.3}$$

where δ_{ij} is kronecker delta, μ is the fluid viscosity, k is the thermal conduction coefficient, and C_p is the constant pressure specific heat. The equations are closed using the ideal gas relation, $p = \rho RT$, where R is gas constant and the temperature is related to the enthalpy via $dh = C_p dT$. The flows consist of a single metal vapor diluted in a carrier gas. The transport of each species mass-fraction, Y_i, is given by

$$\frac{\partial \rho u_j Y_i}{\partial x_j} = \frac{\partial}{\partial x_j}\left(\rho D_i \frac{\partial Y_i}{\partial x_j}\right) + \dot{\omega}_i, \tag{3.4}$$

where D_i is the diffusion coefficient of species i and $\dot{\omega}_i$ is mass conversion rate (from vapor to particle) given by

$$\dot{\omega}_i = \frac{\pi}{6}\rho_i {d_p}^3 J, \tag{3.5}$$

where ρ_i is density of the condensing species, d_p is the critical particle diameter, and J represents the vapor to particle conversion rate, i.e. the nucleation rate.

3.2.2 Nucleation modeling

The particle nucleation rate J is based on CNT with the use of several correction factors. These corrections are omitted here as they are not the subject of our investigation and are found elsewhere [44, 54, 33, 35]. The rate of particle formation is given by

$$J_s = \frac{\rho Y_i}{2 m_i \pi R_S} \sqrt{\frac{3 \ln S}{\rho \kappa}} \sqrt{\frac{R_S}{R_e}} \exp\left(-\frac{16 \pi m_i^2}{3 \rho^2 (\ln S)^2} \left(\frac{\sigma}{k_B T} \right)^3 \right), \tag{3.6}$$

where m_i is mass of a vapor molecule, $\sigma(T, d_p)$ is the surface tension, d_p is the nuclei diameter, R_e is the radius of the equimolar surface, R_s is the surface radius ($R_s = d_p/2$), κ is the isothermal compressibility of the critical nuclei, and S represents the saturation ratio. The size of the critical nuclei, or the size at which particles form, is given by the Kelvin relation

$$d_p = \frac{4 \sigma m_i}{k_B T \rho_i \ln(S)}. \tag{3.7}$$

This rate expression been shown to be accurate in predicting the nucleation of a variety of metal nanoparticles [3, 35].

3.3 Results

3.3.1 Flow configuration

The flows been considered in this work consist of a three dimensional round jet of a nozzle diameter D. Jet flow with a velocity of U_o issues into a co-flowing stream with velocity U_∞. A schematic of the flow configuration is shown in Fig. 3.1. The flows are laminar and the velocity ratio is $U_o/U_\infty = 2.5$. The flows consist of a hot metal vapor stream at temperature T_o, diluted in argon issuing into a cooler co-flowing stream of argon at temperature T_∞. The mass fraction of the metal vapor is Y_o in the jet.

3.3.2 Physical parameters and assumptions

Three different metals are considered – lithium (Li), magnesium (Mg), and zinc (Zn). The momentum, thermal, and chemical transport are governed by three non-dimensional

parameters. The Reynolds number, $Re = U_o D/\nu$, is the ratio of inertial to diffusive forces; the Prandtl number, $Pr = \nu C_p/k$, is the ratio of momentum diffusivity (kinematic viscosity) to thermal diffusivity; and the Schmidt number, $Sc = \nu/D$ is the ratio of momentum diffusivity (viscosity) to mass diffusivity. A third non-independent yet illustrative parameter is the Lewis number, $Le = Sc/Pr$, which represents the ratio of thermal diffusivity to mass diffusivity. This is useful as the paths to nucleation traverse through temperature and mass-fraction space. The values of all parameters are listed in Table 3.2. All physical properties — those of the particles and the gas mixtures — are calculated based on the local mass fraction of each chemical species Y_i.[55, 56, 57] The variation of these properties with temperature is adopted from published empirical curves to ensure accuracy.[1, 2, 3] The particle density is taken to be that of the bulk material and the particle volume is calculated using $v_i = \frac{1}{6}\pi d_p^3$, where $d_p = 2R_s$. The momentum transfer between fluid and particles is assumed to be negligible due to the low volume fraction. A typical volume fraction, which is ratio of the total volume of particles to the volume of fluid mixture, is less than 10^{-7}.

Saturation ratio S is the ratio of partial pressure of the condensing vapor to the saturated pressure at certain temperature, which is critical to the nucleation process especially within flow systems. The variation of partial pressure of metal vapor reflects the transport of mass fraction, and the saturated pressure is strongly correlated to the thermal transport within the flow. The saturation ratio is given by

$$S = \frac{MW}{MW_i} \times \frac{pY_i}{p_s} \tag{3.8}$$

where MW is average molecular weight of the fluid mixture, MW_i is molecular weight of the condensing species, and p_s is the saturated vapor pressure given by $p_s = 133.32 \times 10^{C-D/T}$, where C and D are parameters dependent on the condensing species and the pressure is in units of Pascals (Pa). The surface tension is a function of temperature and nuclei diameter, which is given by

$$\sigma\left(d_p, T\right) = \sigma_T\left(T\right) \exp\left[-4\frac{\delta\left(d_p\right)}{d_p}\left(1 - \beta\frac{2\delta\left(d_p\right)}{d_p}\right)\right], \tag{3.9}$$

where $\sigma_T = C_1\left(C_2 - T\right)$ and the function β is given by

$$\beta = 1 - \frac{1}{2}\left(\delta_o \frac{\delta(3/4d_p)}{\delta^2(d_p)}\right), \tag{3.10}$$

where

$$\delta(d_p) = \frac{A}{d_p} + \delta_o, \tag{3.11}$$

and δ_o is the Tolman length and A is a constant. These values of these parameters are listed in Table 3.1 and a thorough description of the approach can be found elsewhere.[3, 35]

3.3.3 Numerical specifications

The governing equations for the flow, thermal and chemical transport are solved via a fourth order accurate hybrid MacCormack-based, predictor-corrector scheme [58, 59]. Numerical simulations are performed on a domain of $14D \times 8D \times 8D$ in x, y and z directions respectively. The resolution for all simulations is $320 \times 240 \times 240$. The results exhibited grid independence at this resolution. Each simulation was performed using 64 CPUs and required roughly 200 CPU-hours.

3.3.4 Scalar transport

From a molecular perspective, nucleation or particle formation is the result of competing energies – the kinetic energy of the colliding molecules and the surface energy that binds them together. From a fluid dynamics perspective, nucleation is about the interplay of temperature and vapor concentration. Combinations of temperature (representing the mean kinetic energy of the colliding molecules) and concentration or mass-fraction (representing the number of colliding molecules). Cross-stream profiles of the normalized zinc vapor mass fraction, $Y^{\star}_{Zn} = Y_{Zn}/Y_{Zn_o}$, and temperature, $T^{\star} = (T - T_{\infty}) / (T_o - T_{\infty})$, are shown in Fig. 3.2. The profiles in Fig. 3.2(a) show that the zinc mass-fraction decreases with downstream distance, x/D, while spreading in the cross-stream direction, r/D. This reflects the dilution of zinc as the jet spreads and mixes with the co-flowing argon stream. A similar trend is observed in the fluid temperature, shown in Fig. 3.2(b). The profiles are quite similar except that the jet temperature does not decrease as quickly as the mass-fraction. Ie. the rate of cooling is less than the rate of dilution. Along the centerline, at $x/D = 12$ the temperature is $T^{\star} = 0.71$ while the zinc mass-fraction is $Y^{\star}_{Zn} = 0.40$. These differences are largely due

to the non-unity Lewis number. For zinc, the Lewis number is $Le = 0.74$ which means that heat conduction is less than mass diffusion.

Cross-stream profiles of the saturation ratio S for lithium, zinc and magnesium vapor respectively at several downstream locations are shown in Fig. 3.3. In all flows, the saturation ratio near the jet origin is less than unity, $S < 1$. The profiles indicate that the saturation ratio increases significantly as the jets travel downstream. The increase in saturation ratio originates at the interface of the jet and co-flowing stream. This is where the hot vapor diffuses into to cooler co-flow. The effect of cooling and dilution acts to increase the saturation ratio. Specifically, cooling acts to increase S while dilution acts to decrease S. The fact that the saturation ratio increases, reflects the relative importance of cooling (compared to dilution), and the sensitivity of the saturation ratio to the fluid temperature. The profiles also show that the width of the $S > 1$ region increases with Lewis number. This suggests that the extent of the flow in which particles may nucleate is greater in the magnesium jet ($Le = 1.52$) than in the zinc jet ($Le = 0.74$). In the zinc jet, the saturation ratio is roughly $S = 250$ at $x/D = 1$ and reaches a peak value of $S = 740$ by $x/D = 12$. Similar trends are observed in the lithium and magnesium predictions. The peak values occur at specific radial locations which increase as the jet travels downstream. These results suggest that a single laminar jet maybe used to obtain nucleation data at a variety of saturation ratios. The current practice is to perform an experiment at a specific saturation value and examine/evaluate nucleation dynamics.[60, 61].

The sensitivity of saturation ratio to the mass-fraction and temperature can be observed by considering the combinations of S, T and Y throughout the domain. Scatter plots of S vs $T^\star$ and S vs $Y^\star_{Zn}$ are shown in Fig. 3.4. The scalar points are colored by the nucleation rate to convey the importance of those values on particle nucleation. For the largest rates, $10^{18} < J < 10^{22}$, the results show that changes in temperature impart greater changes in the saturation ratio than changes in mass-fraction. Consider a streamline going from $T^\star = 0.4$ to $T^\star = 0.25$. Along this streamline, Fig. 3.4(a) suggests that the saturation ratio will increase by at least 1 order of magnitude. According to 3.4(b), a similar change in mass-fraction — $Y^\star_{Zn} = 0.4$ to $Y^\star_{Zn} = 0.25$ — may result in a saturation ratio decrease or a change by a factor of one or two.

3.3.5 Model validation

Initially, the molecules collide but they do not "stick" or form stable nuclei for future growth. This is because the surface energy is not sufficient to bind the kinetic energy of the participating molecules. As the fluid travels downstream, cooling occurs via Fourier diffusion, the participating molecules are less energetic and and stable clusters form. Cross-stream profiles of the zinc nucleation rate, J_s, at four downstream locations are shown in Fig. 3.5(a). The profiles shows that the peak nucleation rate of $J_s = 10^{22}$ particles/$(m^3 \cdot s)$ is located near $r/D = 0.5$. This is the interface of jet flow and co-flowing stream, and is where thermal conduction and mass diffusion are the greatest. As the jet travels farther downstream, the extent of the flow where nucleation occurs broadens and a second peak (really a plateau) begins appears in the region $1 < r/D < 1.5$. In this region the nucleation rate is roughly $J_s = 10^{15}$.

The performance of the simulation is assessed via comparison with physical data and CNT. Physical data are available for lithium, zinc and magnesium.[3, 1, 2] For brevity we present the validation of zinc nucleation. The CNT result is obtained using

$$J_c = \rho \left(\frac{Y_i}{m_i}\right)^2 \sqrt{\frac{2m_i\sigma}{\pi}} \exp\left(-\frac{16\pi m_i^2}{3\rho^2 \left(\ln S\right)^2} \left(\frac{\sigma}{k_B T}\right)^3\right). \tag{3.12}$$

The data from the simulation is obtained by considering points only where the nucleation rate is equivalent to those in the physical experiments. In the zinc data, this value is $J = 10^{22}$ particles/$(m^3 \cdot s)$. A plot of the saturation ratio vs temperature is shown in Fig. 3.5(b). The data shows that as the temperature increases, the saturation ratio required to yield the same nucleation rate decreases. The saturation ratio decreases from $S = 32$ at $T = 590K$ to $S \approx 10$ at $T = 725K$. Between the simulation, CNT and the physical data, the CNT predictions are the outlier. Over the same temperatures, the values predicted by CNT are at least two orders higher than both the physical data and the simulation. Farther downstream, and away from the jet centerline, as the temperature increases, the performance of CNT improves but a large discrepancy remains. The simulation agrees very well with the physical data. The size-dependency in the surface tension, predicts a lower value of surface energy barrier than CNT for small particles ($d_p \approx 1nm$), such that the formation and growth of stable clusters are readily occurs and thus the saturation ratio required is much lower than CNT. The

discrepancy between the CNT results and the simulation is larger at low temperatures.

3.3.6 Implications for mixing, phase-change and particle formation

This work suggests a dynamic that has not been previously reported. Rapid cooling — typically achieved via turbulent mixing — is widely used to increase nucleation.[62, 63] Traditionally, as the condensible vapor cools, the nucleation rate increases and the size at which particles form/nucleate decreases.[64] I.e. faster cooling means more and smaller particles. It has been a widely used approach for particle synthesis.[51, 40, 65, 66] However, our results suggest that this approach is not as universally valid as one might suppose and, in fact, turbulent mixing may act to suppress particle nucleation in highly-saturated vapors. Scatter-plots of the temperature, $T^\star$, vs zinc mass fraction $Y^\star_{Zn}$ are shown in Fig. 3.6. The results for the size-dependent surface tension are shown in Fig. 3.6(a) and the CNT results are shown in Fig. 3.6(b). For better illustration, the points are colored with the log of the nucleation rate. For orientation, note that when the fluid exits the jet, the mass-fraction is $Y^\star = 1$ and the temperature is $T^\star = 1$, which is the upper right corner of the frame. Dilution and cooling, reflected in Fig. 3.2, decreases both the mass-fraction and the temperature. These do not decrease in equal amounts because the Lewis number is not unity ($Le_{Zn} = 0.74$). (As a result, a 10% change in the temperature corresponds to a 13.5% change in mass-fraction. For lithium, the same change in temperature would result in a 13% change in the Li mass fraction. Similarly for magnesium, a 6.5% change in Mg mass fraction. In fact, in the absence of convective, or other transport — e.g. thermophoresis or soret diffusion transport, radiative heat transfer, etc. — the Lewis number represents the slope by which one traverses the T-Y space from upper right to lower left.) Traveling from upper right to lower left shows that the nucleation rate increases. When the temperature has cooled to $T^\star = 0.5$ and the mass-fraction reaches $Y^\star_{Zn} = 0.4$, the nucleation rate is roughly $J \approx 10^9$. If the flow is cooled to $T^\star = 0.31$ and the mass-fraction diluted to $Y^\star_{Zn} = 0.28$, the nucleation rate increases to $J \approx 10^{23}$. However, Fig. 3.6(a) suggests that further cooling will only serve to decrease the nucleation rate. To be exact, CNT suggests a somewhat similar behavior. However, the mass-fraction must reach to within 6% of its initial value, $Y^\star_{Zn} = 0.06$, before the rate of particle formation begins to decrease.

The results for lithium and magnesium are shown in Fig. 3.7. The nucleation data,

shown in Fig. 3.7(a), are similar to that of zinc in that the rate of particle formation initially increases with decreasing temperature, but then decreases with further cooling. For lithium the highest mass-fraction at which the nucleation rate begins to drop with increased cooling is $Y^{\star}_{Li} = 0.26$. Meaning, subsequent mixing only serves to decrease the nucleation rate. For magnesium, the data shown in Fig. 3.7(b) suggests that nucleation of Mg nanoparticles is "more monotonic" as the flow cools. That is rate of formation does not decrease with increased cooling before the mass-fraction drops to $Y^{\star}_{Mg} = 0.05$.

3.4 Conclusions

We have performed direct numerical simulations of metal nanoparticle nucleation in laminar jets. The flows consist of metal vapor (zinc, lithium, magnesium) diluted in argon issuing into a cooler argon stream. The formation of metal nanoparticles is treated as an irreversible isothermal process and is modeled using a homogeneous nucleation theory with a size-dependent surface tension. The approach is validated via comparison which physical data and classical nucleation theory.

The results show that nucleation occurs at the interface of the two streams, and that this interface increases and the flow travels downstream. As the jet travels downstream, both the temperature and the metal vapor mass-fraction decreases. The former has the effect of increasing the saturation ratio while the latter has the effect of decreasing the saturation ratio. However, the results show that the saturation ratio is much more sensitive to changes in temperature as it is to changes in mass-fraction. This is important in understanding fluid processes leading to gas-phase nucleation. It also has utility when attempting to model particle formation and growth processes and the influence of molecular transport. Recently, researchers utilized a probability density function based approach to model particle formation and growth.[53] This work employed a unity Lewis number, explicitly setting conduction and diffusion equal to each other. This assumption alters or restricts combinations temperature and mass-fraction that result in particle nucleation. For systems where the true Lewis number is less than unity, the result would be an over-prediction in the saturation ratio and number of particles formed, whereas for systems where the true Lewis number is greater than unity, the result would be under-prediction. While turbulence is important in these dynamics,

nucleation is at its core a molecular-scale processes and approaches which depend on a unity Lewis numbers — either for practicality or because of mathematical restrictions — may not be appropriate. Another important result of this work is the notion that increased mixing — mass/chemical mixing as well as energy/temperature mixing — can lead to reduced nucleation rate. For example, while CNT suggests that the nucleation rate for zinc will begin to decrease at a mass fraction of $Y_{Zn} = 0.05$, the more accurate model suggests that this occurs at mass-fractions some six times larger, $Y_{Zn} = 0.28$. Rapid cooling via turbulent mixing is a technique employed in a wide variety of particle production processes. This work suggests that while rapid mixing does generate high saturation ratios, it may do so in regions where the vapor concentration is too low for particles to be formed.

Table 3.1: Nucleation constants and parameters

Species	A (nm^2)	C	D/T	δ_o (nm)	$C_1(\times 10^{-3})$	C_2
Li	-0.389	8.00	8120	0.097	0.140	3300
Mg	-0.406	8.80	7674	0.350	0.254	3128
Zn	-0.45	8.35	6400	0.448	0.167	5430

Table 3.2: Thermal, chemical, and transport properties

Species	Mass fraction	T_o (K)	T_∞ (K)	Re	Pr	Sc	Le
Li	0.02	1615	726	130	0.84	0.65	0.77
Mg	0.02	1400	630	167	1.06	1.62	1.52
Zn	0.02	1000	450	224	0.77	0.57	0.74

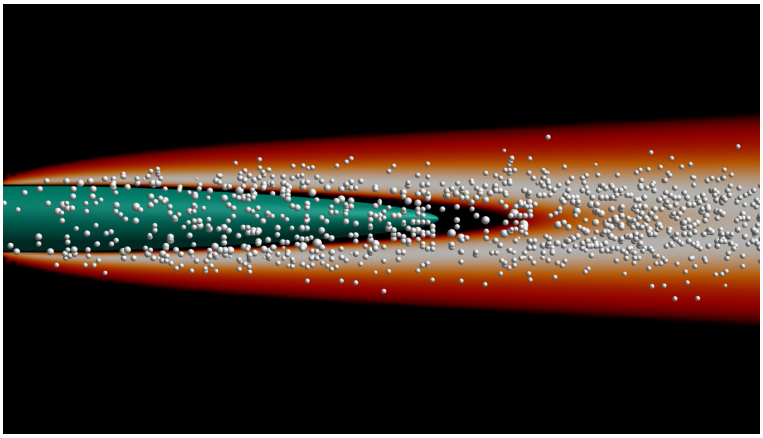

Figure 3.1: Zinc vapor issues in a cool argon stream and particles nucleate. The instantaneous nucleation rate is represented by spheres. The number of spheres is weighted by $\log J$ and the size of the spheres is proportional to the critical diameter.

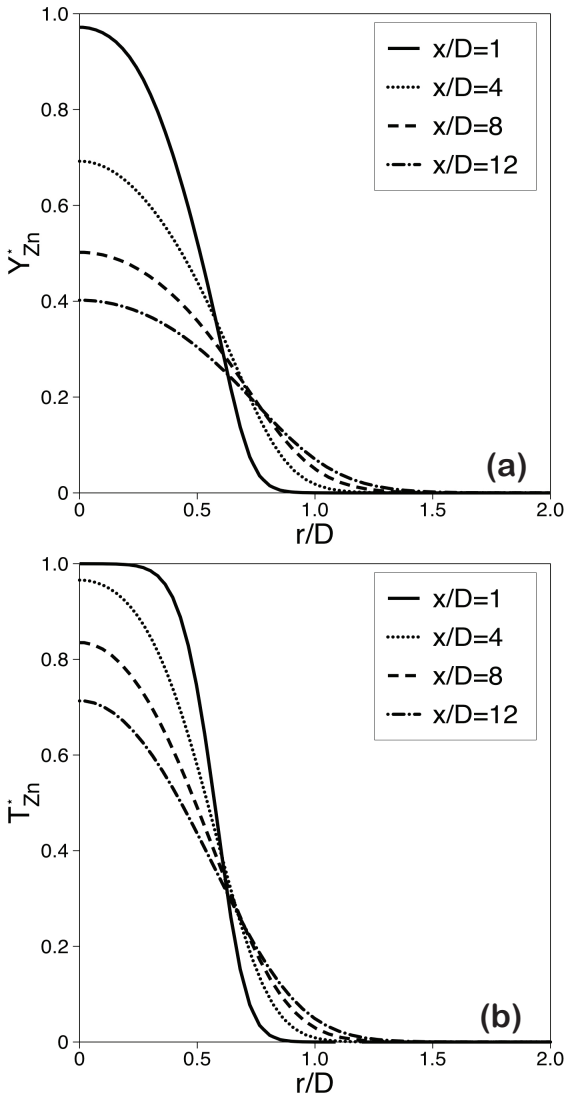

Figure 3.2: Cross-stream profiles of the non-dimensional (a) zinc mass-fraction, $Y^{\star}_{Zn}$, and (b) gas temperature, $T^{\star}$, in the zinc-argon flow.

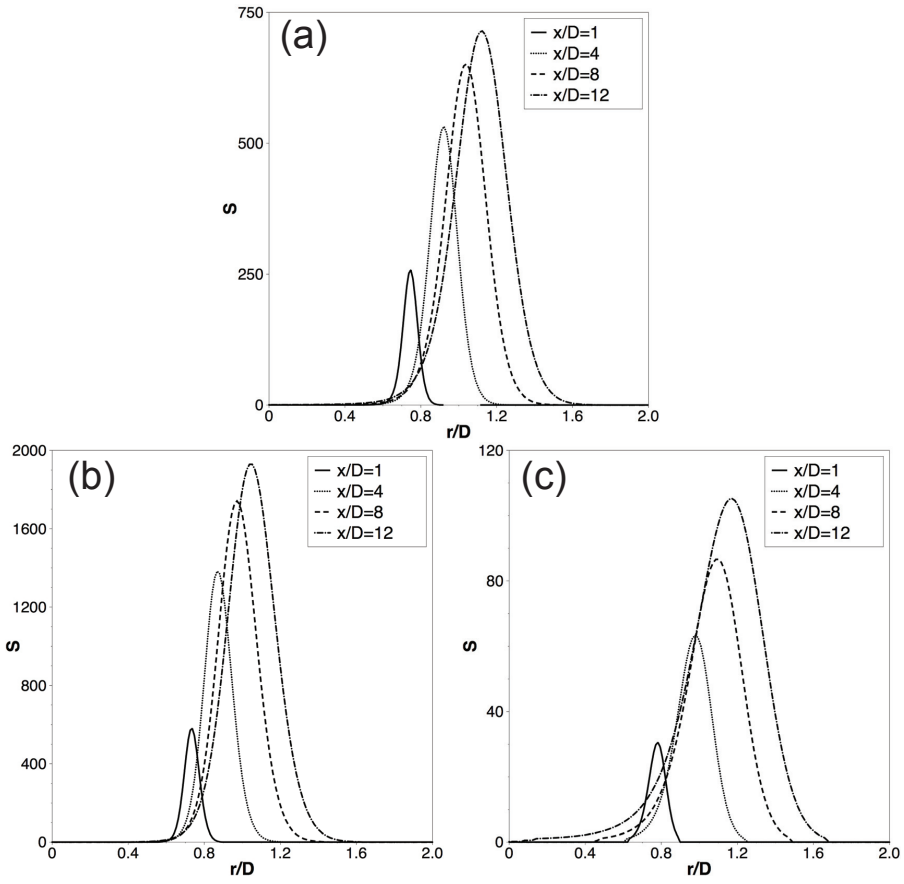

Figure 3.3: Cross-stream profiles of the saturation ratio, S: (a) zinc; (b) lithium; and (c) magnesium.

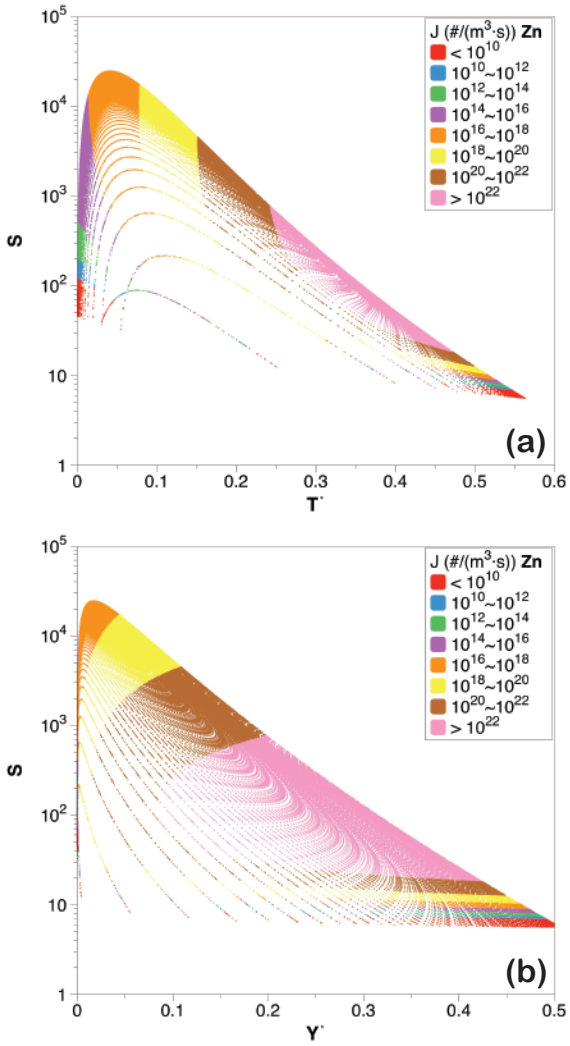

Figure 3.4: (a) Saturation ratio, S vs temperature, $T^{\star}$, and (b) Saturation ratio, S, vs mass-fraction $Y^{\star}$.

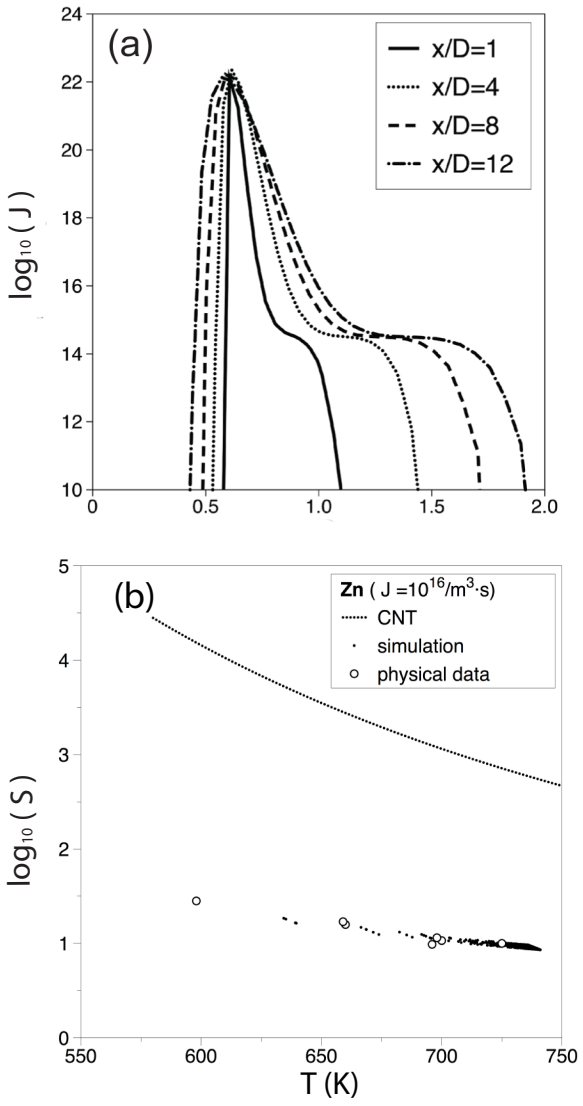

Figure 3.5: (a) Cross-stream profiles of the zinc nanoparticle nucleation rate, J_s ($\#/(m^3 \cdot s)$); (b) Validation of the laminar flow simulations via prediction of S *vs.* T with physical data, and CNT for zinc. Each physical data point represents an experiment at a particular a saturation ratio required to obtain $J = 10^{16}$.

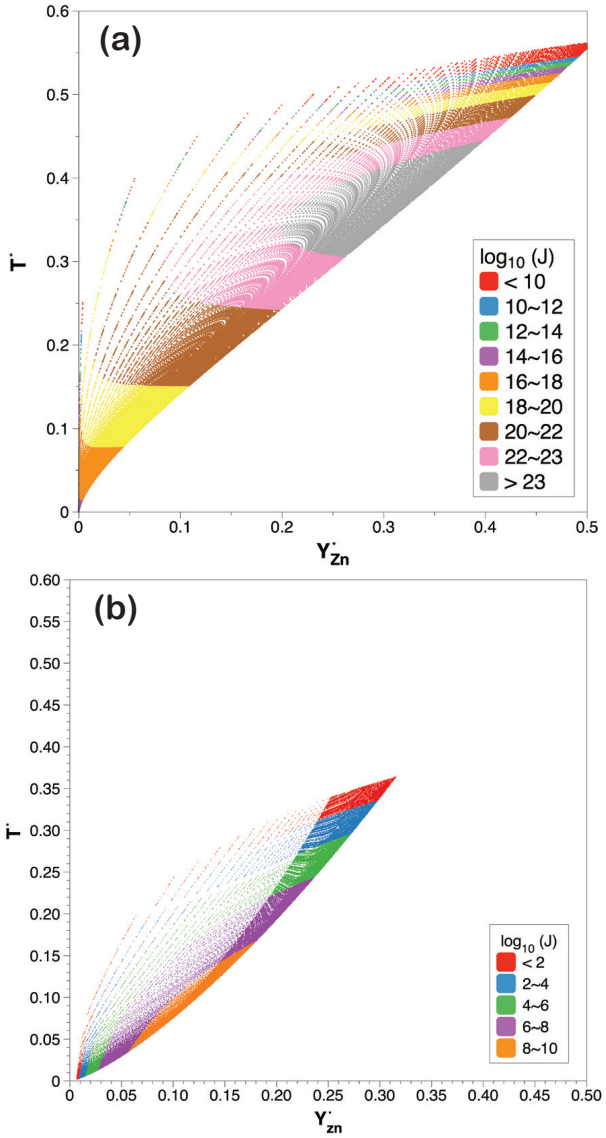

Figure 3.6: Temperature vs zinc mass-fraction as a function of nucleation rate: (a) size-dependent surface tension; (b) classical nucleation theory.

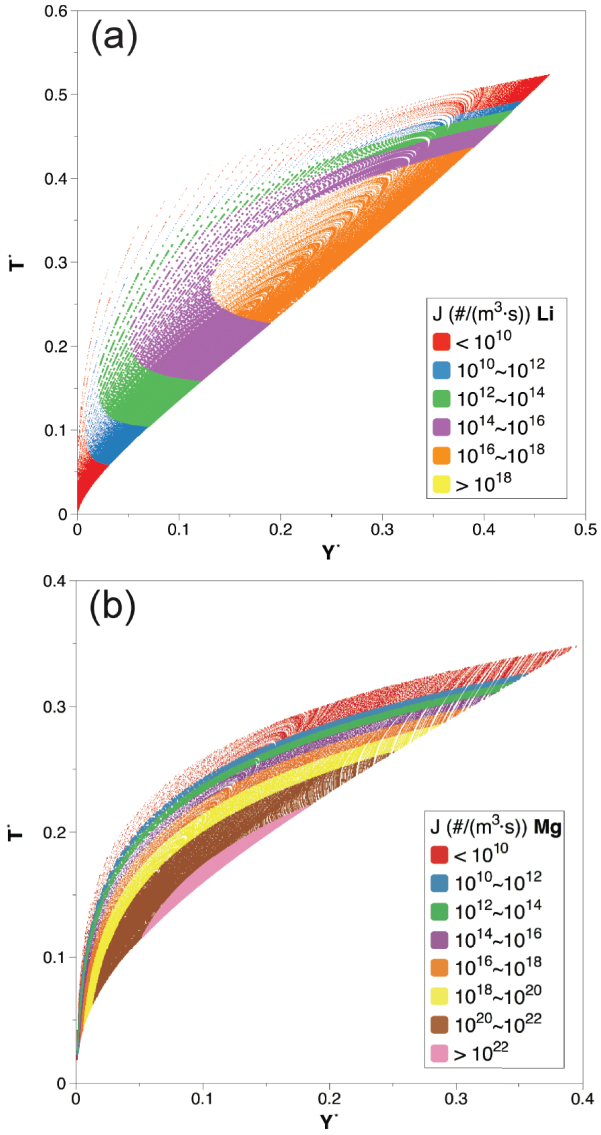

Figure 3.7: Temperature vs mass-fraction as a function of nucleation rate: (a) lithium; (b) magnesium.

Chapter 4

Metal particle nucleation in turbulent flows

Mixing effects of flow turbulence on metal nanoparticle formation via homogeneous nucleation are analyzed using direct numerical simulations. Simulations are performed for zinc nanoparticle homogeneous nucleation in three-dimensional turbulent round jet flows. The flows consist of a high-temperature jet stream with zinc vapor diluted in argon issuing into a low-temperature particle-free argon co-flow. The fluid, thermal, and chemical transports are obtained by solving the Navier-Stokes, enthalpy, and mass transport equations. The zinc nanoparticle formation is simulated via a size-dependent surface tension homogeneous nucleation model. The results show that particle nucleation initially occurs in the shear layers between the jet flow and co-flow, and then into the vortex cores when the flow transits into turbulence. Pre-transition, the nucleation is caused majorly due to molecular mixing processes. During transition, the nucleation happens in the region where large scale convective structures are the major source of mixing. Post-transition, the large structures of flow movement break down into turbulence. During turbulent mixing, zinc particles are produces uniformly across the jet, with the small scale dilution as well as cooling by the flow turbulence. More significantly, the results indicate with turbulence, particles are produced at a wider range of sizes. With size-dependent surface tension, faster cooling and transition into turbulence will actually decrease particle nucleation.

4.1 Introduction

Simulating metal homogeneous nucleation in turbulent flows is both a challenge and a need for many scientific and industrial applications. Turbulent flows have features and dynamics that vary on both length scale and time scales that are very different than that of laminar flows. Meanwhile, it has very significant applications in nanoparticle manufacturings since pursuing faster cooling by stirring and faster mixing is the mainstream opinion of increasing nanoparticle production rate nowadays [67, 68].

Homogeneous nucleation is highly sensitive on local temperature and vapor concentration [67, 24, 69, 70]. As a result, fluctuations in these quantities can result in orders of magnitude changes in the local nucleation rate. However, modeling of the small scale, unresolved fluctuations on homogeneous nucleation is challenging, and the little insight into the significance of these fluctuations is available [68]. Direct numerical simulation could resolve all time and length scales explicitly. No assumptions about flow development nor the mixing processes need to be done in a prior manner [21]. The mechanism of fluid turbulent is still not well understood, and the nanoparticle nucleation in turbulent flows could be a very complex process involving small time and spatial scales [71]. When experimental methods cannot fully capture/resolve the small-scale dynamics (space and time), accurate numerical methods are superior. In many scenarios they're also more economical [22].

In this work we perform simulations of zinc nanoparticle nucleation in turbulent round jets. The flows consist of a high-speed jet of zinc metal vapor issuing into a cooler stream. As the two streams mix, the metal vapor becomes super-saturated and nanoparticles form via homogeneous nucleation. We utilize direct numerical simulation approach to assess the effects of the small-scale thermo-chemical interactions on nanoparticle nucleation. This serves as a benchmark simulation. More precisely, the nucleation rate and critical diameter are based on the small scale-resolved temperature, density, and vapor concentrations. This approach allows us identify the effects of the small scales flow structures on nanoparticle nucleation.

4.2 Formulation

4.2.1 Fluid and scalar transport

The flows are governed by the compressible Navier-Stokes equations. The primary variables are the fluid density $\rho(\vec{x})$, velocity $u_i(\vec{x})$, pressure $p(\vec{x})$, and the enthalpy $h(\vec{x})$, which are obtained by

$$\frac{\partial \rho}{\partial t} + \frac{\partial \rho u_i}{\partial x_i} = 0, \tag{4.1}$$

$$\frac{\partial \rho u_i}{\partial t} + \frac{\partial \rho u_i u_j}{\partial x_j} = -\frac{\partial p}{\partial x_i} + \frac{\partial \tau_{ij}}{\partial x_j}, \tag{4.2}$$

$$\frac{\partial \rho h}{\partial t} + \frac{\partial \rho u_j h}{\partial x_j} = \frac{\partial}{\partial x_j}\left(\frac{k}{C_p}\frac{\partial h}{\partial x_j}\right), \tag{4.3}$$

where τ_{ij} represents viscous stress tensor, k is the coefficient of thermal conductivity, C_p is specific heat at constant pressure, and $\dot{Q}$ is the enthalpy increase per unit time due to nucleation. The enthalpy h is related to temperature T via $dh = C_p dT$. The equations are closed using the ideal gas relation, $p = \rho RT$, where R is the gas constant.

The transport of metal vapor mass fraction Y_i is governed by

$$\frac{\partial \rho Y_i}{\partial t} + \frac{\partial \rho u_j Y_i}{\partial x_j} = \frac{\partial}{\partial x_j}\left(\rho D_i \frac{\partial Y_i}{\partial x_j}\right) - \dot{\omega}_i, \tag{4.4}$$

where D_i is the diffusion coefficient and $\dot{\omega}_i$ is the 'sink' term due to nucleation. The enthalpy increase per unit time due to the nucleation process is given by $\dot{Q} = \dot{\omega}_i h_o$, where h_o is the enthalpy of formation of metal particle per unit mass.

4.2.2 Nucleation modeling

The particle nucleation rate J is based on CNT with the use of several correction factors. These corrections are omitted here as they are not the subject of our investigation and are found elsewhere [44, 54, 33, 35]. The rate of particle formation is given by

$$J_s = \frac{\rho Y_i}{2 m_i \pi R_S}\sqrt{\frac{3\ln S}{\rho\kappa}}\sqrt{\frac{R_S}{R_e}}\exp\left(-\frac{16\pi m_i^2}{3\rho^2(\ln S)^2}\left(\frac{\sigma}{k_B T}\right)^3\right), \tag{4.5}$$

where m_i is mass of a molecule, $\sigma(T, d_p)$ is the surface tension, d_p is the critical nuclei diameter, R_e is the equimolar radius, R_s is given by $R_s = d_p/2$, κ is the isothermal compressibility, k_B represents the Boltzmann constant. S is the saturation ratio. The

size of the critical nuclei, or the size at which particles form, is given by the Kelvin relation

$$d_p = \frac{4\sigma m_i}{k_B T \rho_i \ln(S)}. \tag{4.6}$$

This rate expression been shown to be accurate in predicting the nucleation of a variety of metal nanoparticles [3, 35].

4.3 Results

4.3.1 Flow configuration

The turbulent flow simulations set-ups are similar to the laminar flows described above except the Reynolds number, which is based on the jet diameter, is increased significantly. Here the Reynolds number is $Re_D = 3600$. The velocity ratio is $U_o/U_\infty = 3$ and the temperatures are $T_o = 1000K$ and $T_\infty = 450K$. The flow configuration is shown in Fig. 4.1, along with an iso-surface of vorticity. (In the laminar flow, $Re_D = 335$, the surface would be a simple cone.)

The governing equations for the flow, thermal and chemical transport are solved via a fourth order accurate hybrid MacCormack, predictor-corrector scheme [58, 59]. Numerical Simulations are performed on a domain of $14D \times 8D \times 8D$ in x, y and z directions respectively. The resolution for all simulations is $640 \times 480 \times 480$. The results exhibited grid independence at this resolution. Each simulation was performed using 2048 CPUs and required roughly 60,000 CPU-hours.

4.3.2 Physical assumptions and numerical specifications

The simulations are performed on a domain size of $14D \times 8D \times 8D$ in the x, y, and z directions, respectively. A clustered, structured grid is employed with a resolution of $640 \times 480 \times 480$. Grid clustering is used to resolve the shear layers as the flow evolves in the stream-wise direction. Random perturbations are added at the inlet of the jet nozzle to accelerate the development of large-scale flow structures. For the nodal approximation of the GDE, a total of $NB = 13$ bins are used to discretize the particle distribution.

4.3.3 Effects of turbulence on scalar transport

Contours of the instantaneous temperature for both the laminar and turbulent flows at the central planes of the jets are captured in Fig. 4.2. In laminar jet flow, the temperature along the center remains relatively high, and changes slowly and gradually, at the outlet the temperature of center in laminar jet is almost 20% higher than the turbulent one. In turbulent jet flow, vortex structures form, merge and interact to produce smaller-scale features. The large-scale structures act to bring the cooler co-flow into the jet. This increases the contacting surface area of jet flow with the cooler co-flow. Small scale mixing via molecular diffusion dominates in laminar flows. In turbulent flows, large scale convective mixing dominates. This increased mixing and heat transfer provides more rapid cooling which is mechanism often used to increase particle production. Such significant and unique properties of the turbulent flow are the direct stimulus for further investigation in the effect of turbulence on nanoparticle nucleation. This interdisciplinary field is relatively new and provide a promising opportunity for new discoveries.

Cross-stream contours of the instantaneous vorticity magnitude in turbulent round jet flows are shown in Fig. 4.3. The figures represent the evolution of the flow vorticity. Initially vorticity contour is cylindrical or "ring" shaped. In the early stage of flow development, the vortex contours coincide with the contacting layer of the flows. As the flow travels downstream, perturbations and excitations begin to grow due to the non-linear nature of the governing equations and characterized by the large Reynolds number. The perturbations added at the inlet plane are similar to those observed in so-called "crown jets" [72]. The physical effects of the large structures act to bring the cooler co-flow into the cores of the eddies, where the density of the condensing vapor is still high, so that the condensing vapor get super saturated. At the same time, the eddy structures bring more contact surface between the jet flow and co-flow. These are interesting in that they feature side-jets. Turbulent flows are ones in which existing vorticity generates more vorticity, and rapidly increases the rate of mixing. This vorticity acts to greatly increase fluid mixing.

4.3.4 Effects of turbulence on nucleation

Instantaneous contours of the nucleation rate are shown in Fig. 4.4. The cross-stream contours are taken at 6 different x/D locations and show that nucleation primarily occurs at the contacting shear layers. This is due to the fact that at the interfaces, the jet is cooled down and the zinc vapor becomes super-saturated. As the flow travels further downstream, nucleation increases spatially in the similar manner as vortex structures evolve. So that it is not surprising the types of flow could greatly affect the total nucleation rate. Before $x/D = 5$, nucleation mainly happens at the shear layer, where molecular diffusion processes are the major sources of mixing. After $x/D = 5$, nucleation happens within the small "side-jets" where the small structures bring in more cooler flow into the cores of eddies. The flow structure is still symmetric until $x/D = 12$, the small structures not only result in better mixing, they also bring various combinations of local temperature and condensing vapor mass fractions.

Figure 4.5 shows the significance of vorticity and nucleation evolution based on the turbulence and different scales of mixing in turbulent round jet simulation. (This is for a turbulent round jet without the crown-jet perturbations.) Near the jet inlet, small scale molecular mixing dominates in the cylindrical shaped contacting shear layer. As the jet flow travels downstream, the large scale movements as folding and ring-shaped vortex structures begin to form and convective mixing begins to be more important, it brings the cooler co-flow into the center of the jet flow much quicker. The stability of the round jet breaks down eventually, vortex structures emerge and separate quickly to generate more vorticity, after which the flow becomes turbulent, small structures and fluctuations involve more cooler flow into the center of the jet and spread the condensing species into deeper the co-flow.

Figure 4.6 shows the critical cluster size as a function of temperature and vapor mass fraction in zinc nucleation. Each colored point in this plot represents a combination of these quantities under which the zinc nanoparticles can be formed via nucleation. The results show: (1) at the same temperature, when vapor concentration increases, the size of critical clusters decreases rapidly for very low concentration region, and keeps decreasing slowly for a long range; For example, at $T = 600K$ and the xritical particle diameter decreases rapidly when $Y < 1 \times 10^{-3}$, from $d_p = 1,2nm$ to about $d_p = 0.8nm$. However between $Y = 1 \times 10^{-3}$ and $Y = 2 \times 10^{-3}$ at the same temperature, the

critical particle diameter remains about $d_p = 0.7$ to $0.8nm$. Between $Y = 2 \times 10^{-3}$ and $Y = 5 \times 10^{-3}$ at the same temperature, the critical particle diameter remains about $d_p = 0.7nm$ (2) at the same vapor concentration, when temperature increases, the size of critical clusters increases rapidly; For example, at $Y = 1 \times 10^{-3}$, and temperature increases from $T = 500K$ to $T = 670K$, the critical sizes of nuclei drop from $d_p = 0.6nm$ to $d_p = 1.2nm$. (3) larger particle ribbon is much narrower, meaning it is harder to produce uniformly distributed large nanoparticles in the system. The results also show that certain ranges of temperatures and vapor concentrations are favored in zinc nanoparticle nucleation in turbulent practical flow, and the size of the critical cluster is more sensitively to the changes of temperature.

The relation of zinc nucleation rate on saturation ratio and temperature is shown in Fig. 4.7. It gives the correlation of nucleation rate as related to the saturation ratio and temperature. The CNT has overestimated the minimum saturation ratio required for zinc nanoparticles to be forming in practical flows. Our results could assist the design of aerosol reactor for zinc nanoparticle synthesis. With carefully controlling the effect of turbulence and other physical parameters, we can get suitable and uniform sized nanoparticles at a higher optimized nucleation rate. As compared to the laminar simulation results in the Appendix, the turbulent effects on nucleation mainly results in more combinations of temperature and saturation ratio. At the same temperature, the nucleation rate does not necessarily increase with increasing saturation ratio. For example, at $T = 600K$ and when the saturation ratio is increasing, the nucleation rate increases as the saturation ratio is between $S = 10^{1.5}$ and $S = 10^{2.2}$. After that the nucleation rate will decrease with increasing saturation ratio. From the perspective of particles' sizes, at the same temperature, the critical particle sizes decrease with increasing saturation ratio too, as shown in the figure. The results indicate that faster mixing, which is caused by more small structure diluting/cooling of the condensing vapor and induces higher saturation ratio, may not always increase the nucleation rate with size-dependent surface tension.

4.4 Conclusion

We have performed direct numerical simulations of metal nanoparticle nucleation in turbulent round jets. The flows consist of zinc vapor diluted in argon issuing into a cooler argon stream. The formation of zinc nanoparticles is treated as an irreversible isothermal process and is modeled using a homogeneous nucleation theory with a size-dependent surface tension. The approach is validated via comparison which physical data and classical nucleation theory.

The results show that pre-transition, nucleation occurs at the interface of the two streams, and that this interface increases and the flow travels downstream. As the jet travels downstream, both the temperature and the metal vapor mass-fraction decreases. The former has the effect of increasing the saturation ratio while the latter has the effect of decreasing the saturation ratio. Flow turbulence bring in more combinations of temperature and mass fraction, and nucleation happens across the stream spatially wider with mixing effects caused by small structures. The results also indicate that molecular mixing is the major driven force for nucleation before the flow transit into turbulence. Post-transition, the large scale convection and small structure dilution/cooling are the driven forces for nucleation. During turbulent mixing, zinc particles are produces uniformly across the jet. More significantly, the results indicate with turbulence, particles are produced at a wider range of sizes. With size-dependent surface tension, faster cooling and transition into turbulence will actually decrease particle nucleation.

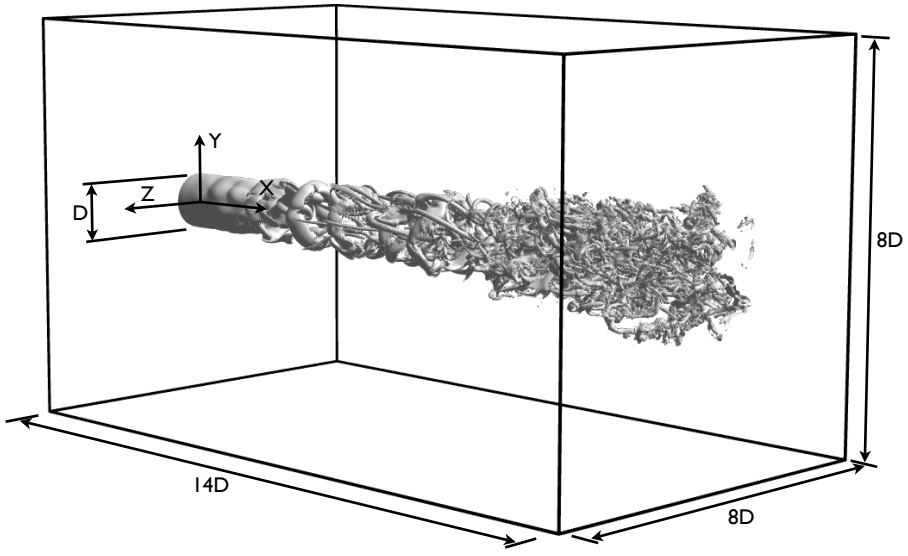

Figure 4.1: Flow configuration for the round jet.

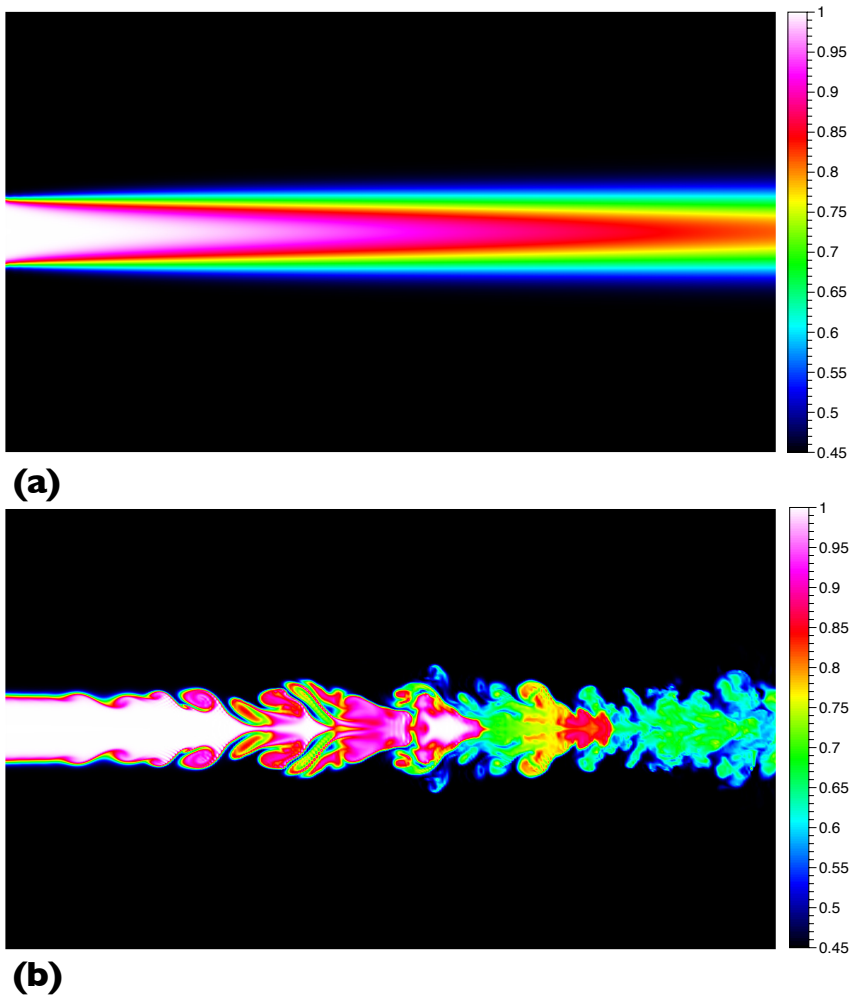

Figure 4.2: Instantaneous countours of the normalized temperature, T/T_{max} along the central plane of the jet z/D=0: (a) laminar flow; (b) turbulent flow.

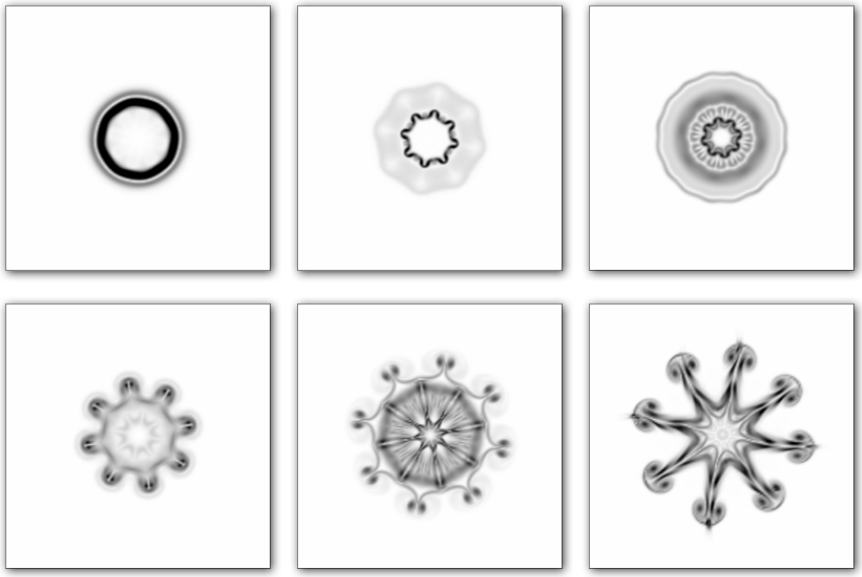

Figure 4.3: Instantaneous vorticity magnitude contours, Ω. From upper-left: (1) x/D=0.5, (2) x/D=3.5, (3) x/D=5, (4) x/D=7.2, (5) x/D=9.5, (6) x/D=11.5.

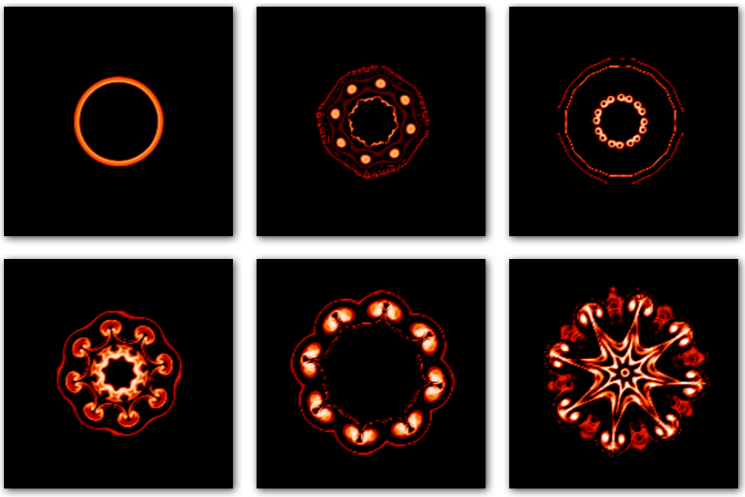

Figure 4.4: Instantaneous nucleation rate magnitude contours, J. From upper-left: (1) x/D=0.5, (2) x/D=3.5, (3) x/D=5, (4) x/D=7.2, (5) x/D=9.5, (6) x/D=11.5.

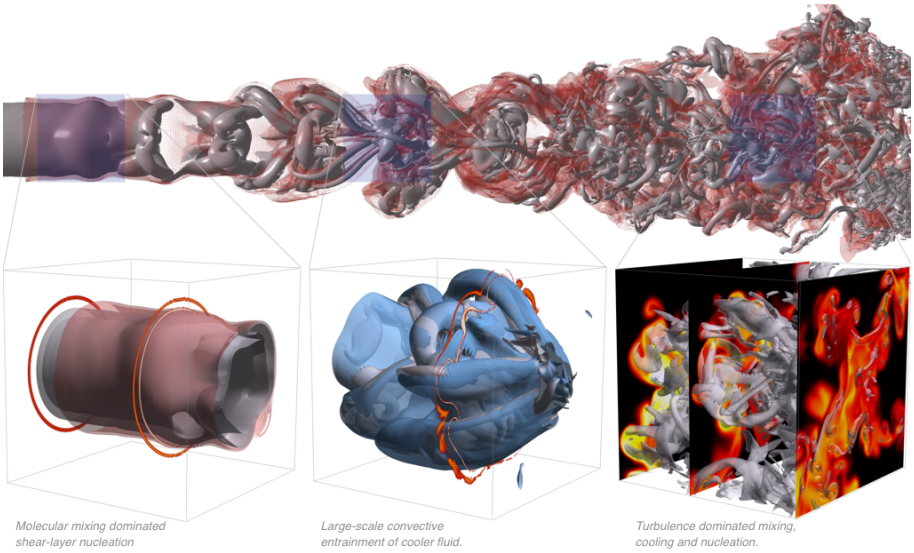

Figure 4.5: Nucleation of zinc nanoparticles in a turbulent round jet. The gray isosurfaces reveal locations in the flow where the vorticity is 1/4 the maximum value. In the top image, the red surface indicates where the nucleation rate is 10^{18} particles per m^3 per second. The area of the red surface increases with mixing and along the downstream direction.

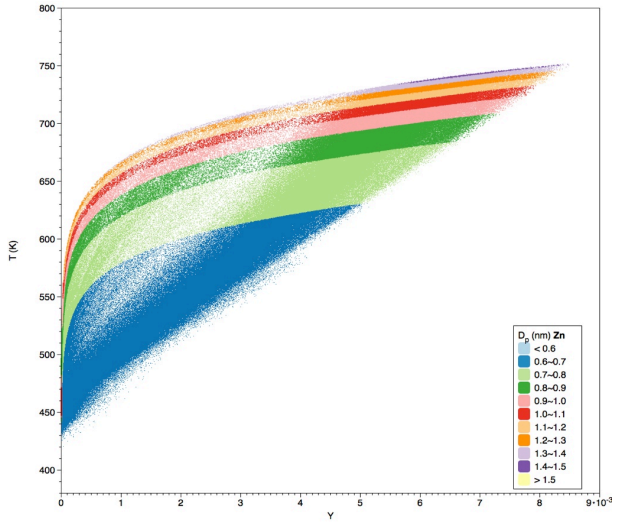

Figure 4.6: Nucleation of zinc nanoparticles in a round turbulent jet.

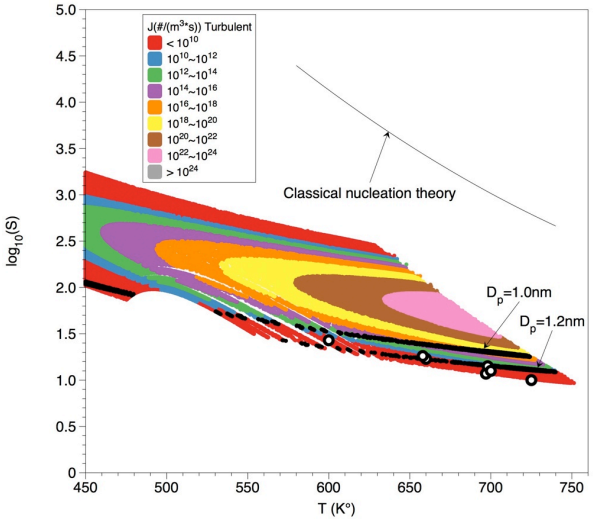

Figure 4.7: Nucleation of zinc nanoparticles in a round jet. The solid line represent the classical nucleation theory (CNT). The circles represent the physical data of Onischuk *et al.* [3]

Chapter 5

Effects of heat release on the homogeneous dibutyl-phthalate nucleation in laminar jets

The effects of nucleation heat release during the nucleation of dibutyl-phthalate (DBP nanoparticles is studied via direct numerical simulation. We simulate the formation of DBP nanoparticles via homogeneous nucleation in laminar jets. The flows consist of DBP vapor diluted in nitrogen gas issuing into a cooler, slower moving nitrogen stream. Simulations are performed at different nucleation Damköhler numbers (representing the ratio of the inertial time scale to the nucleation time scale) and also with and without heat-release due to phase change. By doing this we are able to establish the effects of heat-release on the particle nucleation process. The results show that as the nucleation Damköhler number is increased, the temperature of the flow increases. However the resulting temperature increase does not significantly affect the jet growth-rate or velocity field. The resulting temperature increase does affect the saturation ratio, nucleation rate, and critical diameter. As the nucleation Damköhler number is increased, the difference in the saturation ratios, with and without heat-release, increases significantly. The result is that the neglect of heat-release leads to an over-prediction in nucleation rate (by as much as 6 orders of magnitude) and an under-prediction in the diameter of the nucleated nanoparticles (by as much as 50 percent).

5.1 Introduction

Gas-to-particle phase change by nucleation plays an essential role in many scientific and industrial processes [16, 73, 71]. Formation of particles via homogeneous nucleation is very sensitive to the local temperature and also concentration of condensing vapor [74, 75]. In many processes, nucleations is accompanied by heat release during phase-change. The energy release – the amount of which is proportional to the particle formation rate – can affect fluid flow and fluid properties, which in turn affects particle formation. The result is a tightly coupled non-linear interaction. As a result knowledge of the interaction between the fluid, thermal and scalar fields is critical to the accurate prediction of particle nucleation [42, 23].

Previous investigations have demonstrated that under low vapor concentration, and for some materials, the amount of heat release is negligible and the simulation results agree well with physical data [76, 22]. However, for nucleation of materials which are accompanied by significant amount of energy release, such as DiButyl phthalate (DBP), heat release may play an important role [77, 78]. For example, researchers have shown, via molecular dynamics, that the time required to establish equilibrium for gas-particle interactions is smaller with heat release [79]. Additionally, experiments of laminar planar reacting mixing layer show that the growth rate of the shear layer decreases slightly with increasing heat release [80]. Nonetheless, it is not uncommon to neglect the effect of heat-release and therefore the coupling between the fluid, thermal, chemical and particle fields [53].

In this work, we utilize direct numerical simulation of DBP nucleation in three-dimensional laminar planner jet flows to investigate the nucleation heat release effects on the interaction of fluid dynamics and nucleation. Simulations are conducted under different nucleation Damköhler numbers both with and without no heat release, which allows insight into the heat release effects on fluid-nucleation interaction at different particle formation rates. We utilize data from the simulations to examine the jet growth and particles mass fluxes at downstream locations. Clarification need to be made that we are analyzing nucleation heat release only as a minimum level of heat release, heat release during other particle formation mechanisms are not considered here.

5.2 Formulation

5.2.1 Fluid and scalar transport

The flow fields are governed by the compressible Navier-Stokes equations. The primary variables are the fluid density ρ, velocity $u_i(\vec{x}$, pressure p, and the enthalpy $h(\vec{x}$, which are obtained by

$$\frac{\partial \rho}{\partial t} + \frac{\partial \rho u_i}{\partial x_i} = 0, \tag{5.1}$$

$$\frac{\partial \rho u_i}{\partial t} + \frac{\partial \rho u_i u_j}{\partial x_j} = -\frac{\partial p}{\partial x_i} + \frac{\partial \tau_{ij}}{\partial x_j}, \tag{5.2}$$

$$\frac{\partial \rho h}{\partial t} + \frac{\partial \rho u_j h}{\partial x_j} = \frac{\partial}{\partial x_j}\left(\frac{k}{C_p}\frac{\partial h}{\partial x_j}\right) + \dot{Q}, \tag{5.3}$$

where τ_{ij} is the viscous stress tensor, C_p is the specific heat at constant pressure, and k is the coefficient of thermal conductivity. $\dot{Q}$ is the enthalpy increase per unit time due to nucleation. The enthalpy h is related to temperature T via $dh = C_p dT$. The equations are closed using the ideal gas relation, $p = \rho RT$, and R is the gas constant.

The transport of DBP vapor mass fraction Y_i is governed by

$$\frac{\partial \rho Y_i}{\partial t} + \frac{\partial \rho u_j Y_i}{\partial x_j} = \frac{\partial}{\partial x_j}\left(\rho D_i \frac{\partial Y_i}{\partial x_j}\right) - \dot{\omega}_i, \tag{5.4}$$

where D_i is the diffusion coefficient and $\dot{\omega}_i$ is the 'sink' term due to nucleation. The enthalpy increase per unit time due to the nucleation process is given by $\dot{Q} = \dot{\omega}_i h_o$, where h_o is the enthalpy of formation of DBP particle per unit mass.

5.2.2 Nucleation modeling

We utilize the nucleation rate predicted by a self-consistent classical nucleation theory [44]. The nucleation rate expression J is given by

$$J = \frac{(\rho Y_i)^2}{\rho_i m_i S}\sqrt{\frac{2\sigma}{\pi m_i}}\exp\left(-\frac{\pi\sigma {d_p}^2}{3k_B T} + \frac{\sqrt[3]{36\pi v_i^2}\sigma}{k_B T}\right). \tag{5.5}$$

where S is the saturation ratio, k_B is the Boltzmann constant, m_i is mass of a molecule, and ρ_i is the density of condensed DBP. The volume per molecule v_i is given by m_i/ρ_i, σ is the surface tension. The critical size of DBP nuclei d_p is given by the Kelvin relation,

$$d_p = \frac{4\sigma m_i}{k_B T \rho_i \ln(S)}. \tag{5.6}$$

The 'sink' term of DBP vapor mass transport equation (Eq. 5.4 is then given by

$$\dot{\omega}_i = \frac{\pi}{6}\rho_i {d_p}^3 J. \tag{5.7}$$

To parameterize the nucleation process, non-dimensional variables (marked with $\star$) can be defined using the following reference values (marked with subscript o) :

$$x_i^\star = \frac{x_i}{L_o},\ \ u_i^\star = \frac{u_i}{U_o},\ \ \rho^\star = \frac{\rho}{\rho_o},\ \ Y^\star = \frac{Y}{Y_o},\ \ \rho_i^\star = \frac{\rho_i}{\rho_{io}},\ \ \sigma^\star = \frac{\sigma}{\sigma_o}, \tag{5.8}$$

where L_o is the reference length scale, U_o is the reference velocity, ρ_o and ρ_{io} are the reference density for the fluid and DBP particles, respectively. Y_o is the reference value of DBP vapor mass fraction, and σ_o is the reference value of DBP surface tension. The non-dimensional nucleation rate $J^\star$ is given by $J^\star = J \cdot L_o/(\rho_o U_o)$. The non-dimensional nucleation sink term $\dot{\omega}_i^\star$ in the transport equation of DBP vapor is given by

$$\dot{\omega}_i^\star = \frac{L_o}{U_o \rho_o}\frac{\pi}{6}\rho_i d_p^3 J, \tag{5.9}$$

where the number nucleation rate J and particle critical diameter d_p are given by Eq. 5.5 and Eq. 5.6 respectively, which yields

$$\dot{\omega}_i^\star = Da \cdot \left(\frac{\sigma^\star}{\rho_i^\star T^\star \ln(S)}\right)^3 \frac{\left(\rho^\star Y^\star\right)^2 \sqrt{\sigma^\star}}{S} \exp\left(-\frac{\pi\sigma {d_p}^2}{3k_B T} + \frac{\sqrt[3]{36\pi v_i^2}\sigma}{k_B T}\right). \tag{5.10}$$

The nucleation Damköhler number, Da, which includes all the reference parameters and reflects dependence of specific flow-nucleation system, is then given by

$$Da = \frac{L_o}{6U_o\rho_o}\left(\frac{(\rho_o Y_o)^2}{m_i^{3/2}}\sqrt{2\pi\sigma_o}\right)\left(\frac{\sigma_o m_i}{\rho_{io} k_B T_o}\right)^3, \tag{5.11}$$

the value of Da represents the magnitude of nucleation rate.

5.3 Results

5.3.1 Flow configuration

The flow fields consist of a three dimensional planar jet with nozzle width D. Jet flow with velocity U_o issues into a co-flowing particle-free nitrogen stream with velocity U_∞.

A schematic of the flow configuration is shown in Fig. 5.1. The flows are laminar and the velocity ratio is $U_o/U_\infty = 3.0$. The temperature of the heated jet flow is T_o and the temperature of the cooler nitrogen stream is T_∞, where $T_o = 400K$ and $T_\infty = 300K$. The mass fraction of DBP vapor at the inlet of the jet is Y_o.

5.3.2 Physical parameters and numerical specifications

The Reynolds number, $Re = U_o D/\nu = 200$, is the ratio of inertial to diffusive forces, where ν is the kinematic viscosity; the Lewis number, $Le = Sc/Pr = 4$, represents the ratio of thermal diffusivity to mass diffusivity. The values of all parameters are listed in Table 5.1. The nucleation Damköhler number, Da, is used to describe different nucleation rates in various DBP nucleation flows. Nucleation with or without heat release is simulated via $\dot{Q} = \dot{\omega}_i h_o$ or $\dot{Q} = 0$. All physical properties of the condensing material and the gas mixtures are calculated based on the local temperature T, and also mass fraction of each chemical species Y_i. The properties of DBP are taken from previous work [81, 82, 27]. The DBP condensed phase density is given by $\rho_i = 1063 - 0.826\,(T - 273.16)\,kg/m^3$, its surface tension is $\sigma = 0.0353 - 0.0000863\,(T - 273.16)\,N/m$, and the saturation mole fraction is given by $x_{sat} = \exp(21.497 - 11497/T)$. A typical volume fraction of particles within the flow is 10^{-6} at maximum, so that the momentum transport between particles and fluids are negligible.

The governing equations for the flow, thermal and chemical transport are solved via a fourth order accurate hybrid MacCormack-based, predictor-corrector scheme [58, 59]. Simulations are performed on a domain of $12D \times 8D \times 6D$ in x, y and z directions respectively. The resolution for all simulations is $320 \times 240 \times 120$. The grid is clustered about the shear layers and each simulation performed requires roughly 300 CPU-hours.

5.3.3 Scalar transport

As energy is released during phase change, the local temperature increases. Cross-stream profiles of normalized temperature, $T^\star = (T - T_\infty)\,/\,(T_0 - T_\infty)$, taken at the $z = 0$ plane are shown in Fig. 5.2. The figure shows that the jet mixes with the background fluid and is cooled as it travels downstream, i.e. the temperature in the jet

($|y|/D < 0.5$) decreases with x/D while the temperature in the co-flow ($|y|/D < 0.5$) increases with x/D. As expected, the temperature profiles for the simulations which are without heat-release are identical. However, the temperatures in the flows with heat-release do differ. The results for case 1 ($Da = 206.8 \times 10^2$), shown in Fig. 5.2(a), suggests that the effects of heat-release on the fluid temperature are quite small if not insignificant. In case 2 ($Da = 206.8 \times 10^6$), shown in Fig. 5.2(b), differences appear. For example, at $x/D = 8$ along the jet centerline ($y/D = 0$), the temperature is 7.5% greater with heat-release than without. Further away from the centerline, near $y/D = 0.5$ the increase is even more pronounced with a 30% greater temperature with heat release. In case 3 ($Da = 206.8 \times 10^9$), Fig. 5.2(c) the effects of heat-release are even more significant. By $x/D = 8$, the centerline temperature with heat-release is 14%, and 36% at the jet edge.

The saturation ratio, S, acts as a bridge between the fluid dynamics and particle nucleation. Contours of saturation ratio S are shown in Fig. 5.3. The saturation ratios are higher than unity (I.e. the condensing vapor is supersaturated) within shear layers formed between the jet flow and co-flow, and generally increase in stream-wise direction and spread spatially in both cross-stream directions. The typical values of saturation ratio in Fig. 5.3(a) are similar to the values in Fig. 5.3(c). For example, the maximum values of saturation ratio are $S = 200$ and 220, respectively. The results indicate that at low nucleation rates and low Damköhler number, the heat release effects on saturation ratio is not significant. At high Damköhler number ($Da = 206.8 \times 10^9$), as shown in Case 3, the typical values of saturation ratio are $S = 50$ and $S = 150$ with and without heat release. Not only does this show that increasing the Damköhler number generally decreases the saturation ratio, it also shows that the heat release effects are only significant at higher nucleation Damköhler numbers, e.g. $Da > 206.8 \times 10^2$. For lower nucleation rates, the heat release effects are negligible. For higher nucleation rates, the heat release effects become more essential with increasing Da.

5.3.4 Nucleation rate and critical size

The contribution of heat release on the fluid dynamics also affects the nucleation processes. Figure 5.4 shows the cross-stream profiles of critical particle diameter as the flow travels downstream. For clarification the profiles are only shown for the region where

the nucleation rate is greater than unity. At low Damköhler number, as shown in Fig. 5.4(a), the differences between heat-release case and no-heat-release cases are negligible. The critical particle diameters are the smallest in shear layers formed between jet flow and co-flow ($y/D \approx 0.5$) and spread into the co-flow as the jet travels downstream. The critical particle diameter increases as the flows further mix. Fig. 5.4(b) shows at higher Damköhler number, the particle diameter is higher with heat release, which is more important within the jet region ($y/D \leq 0.5$). Fig. 5.4(c) shows the increase of particle critical diameter from no-heat release case will be more significant with increasing Damköhler number. Figure 5.5 shows the cross-stream nucleation rate profiles as the flow travels downstream. The effects of heat release on nucleation is negligible at low Damköhler number. WIth increasing Damköhler number, the nucleation rate maintains at a similar level with heat release. However, without heat release, the nucleation rate increase significantly.

Non-dimensional nucleation rate $J^\star$ vs. particle critical diameter d_p is shown in Fig. 5.6 at different Damköhler numbers. Both the nucleation rate and the critical diameter of DBP particles increases with increasing Damköhler numbers. Relatively bigger critical nuclei are formed with heat release because increased kinetic energy of molecules needs to be balanced by larger surface to be stable for future growth. For example, with no heat release effects, the typical values of nucleation are $J^\star = 10^{22}$ at $d_p = 2.1nm$ in case 1 (Fig. 5.6a), and $J^\star = 10^{26}$ at $d_p = 2.4nm$ in case 3 (Fig. 5.6c). At the low Damköhler number in case 1 ($Da = 206.8\times10^2$), the nucleation rates and particle diameters are similar for both the heat-release and no heat-release cases. However, at higher Damköhler numbers (case 2 and case 3), the nucleation rate decreases and the critical diameter increases with heat release. With increasing Damköhler number, the particles being formed with heat-release are larger though produced at a similar rate. For example, the typical values of nucleation rate with heat release effects are $J^\star = 10^{22}$ at $d_p = 2.5nm$ and $J^\star = 10^{22}$ at $d_p = 2.8nm$, in case 2 and case 3 respectively. The critical sizes of DBP nuclei increase with Damköhler number and nucleation heat release. This suggests that the typical method of producing finer particles via faster mixing may not be efficient since the production rate also increases with rapid mixing, and the critical diameter increases with larger Damköhler number.

5.4 Summary and conclusions

Direct numerical simulation of DBP nanoparticle nucleation is performed in three-dimensional laminar planar jets. The Navier-Stokes equations are solved for the fluid dynamics. Both the mass and thermal transport equations are solved for the chemical species and temperature fields. The flows simulated consisted of heated jet flows of DBP vapor diluted in nitrogen issuing into cooler particle-free nitrogen streams. The effects of heat release on fluid dynamics and particle formation are investigated via comparison of cases where heat release is and is not present, at different nucleation Damköhler numbers. The heating effects on the co-flow and the momentum change between the jet and co-flow is analyzed via the cross-stream temperature profiles and jet widths. The effects of the fluid dynamics on DBP particle formation are presented via the nucleation rate, critical particle diameter and the mass flux.

The results show that at low Damköhler numbers both the flow dnamics and nucleation are similar regardless of heat release, indicating that the amount of energy liberated during nucleation is negligible. At higher Damköhler numbers, the temperature increases in the nucleation region. Although the reference Prandtl number is unity, with heat release at high Damköhler numbers the temperature thickness still grows faster than the momentum thickness, or jet half-width. The nucleation heat release at the shear layer inhibits the momentum exchange between jet flow and co-flow. Additionally, the saturation ratio generally decreases with increasing Damköhler number. This is because higher Damköhler numbers represent faster consumption of DBP vapor, and the saturation ratio generally decreases with increasing temperature. Another interesting result is that with heat-release, the nucleation rate maintains a similar level when the Damköhler number increases. However, when heat-release is neglected, the nucleation rate is shown to increase with the nucleation Damköhler number. This reflects the fact that increases in temperature act to suppress nanoparticle nucleation. When this mechanism is neglected, nucleation is significantly over-predicted.

Table 5.1: Simulation cases

Cases	Re	Le	Da
Case 1	200	4	206.8×10^2
Case 2	200	4	206.8×10^6
Case 3	200	4	206.8×10^9

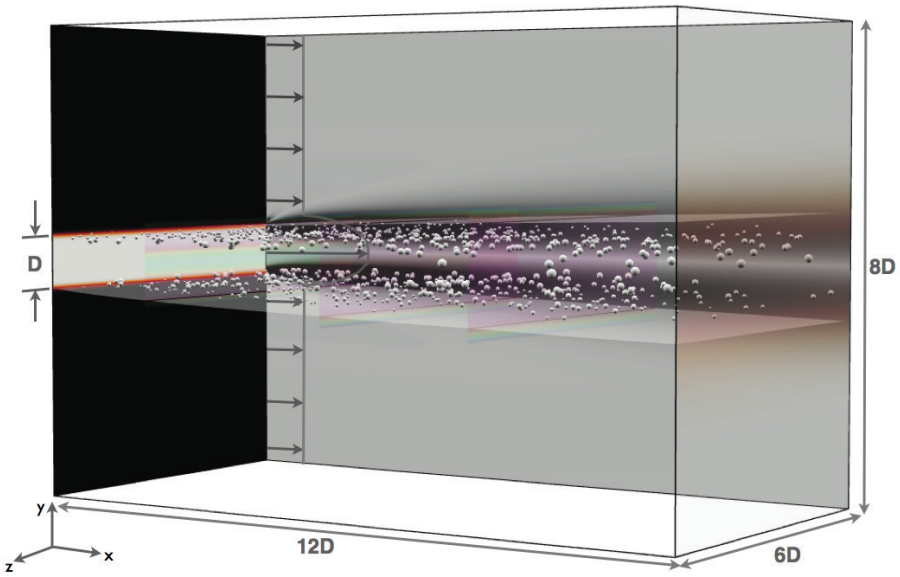

Figure 5.1: Simulation configuration, showing a temperature iso-surface of $340K$, vorticity contour at $z = 0$, temperature contour at $x = 0$, and nucleation rate contour at downstream locations. The silver spheres represent DBP nucleation, where the sphere sizes are scaled to the actual critical diameter of DBP nuclei and the number density is scaled to nucleation rate.

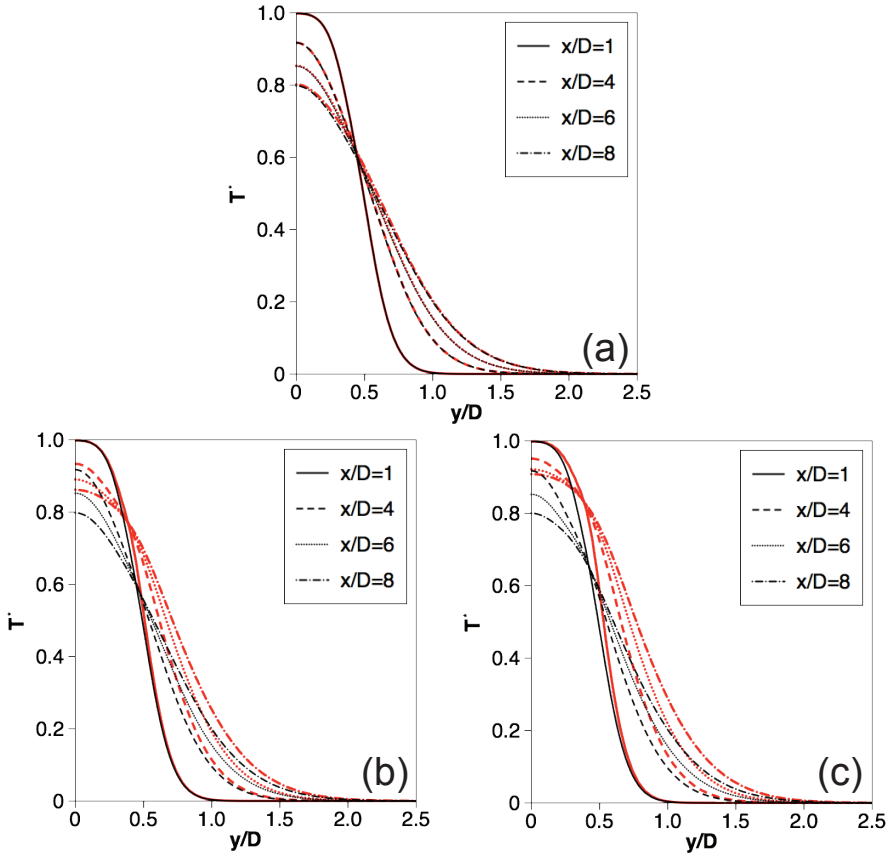

Figure 5.2: Cross-stream profiles of the non-dimensional temperature $T^{\star}$: (a) case 1; (b) case 2; (c) case 3. The red (light) lines indicate cases with heat-release and the black (dark) lines indicate cases without heat-release.

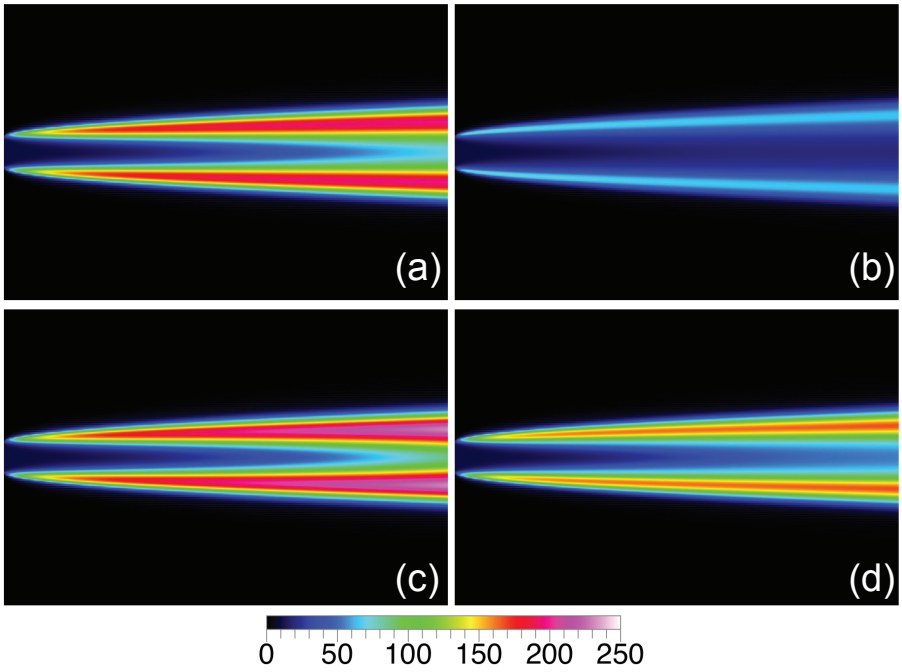

Figure 5.3: Contours of saturation ratio, S: (a) case 1 with heat-release; (b) case 3 with heat-release; (c) case 1 without heat-release; (d) case 3 without heat-release.

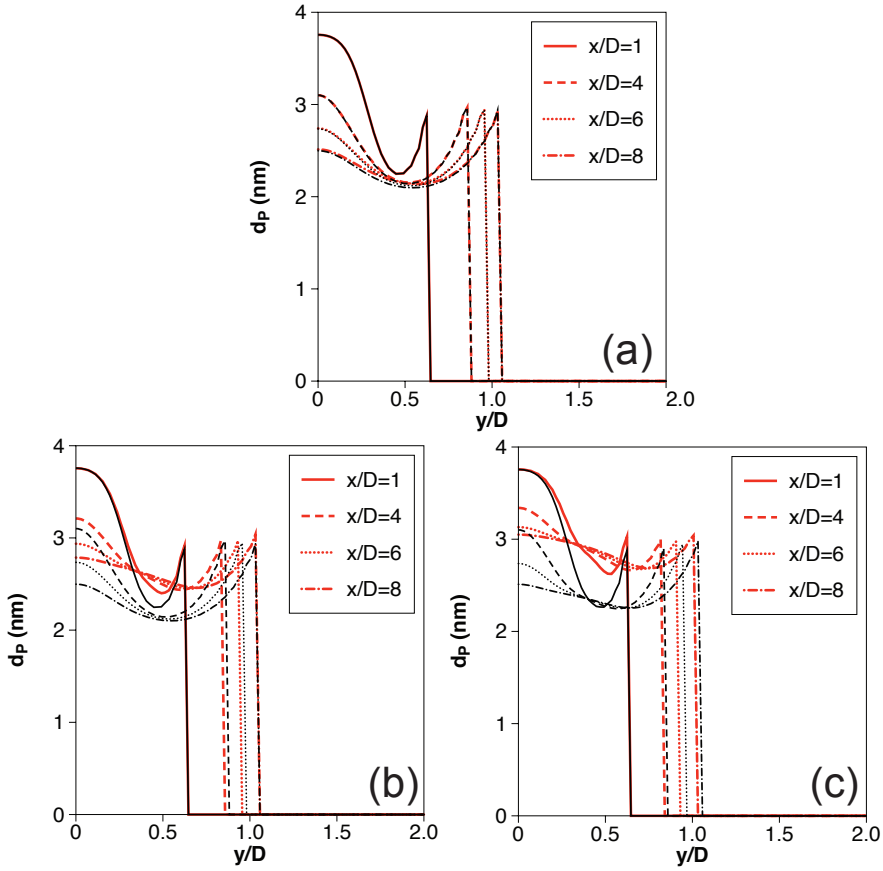

Figure 5.4: Cross-stream profiles of the critical diameter, d_p: (a) case 1; (b) case 2; (c) case 3. The red (light) lines indicate heat-release and the black (dark) lines indicate no heat-release.

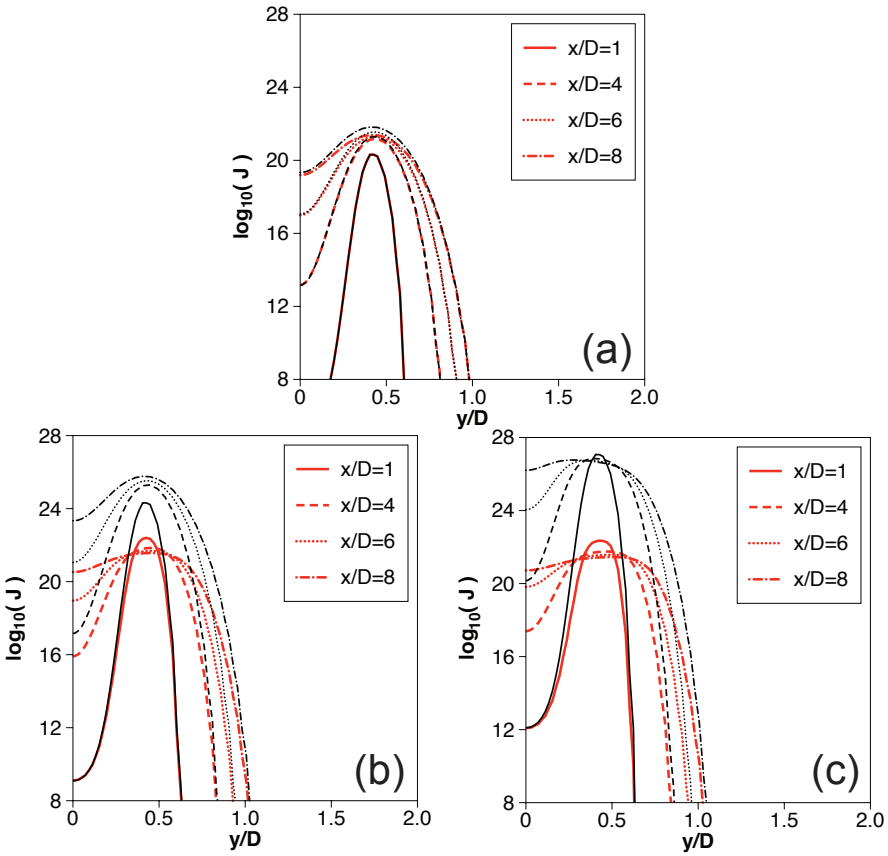

Figure 5.5: Cross-stream profiles of the nucleation rate, J: (a) case 1; (b) case 2; (c) case 3. The red (light) lines indicate heat-release and the black (dark) lines indicate no heat-release.

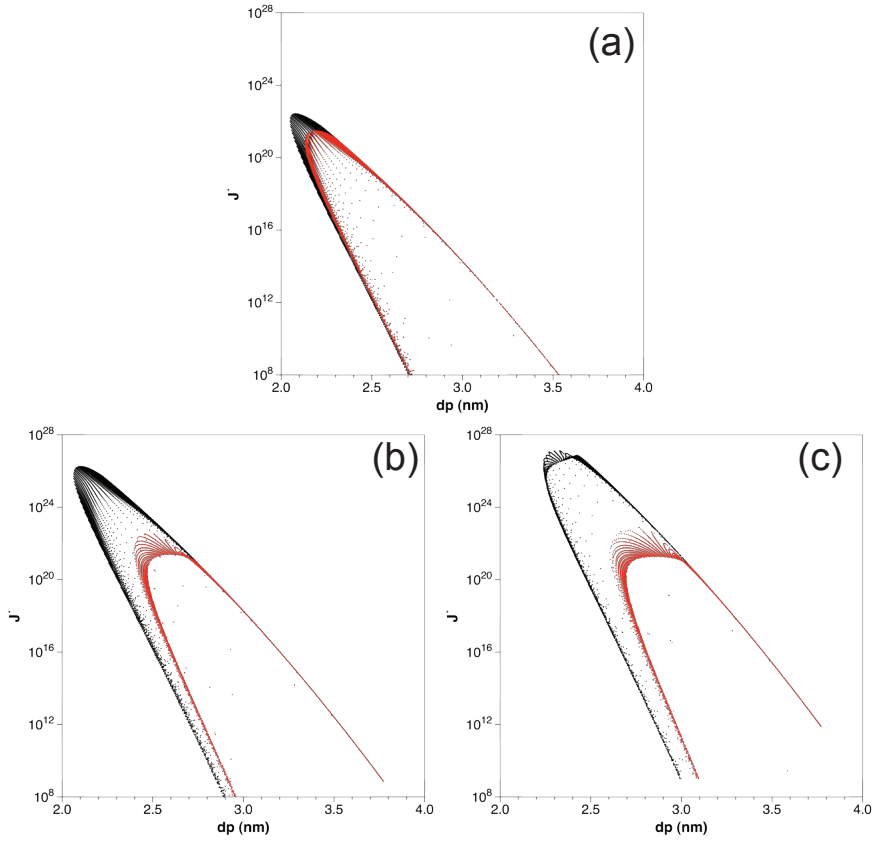

Figure 5.6: Non-dimensional nucleation rate, $J^{\star}$, vs. critical diameter, d_p: (a) case 1; (b) case 2; (c) case 3. The red (light) dots indicate heat-release and the black (dark) dots indicate no heat-release.

Chapter 6

Effects of heat release on dibutyl-phthalate homogeneous nucleation in turbulent flows

Effects of heat release on the interactions of fluid dynamics and nanoparticle formation within turbulent flows are investigated via direct numerical simulations. Simulations are performed for homogeneous nucleation of DiButyl phthalate (DBP) nanoparticle in three-dimensional turbulent planar jet flows. The flows consist of a high-temperature jet stream with DBP vapor diluted in nitrogen gas issuing into a low-temperature particle-free nitrogen co-flow. The fluid, thermal, and chemical transports are obtained via solving the Navier-Stokes, enthalpy, and mass transport equations. The DBP nanoparticle formation is simulated via a self-consistent classical homogeneous nucleation model. The results show that heat release due to nucleation initially occurs in the shear layers, and then vortex cores when the flow transits into turbulence. Pre-transition, the jet flow heats up the co-flow faster and the saturation ratios within shear layers are lower with heat release. Post-transition, the large structures of flow movement break down later and further downstream with heat release. Unlike the case where heat release is neglected and saturation ratios increase with fluid mixing and downstream locations, with heat release the saturation ratios maintain lower but spatially uniform values. The nucleation rates decrease and the critical sizes of nuclei increase. The results indicate

that heat release during nucleation acts to reduce and maintain a uniform distribution of saturation ratios as flows mix. More significantly, with heat release the flows transit into turbulence further downstream, and the nucleation rates maintain lower values. The simulations provide a demonstration of the interactive effects of heat release on fluid evolvement and nucleation, which suggests faster transition into turbulence – which were believed to increase nanoparticle production rate and produce finer particles – may not be effective with heat release.

6.1 Introduction

In many scientific and industrial processes of producing nanoparticle, gas-to-particle phase change in the form of nucleation plays an important role [16, 71]. Properly taking the effects of heat release into account on flow turbulence is an essential bridge between fluid dynamics and particle nucleation, since nucleation is very sensitive to the physical distributions of condensing vapor [74, 42, 75, 22]. Nucleation within flows accompanied by heat release results in variations of fluid temperature, density, and dynamics of flow evolvement [77, 83, 84]. Previous investigations have demonstrated that under low vapor concentration and for some materials, such variations are negligible due to small amount of heat release [76, 85, 22]. However, for nucleation flows accompanied by significant amounts of heat release, heat release plays an important role in the fluid-nucleation interactions. DiButyl Phthalate (DBP) is a commonly used material with relatively high latent heat. Formation of DBP nanoparticles is a challenging problem of interest to many industrial needs [86, 87, 88, 76, 89]. In this paper, we address the effects of heat release on the overall fluid transport and mixing properties during and post transition into turbulence, and from an accurate prediction of nanoparticle formation within complex flow systems [90].

The effects of nucleation heat release on the properties of flow turbulence have been studied extensively, both in experiments and theories. Experiments were performed in a planar reacting mixing layer and showed the growth rate of the layer will decrease with heat release [80]. Effects of heat release also prevented large-scale structures in turbulent mixing layers from breaking into small structures [77]. Heat release in reacting turbulent shear flows indicated the growth of turbulent kinetic energy is caused by

temperature changes [91]. Studies have also shown that heat release affects flow development by limiting the growth of shear layer [77, 80]. Differences observed between the reacting and non-reacting shear flows are reviewed by Dahm *et al.* (2000, 2005) [83, 84]. Properly account for the effects of heat release on particle nucleation is essential when most previous approaches de-couple fluid dynamics and nucleation by superimposing nucleation on pre-solved flow fields. Experiments and simulations were performed in Ludwieg-tube where an increase in both the pressure and temperature is observed in the vortex core with heat release [92]. Growth and transport of droplets in a turbulent environment is reviewed by Wang *et al.* (2012), Guta, A. (2008) and Shaw, R. A. (2003) [93, 90, 69]. However, little is known about the coupled effect of fluid dynamics on particle nucleation due to its coherent complexity. A popular approach is to study the effect of heat release on nucleation mechanism. Molecular dynamics technique shows that the time required to establish equilibrium for gas-particle interactions is smaller with heat release, and the temperature gradient leads to a lower nucleation rate from isothermal classical expression [79, 70]. Hybrid simulations of metal particle nucleation indicates the small scale structures are critical to the particles' properties[23]. Study the effects of heat release on the both the properties of turbulent flows and nucleation is made possible by direct numerical simulation to capture the mixing processes in a model-free manner [22]. No assumptions regarding flow mixing or the nature of scalar transport need to be made and the methodology is potentially beneficial in dealing with the coupling of turbulent flow evolvement and nucleation.

In this work, we utilize direct numerical simulation of DBP nucleation in three-dimensional turbulent planner jet flows to investigate the heat release effects on the interplay of fluid dynamics and nucleation. All physical properties, such as the thermal and physical diffusivity of the DBP-nitrogen flow, are calculated by local temperature and chemical compositions to enhance physical accuracy of flow evolvement. Simulations are conducted both with and without heat release, which allows insight into the heat release effects on properties of turbulent flows. The resultant particles' properties are also analyzed to correctly predict particle size and production rate with heat release.

6.2 Formulation

6.2.1 Fluid and scalar transport

The fluid dynamics are governed by the compressible Navier-Stokes equations. The variables are the fluid density $\rho(\vec{x})$, velocity $u_i(\vec{x})$, pressure $p(\vec{x})$, and the enthalpy $h(\vec{x})$, which are obtained by

$$\frac{\partial \rho}{\partial t} + \frac{\partial \rho u_i}{\partial x_i} = 0, \tag{6.1}$$

$$\frac{\partial \rho u_i}{\partial t} + \frac{\partial \rho u_i u_j}{\partial x_j} = -\frac{\partial p}{\partial x_i} + \frac{\partial \tau_{ij}}{\partial x_j}, \tag{6.2}$$

$$\frac{\partial \rho h}{\partial t} + \frac{\partial \rho u_j h}{\partial x_j} = \frac{\partial}{\partial x_j}\left(\frac{k}{C_p}\frac{\partial h}{\partial x_j}\right) + \dot{Q}, \tag{6.3}$$

where τ_{ij} is the viscous stress tensor, k is the coefficient of thermal conductivity, C_p is the constant pressure specific heat, and $\dot{Q}$ is the enthalpy increase per unit time due to nucleation. The enthalpy h is related to temperature T via $dh = C_p dT$. The equations are closed using the ideal gas relation, $p = \rho RT$ and R is the gas constant.

The transport of DBP vapor mass fraction Y_i is governed by

$$\frac{\partial \rho Y_i}{\partial t} + \frac{\partial \rho u_j Y_i}{\partial x_j} = \frac{\partial}{\partial x_j}\left(\rho D_i \frac{\partial Y_i}{\partial x_j}\right) - \dot{\omega}_i, \tag{6.4}$$

where D_i is the diffusion coefficient and $\dot{\omega}_i$ is the 'sink' term due to nucleation. The enthalpy increase per unit time due to the nucleation process is given by $\dot{Q} = \dot{\omega}_i h_o$, where h_o is the enthalpy of formation of DBP particle per unit mass.

6.2.2 Nucleation modeling

We utilize the nucleation rate predicted by a self-consistent classical nucleation theory [44]. The expression for the nucleation rate J is given by

$$J = \frac{(\rho Y_i)^2}{\rho_i m_i S}\sqrt{\frac{2\sigma}{\pi m_i}}\exp\left(-\frac{\pi\sigma {d_p}^2}{3k_B T} + \frac{\sqrt[3]{36\pi v_i^2}\sigma}{k_B T}\right). \tag{6.5}$$

where S is the saturation ratio, k_B is the Boltzmann constant, m_i is the mass of a vapor molecule, and ρ_i is the density of condensed DBP. The volume per molecule v_i is given

by m_i/ρ_i, σ is the surface tension. The critical size of DBP nuclei d_p is given by the Kelvin relation,

$$d_p = \frac{4\sigma m_i}{k_B T \rho_i \ln(S)}. \tag{6.6}$$

The 'sink' term of DBP vapor mass transport equation (Eq. 6.4) is then given by

$$\dot{\omega}_i = \frac{\pi}{6}\rho_i {d_p}^3 J. \tag{6.7}$$

To parameterize the nucleation process, nondimensional variables (marked with $\star$) can be defined using the following reference values (marked with subscript o) :

$$x_i^\star = \frac{x_i}{L_o},\ \ u_i^\star = \frac{u_i}{U_o},\ \ \rho^\star = \frac{\rho}{\rho_o},\ \ Y^\star = \frac{Y}{Y_o},\ \ \rho_i^\star = \frac{\rho_i}{\rho_{io}},\ \ \sigma^\star = \frac{\sigma}{\sigma_o}, \tag{6.8}$$

where L_o is the reference length scale, U_o is the reference velocity, ρ_o and ρ_{io} are the reference density for the fluid and DBP particles, respectively. Y_o is the reference value of DBP vapor mass fraction, and σ_o is the reference value of DBP surface tension. The non-dimensional nucleation rate $J^\star$ is given by $J^\star = J \cdot L_o/(\rho_o U_o)$. The non-dimensional nucleation 'sink' term $\dot{\omega}_i^\star$ in the transport equation of DBP vapor is given by

$$\dot{\omega}_i^\star = \frac{L_o}{U_o \rho_o}\frac{\pi}{6}\rho_i d_p^3 J, \tag{6.9}$$

where the number nucleation rate J and particle critical diameter d_p are given by Eq. 6.5 and Eq. 6.6 respectively, which yields

$$\dot{\omega}_i^\star = Da \cdot \left(\frac{\sigma^\star}{\rho_i^\star T^\star \ln(S)}\right)^3 \frac{(\rho^\star Y^\star)^2\sqrt{\sigma^\star}}{S} \exp\left(-\frac{\pi\sigma {d_p}^2}{3k_B T} + \frac{\sqrt[3]{36\pi v_i^2}\sigma}{k_B T}\right). \tag{6.10}$$

The nucleation Damköhler number, Da, which includes all the reference parameters and reflects dependence of specific flow-nucleation system, is then given by

$$Da = \frac{L_o}{6U_o\rho_o}\left(\frac{(\rho_o Y_o)^2}{m_i^{3/2}}\sqrt{2\pi\sigma_o}\right)\left(\frac{\sigma_o m_i}{\rho_{io} k_B T_o}\right)^3, \tag{6.11}$$

the value of Da represents the magnitude of nucleation rate.

6.3 Results

6.3.1 Flow configuration

The flows consist of a three dimensional planar jet with a nozzle width of D. A schematic of the flow configuration is shown in Fig. 6.1. Jet flow with velocity U_o issues into a co-flowing particle-free nitrogen stream with velocity U_∞. The velocity ratio is $U_o/U_\infty = 3.0$. The temperature of the heated jet flow is T_o and the temperature of the cooler nitrogen stream is T_∞, where $T_o = 400K$ and $T_\infty = 300K$. The mass fraction of DBP vapor at the inlet of the jet is Y_o.

6.3.2 Physical assumptions and numerical specifications

The Reynolds number, $Re = U_o D/\nu = 4000$, is the ratio of inertial to diffusive forces, where ν is the kinematic viscosity. The Lewis number, $Le = Sc/Pr = 4$, represents the ratio of thermal diffusivity to mass diffusivity. The values of all parameters are listed in Table 6.1. Nucleation with or without heat release is simulated via $\dot{Q} = \dot{\omega}_i h_o$ or $\dot{Q} = 0$. All physical properties of the particles and the gas mixtures are calculated based on both local temperature T, and the mass fraction of each chemical species Y_i. The properties of DBP are taken from previous work [81, 82, 27]. The DBP condensed phase density is given by $\rho_i = 1063 - 0.826\,(T - 273.16)\,kg/m^3$, its surface tension is $\sigma = 0.0353 - 0.0000863\,(T - 273.16)\,N/m$, and the saturation mole fraction is given by $x_{sat} = \exp\,(21.497 - 11497/T)$. A typical volume fraction of particles within the flow is 10^{-6} at maximum, so that the momentum transport between particles and fluids are negligible. All time and length scales are resolved explicitly in numerical simulations. No assumptions about the flow structures nor the molecular mixing processes are made to enhance the fidelity of nucleation-fluid dynamics interaction analysis. The convective time scale $\tau_c = D/U_o = 5.7 \times 10^{-6}s$, and the time scale required to reach steady sate nucleation is in the order of $10^{-8}s$, which validate the use of steady state nucleation rate expression [68].

The governing equations for the flow, thermal and chemical transport are solved by a fourth order accurate hybrid MacCormack-based, predictor-corrector scheme [58, 59]. Simulations are performed on a domain of $20D \times 12D \times 8D$, in x, y and z directions respectively. The resolution for all simulations is $1280 \times 640 \times 480$. The grid is clustered

about the shear layers and each simulation performed requires roughly 60,000 CPU-hours.

6.3.3 Effects of heat release on scalar transport

The most direct results of heat release on fluid dynamics are the variations of temperature, thermal energy and condensing vapor mass transports. Figure 6.2(a) shows the cross-stream profiles of the time-averaged normalized temperature $T^\star$ at several downstream locations. With heat release, the core of the jet ($y = 0$ and $z = 0$) maintains a relatively higher temperature, which indicates the cooling of jet is limited by nucleation heat release. For example, at downstream location ($x/D = 16$) and the center of the jet, with heat release the temperature $T^\star = 0.75$ is 30% higher than the temperature at the same location ($T^\star = 0.58$) when heat release is neglected. The thermal energy transports into the co-flow faster with heat release, by heating up the co-flow. At the edge of the jet ($y/D = 1$) and downstream location ($x/D = 12$), the temperature with heat release is $T^\star = 0.65$, when without heat release the temperature is $T^\star = 0.45$ at the same location. More significantly, with heat release, the temperature distribution expands as the jet travels downstream, while the values remains similar values within the jet after $x/D = 8$. However without heat release, the temperature distribution expands in width while the interior of the jet is cooled down. Similar trends can be found for the mass transport of DBP vapor in Fig. 6.2(b). The cross-stream profiles of the time-averaged normalized DBP vapor mass fraction $Y^\star$ at several downstream locations are shown. The mass fraction at the center of the jet is higher with heat release. At $x/D = 12$ and the center of the jet ($y/D = 0$), the mass fraction with heat release $Y^\star = 0.68$ is 17% higher than the value without heat release ($Y^\star = 0.58$). The distribution of DBP vapor expands as the flow travels downstream via both molecular mixing and convective transport by turbulence. After $x/D = 12$ and the flow transits into turbulence. With heat release, the DBP mass fraction at the center of the jet drops 50% from $x/D = 4$ to $x/D = 16$ when without heat release the drop will be 60%. Heat release not only affects cooling process by shifting temperature within the jet, but also affected the mass dilution transport by varying the evolution of flow structures and mixing processes.

The instantaneous contours of the temperature distribution at $z = 0$ is shown in Fig.

6.3. Generally the development of the nucleation flow can be divided into three stages. Pre-transition, which correspond to the region between the jet inlet and $x/D = 4$, where the flow is generally laminar with instabilities forming. Molecular diffusion is the major effect of mixing within the region. The transition region, which appears near $x/D = 4$ without heat release but not until $x/D = 5$ with heat release, in both cases the eddy structures of the flows appear, evolve and migrate as the flow travels. With heat release, not only more thermal energy is transported into the co-flowing stream by heating up further into the co-flow, the large-scale structures break into small-scale ones further downstream. For example, eddy structures after $x/D = 10$ of the jet are larger in Fig. 6.3(a), where heat release is considered. With no heat release, the large structures of the flow begin to break into smaller ones from $x/D = 10$. The eddy structures bring in the cooler co-flow into the core of the jet and increase the cooling effects. Convective transport is the major effect of mixing within the region. Post-transition, which appears from about $x/D = 10$ without heat release and about $x/D = 14$ with heat release, where more small structures of the flow will be more efficient to dissipate the thermal energy into co-flow and effectively cool down the jet flows. The temperature within the eddies after $x/D = 14$ in Fig. 6.3(a) are relatively higher than those in Fig. 6.3(b). For example at $x/D = 18$, the temperature in the eddies are $T^\star = 0.8$ with heat release and $T^\star = 0.6$ without heat release. The results indicate that heat release via nucleation causes slower and further downstream break-down of the large flow structures as compared to no heat release assumptions, which effectively causes less efficient cooling of the jet flows. The commonly used approach of neglecting heat release might have over-predicted the cooling of the condensing flow.

6.3.4 Effects of heat release on nucleation

Saturation ratio acts as the bridge between nucleation and fluid dynamics via a combination of dilution and cooling effects of the flow. The time-averaged saturation ratio distributions at several downstream locations are shown in Fig. 6.4. With heat release, the saturation ratios are lower in general. For example, at downstream location $x/D = 12$ and the center of the jet ($y/D = 0$), saturation ratio is ≈ 60 without heat release and ≈ 25 with heat release. As the jet travels downstream, the supersaturated region expands into the co-flow. Without heat release, the typical value of saturation

ratio increases however without heat release, the saturation ratios after $x/D = 4$ maintain a lower but stable value between $S = 20$ and $S = 30$. After $x/D = 4$ and without heat release, the saturation ratios generally increase with downstream locations. For example at the edge of the jet ($y/D = 1$), the saturation ratio is $S = 40$ at $x/D = 8$ and $S = 70$ at $x/D = 16$. The transition of flow into turbulence has a significant impact on saturation ratio by increasing it when heat release is neglected, however it is not necessarily the same with heat release. In another word neglecting heat release might over-predict the saturation ratio within the nucleation flow.

Figure 6.5 shows the instantaneous vorticity iso-surface colored with saturation ratios. For both cases with and without heat release, the saturation ratios increase as jet evolves and travels downstream. A typical value of saturation ratio with heat release in Fig. 6.5(a) is $S < 50$. Pre-transition, the saturation ratio values at the surface is higher without heat release. For example, for the large structures of eddies at $x/D = 8$, the saturation ratio at the surface is $S = 50$ in Fig. 6.5(a) while $S = 100$ in Fig. 6.5(b). However post transition, without heat release, saturation ratio is generally higher since more small-scale structures appear in Fig. 6.5(b), near the outlet of the jet, which result in faster mixing and cooling of the condensing vapor. Especially at the small structures, very high saturation ratio could be found in Fig. 6.5(b) but rarely in Fig. 6.5(a), high saturation ratios in Fig. 6.5(b) are found on vortical braids, where cooler co-flow is brought into the cores of eddies where vapor mass fraction is still high. The fast cooling via such vortical braids usually result in high saturation ratio. The results indicate that with no heat release assumption, the saturation ratios within the flow is generally over-predicted, especially in the turbulent mixing stage, where the assumption might lead to significant variations in predicting saturation ratios.

Higher saturation ratios do not necessarily result in higher nucleation rates. Figure 6.6 shows the cross-stream profiles of time-averaged non-dimensional nucleation rates $J^\star$. The average nucleation rates with heat release at downstream locations ($x/D > 4$) are $J^\star = 10^{20}$, which are 5 orders of magnitudes lower than the case without heat release ($J^\star = 10^{25}$). The expansion of nucleation region spatially in y direction is slightly slower when heat release is considered. However the results also show nucleation happens through the cross-section of the jet at downstream locations ($x/D > 4$), rather than only the shear layers as in laminar nucleation jets and chemical reacting flows

[22]. So that heat sources caused by nucleation at downstream locations are uniformly distributed, which is quite different from most reacting flows where local expansion within thin shear layers has significant impact on flow instability.

Figure 6.7 shows the instantaneous vorticity iso-surface colored with nucleation rates. Nucleation rates are highest along interface of jet and co-flowing stream, and mostly vortical braids where cooler co-flow is brought into contact with condensing vapor at the cores of eddies. High saturation ratios do not necessarily lead to high nucleation rate. Nucleation initially occurs also in the shear layers, and then vortex cores when the flow transits into turbulence. As the flows travel downstream, with heat release, as shown in Fig. 6.7(a), large scale flow structures breaks into smaller ones later downstream and convective mixing processes still take the majority places. In Fig. 6.7(b), small flow structures begin to appear after $x/D = 6$, and as the flow travels the small scale turbulent mixing effects take the majority places. At the same time the nucleation rate, J with heat release on the same magnitude of vorticity is about 5 times of magnitudes lower than the case without heat release.

6.3.5 Jet growth and particle properties

The jet growth by half-width σ and temperature thickness δ_T are presented in Fig. 6.8. The jet half-width σ is defined as the distance between the cross-stream locations in y direction where the time-averaged x-direction velocity equals to half of the central line value. The temperature thickness δ_T is defined as the distance between the cross-stream locations in y direction where the temperature $T = T_\infty + 0.1 \cdot (T_o - T_\infty)$. The results indicate that the jet grows at similar rates as the flows develops, both with and without heat release as shown in Fig. 6.8(a). Unlike reacting jet flows where heat release and local expansion only happen at the thin shear layers, in nucleation flow the heat release appears across the stream (Fig. 6.6). The heat release does not affect the growth of the jet flows significantly. At the same time as shown in Fig. 6.8(b), the temperature thickness growth of the jets do not vary significantly with heat release either. Since after $x/D = 4$, cooling is either majorly caused by convective mixing in the transient region or turbulent mixing by small structures in the post-transition region, where molecular mixing is less important. Thermal transport within turbulent nucleation flows is not much faster than the jet growth as in laminar flows where molecular mixing is the major

effect of cooling.

The scalar plots of the non-dimensional nucleation rate $J^\star$ and the critical particle diameter d_p are shown in Fig. 6.9. Each point represents a spatially grid within the flow where nucleation take place. Figure 6.9(a) shows with heat release, the majority of particles are formed between the sizes of $d_p = 2.2$ and $d_p = 3.4$ with the nucleation rate $J^\star = 10^{16}$ and above. Figure 6.9(b) shows with heat release, the majority of particles are formed between the sizes of $d_p = 2.0$ and $d_p = 3.0$ with the nucleation rate $J^\star = 10^{22}$ and above.Heat release acts to decrease particle formation and increase critical diameter, or in another word, simulations that neglect heat-release over-predict particle formation and under-predict particle sizes. The scalar plots of the temperature $T^\star$ vs. vapor mass fraction $Y^\star$ are shown in Fig. 6.10. With heat release, the temperature is generally higher when the mass fractions $Y^\star$ are the same. For example at the mass fraction $Y^\star = 0.5$, the temperature $T^\star$ with heat release is $T^\star = 0.8$ in average and the temperature $T^\star$ without heat release is $T^\star = 0.7$ in average. Not only the cooling of the jet is limited by nucleation heat release, the vapor dilution via mass transport, which is represented by the number density of the scalar points, show that the majority of the flow remains less diluted (higher $Y^\star$) with heat release than the case where heat release is neglected. The nucleation rate decreases with heat release too. The results indicate that, with the assumption of neglecting heat release in nucleation flows, one might have significantly over-predicted the production rate of nanoparticles, and the resultant particles' sizes might have been underestimated too.

6.4 Summary and conclusions

Direct numerical simulation of DBP nanoparticle nucleation is performed in three-dimensional turbulent planar jets. Navier-Stokes equations are solved for the flow dynamics. The mass the thermal transport equations are solved for the species and temperature fields. The flows consist of heated jet flows of DBP vapor diluted in nitrogen issuing into cooler particle-free nitrogen streams. The effects of heat release on fluid dynamics and particle formation are investigated via comparison of cases where heat release is and is not present. The heating effects on the co-flow and the growth of the jet is analyzed via the cross-stream temperature profiles, jet half-widths and jet

temperature thicknesses. The effects of the fluid dynamics on DBP particle formation are presented via the nucleation rate and critical particle diameter. Before the flows transit into turbulence, the jet flow heats up the co-flow faster and the saturation ratios within shear layers are lower with heat release. In transition, the large structures of flow break down later and further downstream with heat release. Post-transition and with heat release, the saturation ratio is much lower with less small structures.

The results show that temperature increases in the region where nucleation takes place, and saturation ratio decreases. Before transition into turbulence where molecular mixing is still the major effect of cooling and diluting, the jet heats up the co-flow faster with heat release and the instability structures appear relatively later, which is suitable to the previous findings that heat release will "laminarize" the flow. However during and past transition, with heat release the jet grows at similar rate, both for jet half-width and the temperature thickness, as the case where heat release is neglected. The results indicate that more significantly, unlike most turbulent reacting flows, heat-release does not "laminarize" the flows by preventing large scale structures from further developing since nucleation happens everywhere across the jet rather than only the thin shear layers. Jets without heat release have more small-scale structures at downstream locations, which results in more cooling and diluting at small spatial scales, such faster cooling of condensing vapor will result in high variation of saturation ratios too. Heat release causes higher temperature within eddies and slower break-down, which also result in a lower but more uniformly distributed saturation ratio. The nucleation rates are lower and does not increase significantly with further mixing as flows transit into turbulence. The results indicate that coupling fluid dynamics and nucleation is essential to properly account for the effects of heat release on particle production. Especially with the assumption of no heat release, the values of saturation ratios and their variations within the nucleation flow might have been much over-predicted.

Heat release also have a significant effects on particle nucleation, decoupled fluid-thermal-particle fields may lead to incorrect predicted particle size distributions. With the assumption of neglecting heat release within nucleation flows, one might have significantly over-predicted the production rate of nanoparticles, and the resultant particles' sizes might have been underestimated.

Table 6.1: Simulation cases

Cases	Re	Le	Da	heat release
Case A	4000	4	206.8×10^9	with heat release
Case B	4000	4	206.8×10^9	no heat release

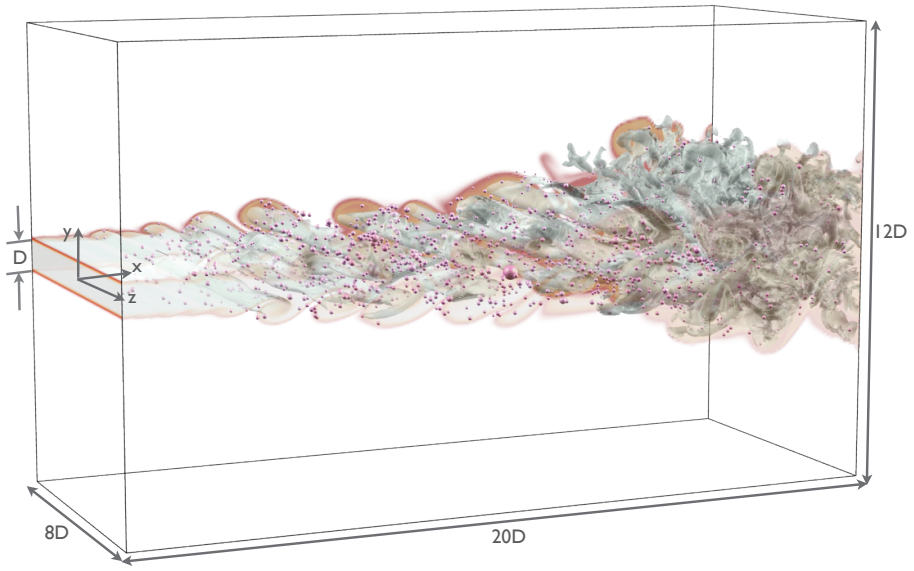

Figure 6.1: Simulation configuration, showing a vorticity isosurface of $\Omega = 1.8$, temperature contour at $x = 0$ and $z = 0$. The spheres represent DBP nucleation, where the sphere sizes are scaled to the actual critical diameter of DBP nuclei and the number density is scaled to the nucleation rate.

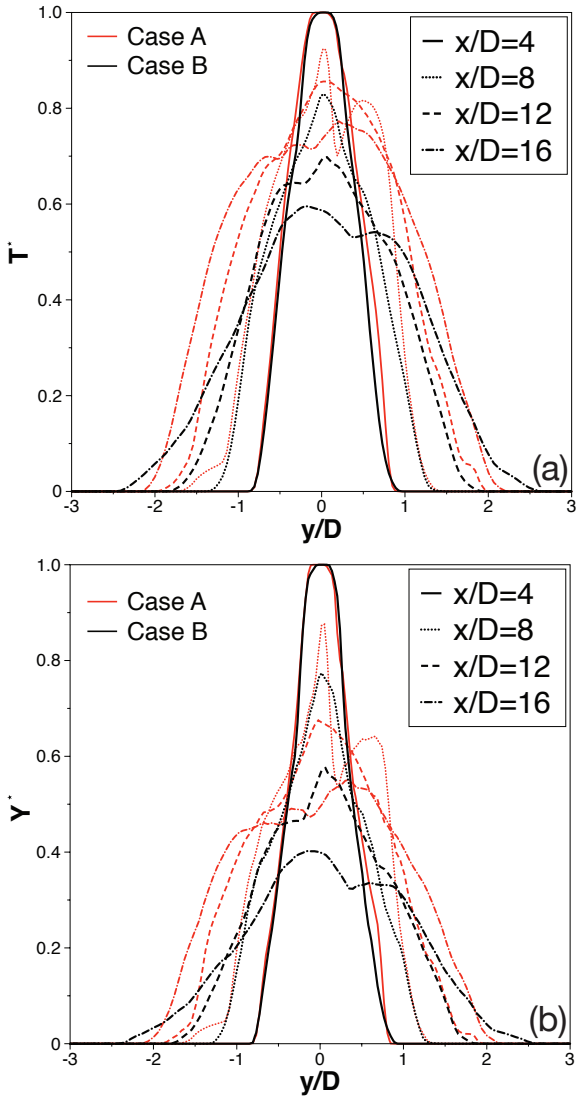

Figure 6.2: Cross-stream profiles of the time-averaged normalized (a) temperature $T^\star$ and (b) DBP vapor mass fraction $Y^\star$.

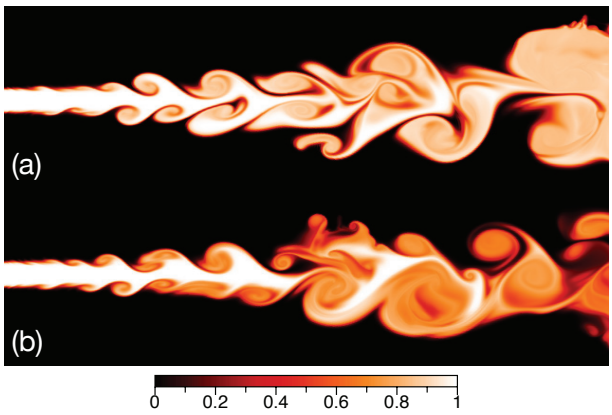

Figure 6.3: Instantaneous contours of the normalized temperature $T^\star$ at $z = 0$: (a) Case A; (b) Case B.

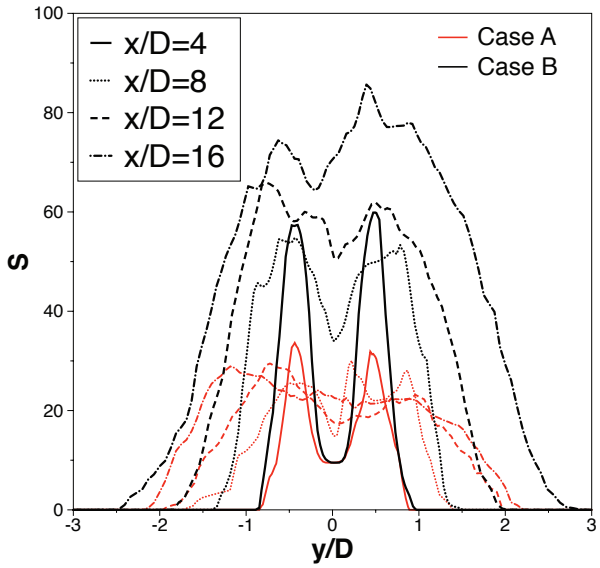

Figure 6.4: Cross-stream profiles of the time-averaged saturation ratio S.

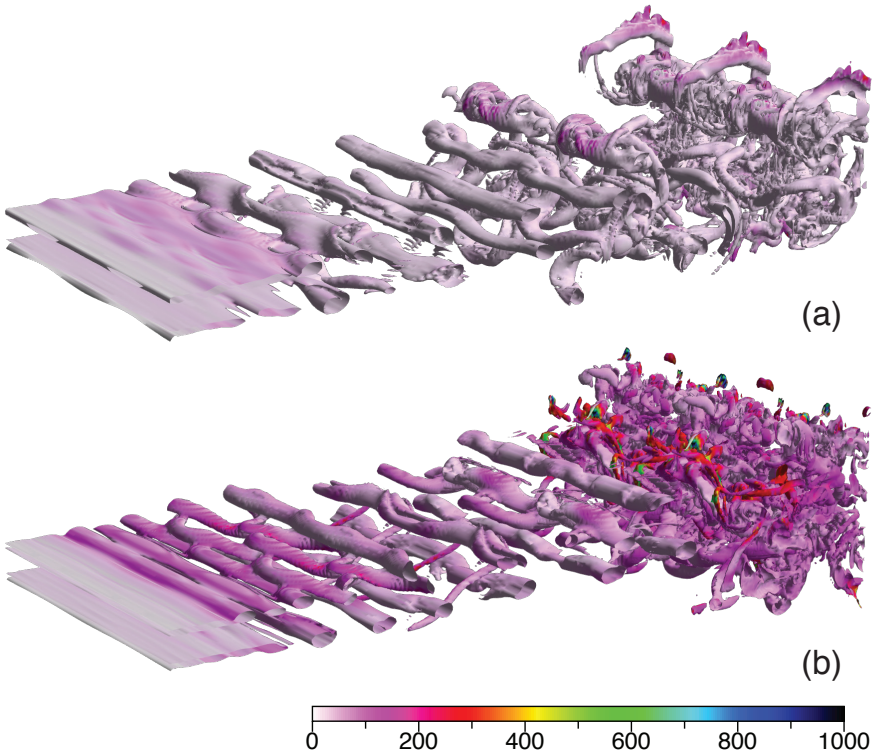

Figure 6.5: Instantaneous vorticity iso–surface ($\Omega = 1.8$) colored with saturation ratio S: (a) Case A; (b) Case B.

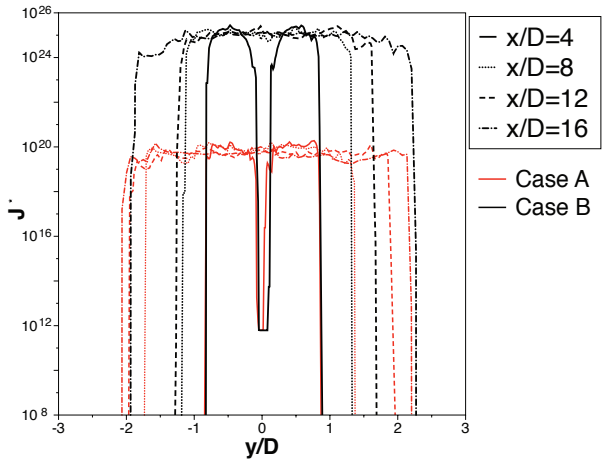

Figure 6.6: Cross-stream profiles of the time-averaged nucleation rate $J^{\star}$.

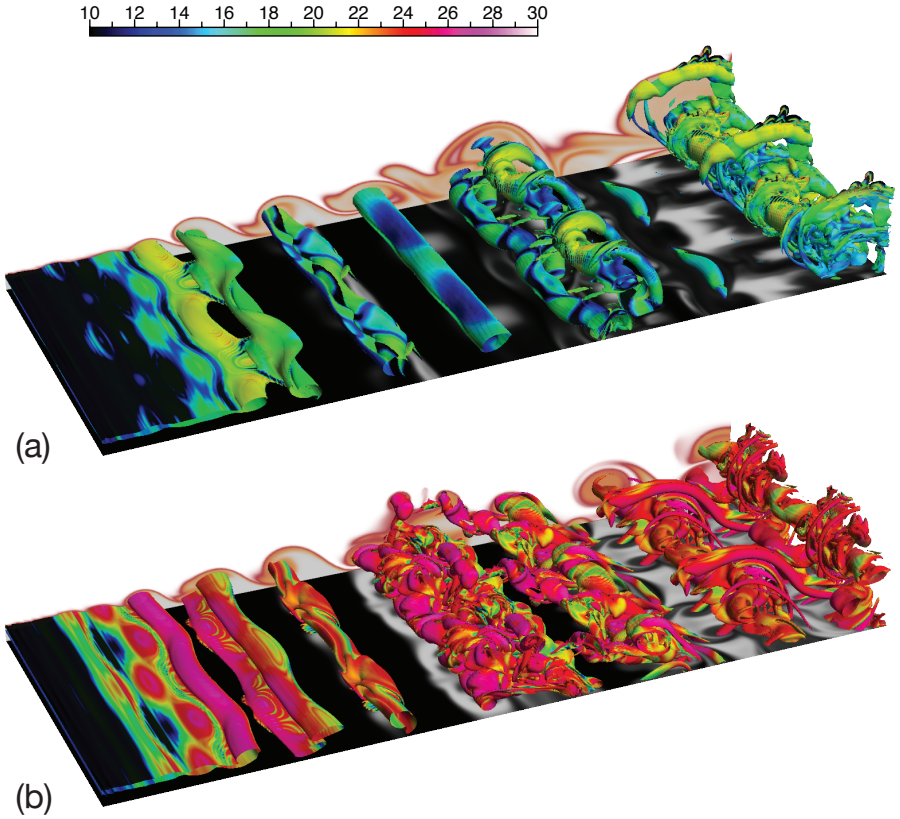

Figure 6.7: Instantaneous vorticity iso–surface ($\Omega = 1.8$) colored with nucleation rate $\log_{10}(J^\star)$, temperature contours at $z = 0$ and $y = 0$: (a) Case A; (b) Case B.

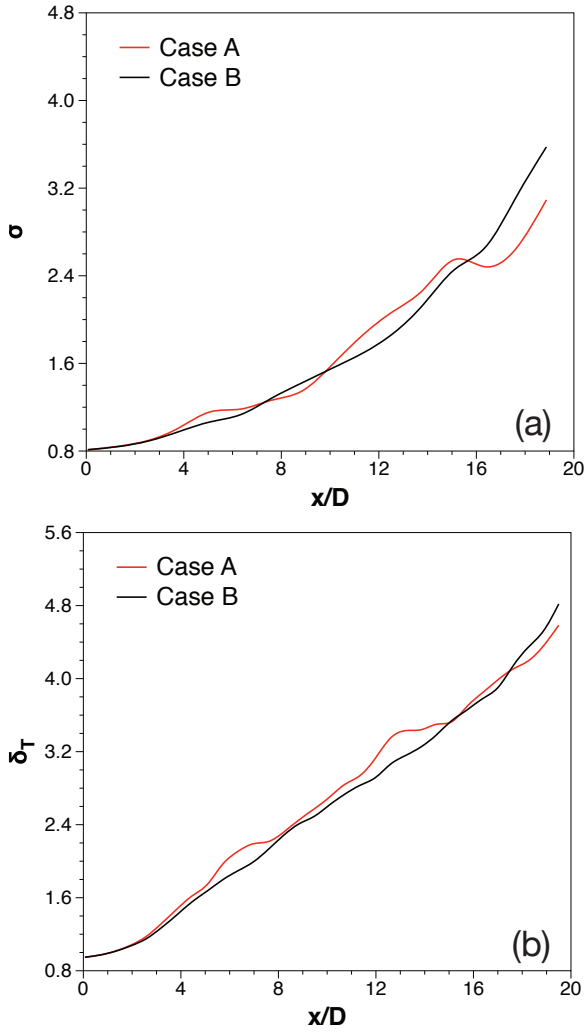

Figure 6.8: Growth of (a) jet half width σ and (b) temperature thickness δ_T as a function of stream-wise location x.

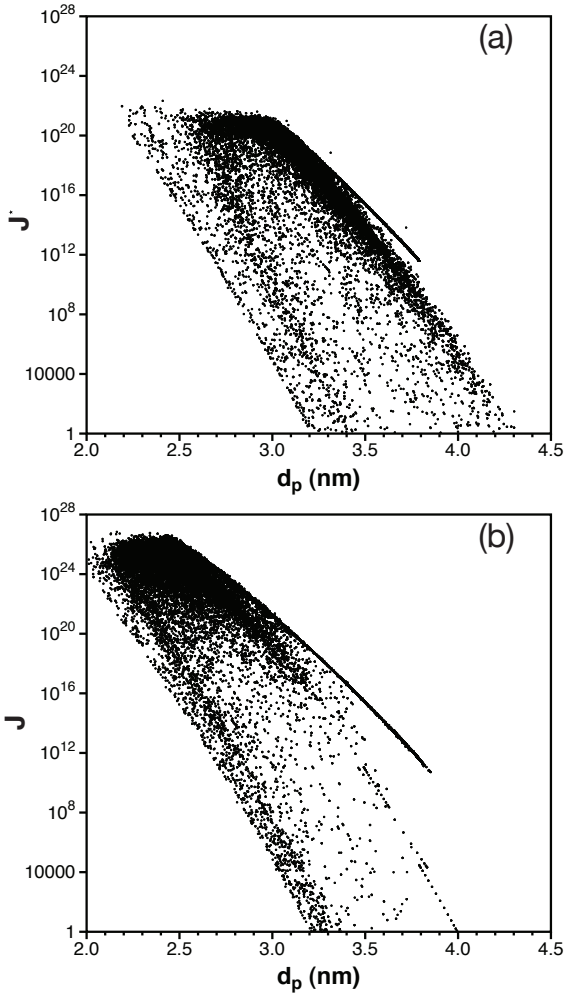

Figure 6.9: Scatter plots of the nucleation rate $J^\star$ as a function of critical diameter d_p: (a) Case A; (b) Case B.

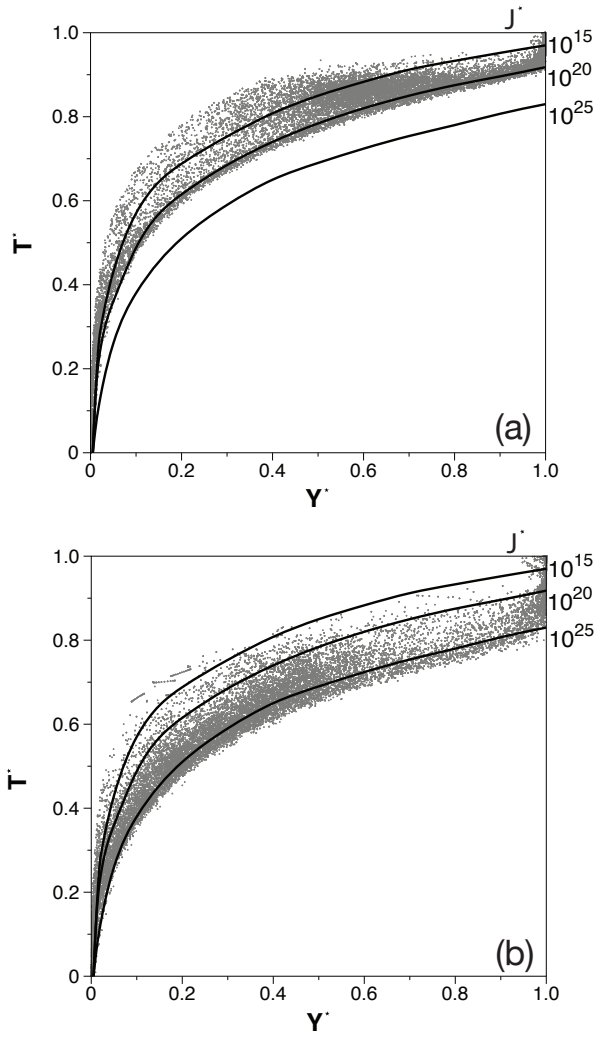

Figure 6.10: Temperature – mass fraction ($T^\star - Y^\star$) maps with lines of constant nucleation rate ($\log_{10}(J^\star)$): (a) Case A; (b) Case B.

Chapter 7

Conclusion and future directions

The objective of this work is to form a more accurate description for nanoparticle formation processes with complex practical flow systems, with properly account for the interactions of fluid dynamics and nucleation. We firstly have performed direct numerical simulations of metal nanoparticle nucleation in laminar and turbulent jets, using the recently developed size-dependent surface tension homogeneous nucleation model. An important result of this work is the notion that increased mixing — mass/chemical mixing as well as energy/temperature mixing — can lead to reduced nucleation rate. This work suggests that while rapid mixing and transition into turbulence do generate high saturation ratios, it may do so in regions where the vapor concentration is too low for particles to be formed.

Secondly, in order to better understand the interactions of flow dynamics and nucleation, especially to properly account the effect of heat release on nucleation, direct numerical simulation of DBP nanoparticle nucleation is performed in three-dimensional laminar and turbulent planar jets. The results indicate that coupling fluid dynamics and nucleation is essential to properly account for the effects of heat release on particle production. Especially with the assumption of no heat release, the values of saturation ratios and their variations within the nucleation flow might have been much over-predicted. Decoupled fluid-thermal-particle fields may lead to incorrect predicted particle size distributions. With the assumption of neglecting heat release within nucleation flows, one might have significantly over-predicted the production rate of nanoparticles, and the resultant particles' sizes might have been underestimated.

Based on the methodologies developed here, many challenging prospective works described below could be done in near future, which would lead to significant physical insights into the behavior of nanoparticle formation with complex flow systems.

- Direct numerical simulations (DNS) of more complex flow systems at practical length scales. As the computational power grows faster, we are able to solve all time and length scales involved in these processes, which are very sensitive to small fluctuations. The methodology studied here could be used to study the complete formation and growth process of nanoparticles of various materials via nucleation, coagulation and condensation.

- Enriched environmental applications by studying the formation of clouds. Based on recent research, the effect of turbulence on cloud formation and its impact on global climate is a topic which can be resolved using the above techniques to evaluate the effects of unresolved sub-grid scale mixing [37].

- Base on the three-dimensional direct numerical simulation results as the "bench" simulations, we can evaluate the effects of turbulent mixing models on the nucleation simulations. DNS is possible for simple flows, such as the round jet in this study. However, it quickly becomes impossible for flows of practical, engineering interest where complex geometries, thermochemistry, and fluid-particle/particle-particle interactions may exist simultaneously. For these engineering flows, large eddy simulation and Reynolds-averaged Navier-Stokes simulations — with the appropriate closures – are practical alternatives, and the methodologies used here can be used to test the fidelity of such turbulent mixing models;

- With the development of supercomputers, more economic methods such as the probability density function method can be employed under more complex flow conditions other than simple jet flows. Computational fluid dynamics will become a more powerful tool in prediction nanoparticle formation processes within various flow systems.

References

[1] F. T. Ferguson and J. A. Nuth III. Experimental studies of the vapor phase nucleation of refractory compounds. v. The condensation of lithium. *J. Chem. Phys.*, 113:4093–4102, 2000.

[2] F. T. Ferguson, J. A. Nuth III, and L. U. Lilleleht. Experimental studies of the vapor phase nucleation of refractory compounds. iv. The condensation of magnesium. *J. Chem. Phys.*, 104(9):3205–3210, 1996.

[3] A. A. Onischuk, P. A. Purtov, A. M. Baklanov, V. V. Karasev, and S. V. Vosel. Evaluation of surface tension and Tolman length as a function of droplet radius from experimental nucleation rate and supersaturation ratio: Metal vapor homogeneous nucleation. *J. Chem. Phys.*, 124(014506), 2006.

[4] A. Berman and M. Epstein. The kinetics of hydrogen production in the oxidation of liquid zinc with water vapor. *International Journal of Hydrogen Energy*, 25:957, 2000.

[5] E. A. Fletcher and R. L. Moen. Hydrogen and oxygen from water. *Science*, 197:1050–1056, 1977.

[6] J. Williams, R. Lansdown, R. Sweitzer, M. Romanowski, R. LaBell, R. Ramaswami, and E. Unger. Nanoparticle drug delivery system for intravenous delivery of topoisomerase inhibitors. *Journal of Controlled Release*, 91:167–172, 2003.

[7] W. H. D. Jong and P. J. Borm. Drug delivery and nanoparticles: applications and hazards. *International Journal of Nanomedicine*, 3:133–149, 2008.

[8] H. Hahn. Gas phase synthesis of nanocrystalline materials. *NanoStructured Materials*, 9:3–12, 1997.

[9] F. E. Kruls, H. Fissan, and A. Peled. Synthesis of nanoparticles in the gas phase for electronic, optical and magnetic applications–a review. *J. Aerosol Sci.*, 29:511, 1998.

[10] H. K. Kammler, L. Madler, and S. E. Pratsinis. Flame synthesis of nanoparticles. *Chemical Engineering and Technology*, 24:583–596, 2001.

[11] K. Wegner, B. Walker, S. Tsantilis, and S. E. Pratsinis. Design of metal nanoparticle synthesis by vapor flow condensation. *Chemical Engineering Science*, 57:1753–1762, 2002.

[12] M. T. Swihart. Vapor-phase synthesis of nanoparticles. *Current Opinion in Colloid and Interface Science*, 8:127, 2003.

[13] W. Ekardt. Size-dependent photoabsorption and photoemission of small metal particles. *Phys. Rev. B*, 31(10):6360, 1985.

[14] D. W. Oxtoby and D. Kashchiev. A general relation between the nucleation work and the size of the nucleus in multicomponent nucleation. *J. Chem. Phys.*, 100(10):7665–7671, 1994.

[15] R. C. Tolman. The effect of droplet size on surface tension. *J. Chem. Phys.*, 17(333), 1949.

[16] S. K. Friedlander. *Smoke, dust and haze: fundamentals of aerosol dynamics*. Oxford University Press, New York, 2nd edition, 2000.

[17] I. M. Kennedy. Flow field effects on nucleation in a reacting mixing layer. *Phys. Fluids A.*, 28:3515, 1985.

[18] J. A. Nuth and B. Donn. Experimental studies of the vapor phase nucleation of refractory compounds. i. The condensation of SiO. *J. Chem. Phys.*, 77(5):2639–2646, 1982.

[19] J. A. Nuth and B. Donn. Experimental studies of the vapor phase nucleation of refractory compounds. II. The condensation of an amorphous magnesium silicate. *J. Chem. Phys.*, 78(3):1618–1620, 1983.

[20] F. Romer and T. Kraska. Homogeneous nucleation and growth in supersaturated zinc vapor investigated by molecular dynamics simulation. *J. Chem. Phys.*, 127(234509), 2007.

[21] J. Pyykonen and S. C. Garrick. Direct numerical simulation of homogeneous nucleation during mixing and cooling. *J. Aerosol Sci.*, 2008.

[22] J. Liu and S. C. Garrick. Metal particle nucleation in laminar jets. *Phys. Fluids*, 24(7):073304, 2012.

[23] A. J. Fager, J. Liu, and S. C. Garrick. Hybrid simulations of metal particle nucleation: A priori and a posteriori analyses of the effects of unresolved scalar interactions on nanoparticle nucleation. *Phys. Fluids*, 24:075110, 2012.

[24] S. Das and S. C. Garrick. The effects of turbulence on nanoparticle growth in turbulent reacting jets. *Phys. Fluids*, 22(103303), 2010.

[25] S. E. Miller and S. C. Garrick. Nanoparticle coagulation in a planar jet. *Aerosol Sci. and Technol.*, 38:79–89, 2004.

[26] G. Wang and S. C. Garrick. Modeling and simulation of titania formation and growth in temporal mixing layers. *J. Aerosol Sci.*, 37:431–451, 2006.

[27] J. Pyykonen and J. Jokiniemi. Computational fluid dynamics based sectional aerosol modelling schemes. *J. Aerosol Sci.*, 31:531, 2000.

[28] M. Mehta, Y. Sung, V. Raman, and R. O. Fox. Multiscale modeling of TiO2 nanoparticle production in flame reactors: effect of chemical mechanism. *Industrial & Engineering Chemistry Research*, 49:10663–10673, 2010.

[29] C. S. McEnally, A. M. Schaffer, M. B. Long, L. D. Pfefferle, M. D. Smooke, M. B. Colket, , and R. J. Hall. Computational and experimental study of soot formation in a coflow, laminar ethylene diffusion flame. *Symposium (International) on Combustion*, 27:1497–1505, 1998.

[30] G. Wang and S. C. Garrick. Modeling and simulation of titania synthesis in two-dimensional methane-air flames. *Journal of Nano Research*, 7:621–632, 2005.

[31] R. Bahadur and R. B. McClurg. Nucleation rates for the condensation of monovalent metals. *J. Chem. Phys.*, 121(24), 2004.

[32] T. A. Hamed, J. H. Davidson, and M. Stolzenburg. Hydrolysis of evaporated zn in a hot wall flow reactor. *Journal of Solar Energy Engineering*, 130(4), 2008.

[33] H. Reiss, W. K. Kegel, and J. L. Katz. Role of the model dependent translational volume scale in the classical theory of nucleation. *J. Phys. Chem. A.*, 102:8548, 1998.

[34] I. Alxneit. Assessing the feasibility of separating a stoichiometric mixture of zinc vapor and oxygen by a fast quench–Model calculations. *Solar Energy*, 82:959–964, 2008.

[35] J. Liu and S. C. Garrick. Comment on "Evaluation of surface tension and tolman length as a function of droplet radius from experimental nucleation rate and supersaturation ratio: Metal vapor homogeneous nucleation". *J. Chem. Phys.*, 132(1), 2010.

[36] M. Frenklach. Reaction mechanism of soot in flames. *Phys. Chem. Chem. Phys*, 4:2028, 2002.

[37] E. Bodenschatz, S. P. Malinowski, R. A. Shaw, and F. Stratmann. Can we understand clouds without turbulence? *Science*, 327:970, 2010.

[38] J. A. Paquette, F. T. Ferguson, and J. A. Nuth III. A model of silicate grain nucleation and growth in circumstellar outflows. *Astro. J.*, 62:732, 2011.

[39] A. Weidenkaff, A. W. Reller, A. Wokaun, and A. Steinfeld. Thermogravimetric analysis of the zno/zn water splitting cycle. *Thermochimica Acta 2000*, 359:69, 2000.

[40] A. Steinfeld. Solar thermochemical production of hydrogen - a review. *Solar Energy*, 78:603, 2005.

[41] S. E Pratsinis. Flame aerosol synthesis of ceramic powders. *Prog. Energy Combust. Sci.*, 24:197, 1998.

[42] E. G. Moody and L. R. Collins. Effect of mixing on the nucleation and growth of Titania articles. *Aerosol Sci. and Technol.*, 37:403–424, 2003.

[43] B. Hale. Application of a scaled homogeneous nucleation-rate formalism to experimental data at T < Tc. *Phys. Rev. A*, 33(6):4156, 1986.

[44] S. L. Girshick and C. P. Chiu. Kinetic nucleation theory: a new expression for the rate of homogeneous nucleation from an ideal supersaturated vapor. *J. Chem. Phys.*, 93(2):1273–1277, 1990.

[45] R. S. R Sidin, R. Hagmeijer, and U. Sachs. Evaluation of master equations for the droplet size distribution in condensing flow. *Phys. Fluids*, 21(7):073303, 2009.

[46] E. Chacon, F. Flores, and G. Navascues. A theory for liquid metal surface tension. *Journal of Physics F - Metal Physics*, 14(7):1587–1601, 1984.

[47] N. P. Rao and P. H. McMurry. Effect of the Tolman surface tension correction on nucleation in chemically reacting systems. *Aerosol Science and Technology*, 13:183–195, 1990.

[48] A. Laaksonen and R. McGraw. Thermodynamics, gas-liquid nucleation, and size-dependent surface tension. *Europhysics Letters*, 35(5):367, 1996.

[49] D. Mukherjee, A. Prakash, and M. Zachariah. Implementation of a discrete nodal model to probe the effect of size-dependent surface tension on nanoparticle formation and growth. *J. Aerosol Sci.*, 37:1388, 2006.

[50] Z. H. Li and D. G. Truhlar. Cluster and nanoparticle condensation and evaporation reactions. thermal rate constants and equilibrium constants of $al_m + al_{n-m} \rightarrow al_n$ with $n = 2 - 60$ and $m = 1 - 8$. *J. Phys. Chem. C*, 112:11109, 2008.

[51] R. A. LaViolette, R. A. Berry, and R. McGraw. Homogeneous nucleation of metals in a plasma-quench reactor. *Plasma Chem. and Plasma Proc.*, 16:249, 1996.

[52] S. Hartmann, D. Niedermeier, J. Voightländer, T. Clauss, R. A. Shaw, H. Wex, A. Kiselev, and F. Stratmann. Homogeneous and heterogeneous ice nucleation at LACIS: operating principle and theoretical studies. *Atmos. Chem. Phys.*, 11:1753, 2011.

[53] G. Y. Di Veroli and S. Rigopoulos. Modeling of aerosol formation in a turbulent jet with the transported population balance equation-probability density function approach. *Phys. Fluids*, 23:043305, 2011.

[54] J. Frenkel. *Kinetic theory of liquids*. Oxford University Press, 1946.

[55] R. B. Bird, W. E. Stewart, and E. N. Lightfoot. *Transport phenomena*. Wiley, 2nd edition, 2002.

[56] P. Grieveson and E. T. Turkdogan. Determination of interdiffusivities of argon and metal vapor mixtures at elevated temperatures. *J. Phys. Chem.*, 68(6):1547, 1964.

[57] K. M. Aref'ev, B. F. Remarchuk, and M. A. Guseva. Diffusion of metal vapors in gases and the transport properties of vapors. *J. Eng. Phys. Thermophys.*, 42(6):621, 1982.

[58] R. W. MacCormack. The effect of viscosity in hypervelocity impact catering. AIAA Paper 69–354, AIAA, 1969.

[59] C. A. Kennedy and M. H. Carpenter. Several new numerical methods for compressible shear-layer simulations. *Applied Numerical Mathematics*, 14:397, 1994.

[60] M. Wilck, K. Hämeri, F. Stratmann, and M. Kulmala. Determination of homogeneous nucleation rates from laminar-flow diffusion chamber data. *J. Aerosol. Sci.*, 8:889, 1998.

[61] D. M. Martinez, F. T. Ferguson, R. H. Heist, and J. A. Nuth III. Experimental studies of the vapor phase nucleation of refractory compounds. vi. the condensation of sodium. *J. Chem. Phys.*, 123(054323), 2005.

[62] F. Aristizabal, J. M. Richard, and D. Berk. Modeling of the production of ultra fine aluminium particles in rapid quenching turbulent flow. *J. Aerosol Sci.*, 37:162, 2006.

[63] N. Settumba and S. C. Garrick. Modeling and simulation of nano-aluminum synthesis in a plasma reactor. *In Kuo and Rivera [65]*, page 643, 2007.

[64] S. Panda and S. E. Pratsinis. Modeling the synthesis of aluminum [articles by evaporation-condensation in an aerosol flow reactor. *Nanostructured Materials*, 5(7):755, 1995.

[65] K. K. Kuo and J. D. editors Rivera, editors. *Advancements in energetic materials and chemical propulsion*. Begell House Inc., New York, USA, 2007.

[66] D. A. Kaplowitz, R. J. Jouet, and M. R. Zachariah. Aerosol synthesis and reactive behavior of faceted aluminum nanocrystals. *Journal of Crystal Growth*, 312:3625–2630, 2010.

[67] F. Lesniewski and S. K. Friedlander. The effect of turbulence on rates of particle formation by homogeneous nucleation. *Aerosol Sci. and Technol.*, 23(2):174, 1995.

[68] T. Lesniewski and S. K. Friedlander. Particle nucleation and growth in a free turbulent jet. *Proc. R. Soc. Lond. A*, 454:2477, 1998.

[69] R. A. Shaw. Particle-turbulence interaction in atmospheric clouds. *Annu. Rev. Fluid Mech.*, 35:183, 2003.

[70] J. H. ter Horst, D. Bedeaux, and S. Kjelstrup. The role of temperature in nucleation processes. *J. Chem. Phys.*, 134:054703, 2011.

[71] J. H. Seinfeld and S. N. Pandis. *Atmospheric chemistry and physics: from air pollution to climate change*. Wiley, 2nd edition, 2006.

[72] E. K. Longmire, J. K. Eaton, and C. J. Elkins. Control of jet structure by crown-shaped nozzle. *AIAA Journal*, 30(2), 1992.

[73] W. Lenggoro, T. Hata, F. Iskandar, M. M. Lunden, and K. Okuyama. An experimental and modeling investigation of particle production by spray pyrolysis using a laminar flow aerosol reactor. *J. Mater. Res.*, 15:733, 2000.

[74] M. M. Koochesfahani and P. E. Dimotakis. Mixing and chemical reactions in a turbulent liquid mixing layer. *J. Fluid Mech.*, 170:83, 1986.

[75] P. E. Dimotakis. Turbulent mixing. *Annu. Rev. Fluid Mech.*, 37:329, 2005.

[76] C. Housiadas, E. Papanicolaou, and Y. Drossinos. Combined heat and mass transfer in laminar flow diffusion nucleation chambers. *J. Aerosol Sci.*, 33:797, 2002.

[77] P. A. McMurtry, J. J. Riley, and R. W. Metcalfe. Effects of heat release on the large-scale structure in turbulent mixing layers. *J. Fluid Mech.*, 199:297, 1989.

[78] P. Givi, C. K. Madnia, C. J. Steinberger, M. H. Carpenter, and J. P. Drummond. Effects of compressibility and heat release in a high speed reacting mixing layer. *Combust. Sci. Technol.*, 78:33, 1991.

[79] R. Kumar, Z. Li, A. van Duin, and D. Levin. Molecular dynamics studies to understand the mechanism of heat accommodation in homogeneous condensing flow of carbon dioxide. *J. Chem. Phys.*, 135:064503, 2011.

[80] J. C. Hermanson and P. E. Dimotakis. Effects of heat release in a turbulent, reacting shear layer. *J. Fluid Mech.*, 199:333, 1989.

[81] H. V. Nguyen, K. Okuyama, T. Mimura, Y. Kousaka, R. Flagan, and S. Seinfeld. Homogeneous and heterogeneous nucleation in a laminar flow aerosol generator. *J. Colloid Interf. Sci.*, 119:491, 1987.

[82] M. Wilck and F. Stratmann. A 2-D multicomponent model aerososl and its application to laminar flow reactors. *J. Aerosol Sci.*, 28:959, 1997.

[83] K. M. Tacina and W. J. A. Dahm. Effects of heat release on turbulent shear flows. Part 1. A general equivalence principle for non–buoyant flows and its application to turbulent jet flames. *J. Fluid Mech.*, 415:23–44, 2000.

[84] W. J. A. Dahm. Effects of heat release on turbulent shear flows. Part 2. Turbulent mixing layers and the equivalence principle. *J. Fluid Mech.*, 540:1–19, 2005.

[85] H. Laksmono, S. Tanimura, and B. E. Wyslouzil. Methanol nucleation in a supersonic nozzle. *J. Chem. Phys.*, 135:074305, 2011.

[86] K. Okuyama, Y. Kousaka, D. R. Warren, F. C. Flagan, and J. H. Seinfeld. Homogeneous nucleation by continuous mixing of high temperature vapor with room temperature gas. *Aerosol Sci. Technol.*, 6(1):15, 1987.

[87] K. Hämeri and M. Kulmala. Homogeneous nucleation in a laminar flow diffusion chamber: the effect of temperature and carrier gas on dibutyl phthalate vapor nucleation rate at high supersaturations. *J. Chem. Phys.*, 105:7696, 1996.

[88] V. B. Mikheev, N. S. Laulainen, S. E. Barlow, M. Knott, and I. J. Ford. The laminar flow tube reactor as a quantitative tool for nucleation studies: experimental results and theoretical analysis of homogeneous nucleation of dibutylphthalate. *J. Chem. Phys.*, 113:3704, 2000.

[89] J. Pyykonen, M. Miettinen, O. Sippula, A. Leskinen, T. Raunemaa, and J. Jokiniemi. Nucleation in a perforated tube diluter. *J. Aerosol Sci.*, 38:172, 2007.

[90] A. Guha. Transport and deposition of particles in turbulent and laminar flow. *Annu. Rev. Fluid Mech.*, 40:311–341, 2008.

[91] D. Livescu, F. A. Jaberi, and C. K. Madnia. The effects of heat release on the energy exchange in reacting turbulent shear flow. *J. Fluid Mech.*, 450:35–66, 2002.

[92] X. Luo, G. Lamanna, A. P. C. Holten, and M. E. H. van Dongen. Effects of homogeneous condensation in compressible flows: Ludwieg–tube experiments and simulations. *J. Fluid Mech.*, 572:339–366, 2007.

[93] W. W. Grabowski and L. Wang. Growth of cloud droplets in a turbulent environment. *Annu. Rev. Fluid Mech.*, 45:293–324, 2012.

[94] S. L. Girshick, P. Agarwal, and D. G. Truhlar. Homogeneous nucleation with magic numbers: aluminum. *J. Chem. Phys.*, 131(134305), 2009.

[95] A. Prakash, A. P. Bapat, and M. R. Zachariah. A simple numerical algorithm and software for solution of nucleation, surface growth, and coagulation problems. *Aerosol Sci. Technol.*, 37:892–898, 2003.

[96] L. Pasquini, M. Brighi, A. Montone, M. V. Antisari, B. Dam, V. Palmisano, and E. Bonetti. Magnesium nanoparticles for hydrogen storage: structure, kinetics and thermodynamics. *IOP Conf. Ser.: Mater. Sci. Eng.*, 38:012001, 2012.

[97] S. Lee, J. Lee, and Y. Kim. Nucleation and growth of zinc particles on an aluminum substrate in a zincate process. *Journal of Electronical Materials*, 36:1442–1447, 2007.

[98] D. M. Martínez, F. T. Ferguson, R. H. Heist, and J. A. Nuth. Application of scaled nucleation theory to metallic vapor condensation. *J. Chem. Phys.*, 115:310–316, 2001.

Appendix A

Time-scales for nanoparticle nucleation

In homogeneous nucleation theory, the nucleation rate expression (given by Eq. 2.15) represents the steady formation rate of the critical nuclei at a given physical environment. Since particle formation process needs finite time for clusters to reach the critical size, meanwhile the local physical conditions might change rapidly, which could cause failure of homogeneous nucleation expression. the time-scale for nanoparticle nucleation is important for the implement of steady state nucleation rate expression in the computational fluid dynamics. However, to the author's knowledge currently nucleation theory with steady nucleation rate expression is the only efficient and economic approach for numerical simulations of a practical flow system. In order to validate the application of the steady nucleation expression in the context of fluid fluctuations, it is necessary to analyze the transient nanoparticle formation time scale [94].

We propose to examine the validity of using homogeneous nucleation theory in turbulent flow simulations via comparison with a polymerization based nucleation approach. The polymerization approach essentially simulate the cluster growth process by adding and losing one monomer by the cluster at a time via condensing and evaporation, which is currently widely accepted as the aerosol particle formation mechanism. The change

of particle concentration for the k-mer per unit time is given by

$$\frac{dN_k}{dt} = N_1 \frac{1}{1+\delta_{2k}} k_f(1,k-1)N_{k-1} - k_b(k)N_k - \left(N_1 \frac{1}{1+\delta_{2k}} k_f(1,k)N_k - k_b(k+1)N_{k+1} \right), \tag{A.1}$$

where N_1 and N_k are the number concentration of the monomer and k-mer, only non-zero value for δ_{2k} is $\delta_{2k} = 1$ when $k = 2$, k_f and k_b are the forward and backward rate which represent the monomer adsorption and de-adsorption from a cluster respectively [95]. Cluster growth is calculated via the collision frequency, assuming each collision between the monomer and cluster will stick is given by

$$k_f(1,k) = \left(\frac{3}{4\pi}\right)^{1/6} \left(\frac{6k_BT}{\rho_m}\right)^{1/2} \left(\frac{1}{v_m} + \frac{1}{v_k}\right)^{1/2} \left(v_m^{1/3} + v_k^{1/3}\right)^2. \tag{A.2}$$

The loss of monomer (or evaporation rate) is reached via analyzing the Gibbs free energy changes, and derived from the equilibrium constant, in the classical theory it is given by

$$k_b(k) = k_f(1,k-1) n_s \exp\left(\Theta_k k^{2/3} - \Theta_{k-1}(k-1)^{2/3}\right), \tag{A.3}$$

where n_s is the equilibrium monomer concentration based on the saturation vapor pressure at temperature T, and Θ_k is the non-dimensional surface tension of a k-mer, which is given by

$$\Theta_k = \frac{s_m \sigma_k}{k_B T} \tag{A.4}$$

where σ_k and s_m are the surface tension and total surface area of the k-mer, respectively [49].

The assumption made in the polymerization approach are (1) cluster grows stepwise by adsorption and desorption of one monomer per time; (2) the Gibbs free energy change takes into account of the surface energy change of the cluster only; (3) each collision between monomer and cluster is assumed efficient for absorption, and the collisions between clusters are neglected. The polymerization theory gives an applicable method to monitor the temporal evolution of the k-mer . At certain temperature, given an initial number concentration of the monomer, and a suitable surface tension model of certain material, we can simulate the rate of growth for the k-mer vs the actual time needed. In this way we can determine the smallest time scale needed for the homogeneous nucleation rate expression to be a solid assumption.

Zinc is chosen as the primary candidate because of its wide and important applications such as producing hydrogen using solar energy [3, 35]. Additionally, experiments in the Solar Thermal Laboratory (of Mechanical Engineering) can provide physical data. The simulation uses the discrete method to represent the clusters by the number of molecules they include. A total number of $N_B = 100$ bins are used, and in the kth bin the corresponding clusters have k molecules inside, where $k = 1, 2...N_B$. An initial saturation ratio S and temperature T are set as input quantities, and the initial monomer concentration N_1 is calculated via the saturation ratio S and the saturation pressure $p_s(T)$, which is a function of temperature only. The initial monomer concentration is given by $n_1 = SP_s/k_BT$. A time step of $dt = 10^{-9}s$ is used to propagate the temporal evolution of the clusters in each bin and a total $n = 10^6$ iterations are performed. In calculating the forward and backward rates, size-dependent surface tension model form the previous section is employed.

Additionally, only monomer-cluster collisions/growth are represented [16]. The preliminary results for the cluster temporal evolution under different temperatures and saturation ratios are shown in Fig. A.1. The solid lines represent the evolution of the clusters from the first bin to the $k = 20$ bin. The red lines represent the temporal growth of the cluster at critical size under local physical conditions. The combinations are sampled based on high zinc nanoparticle nucleation rate zones in practical flows, which is identified via simulations conducted in the following sections. All the four samples covers the combinations of high and low temperature and saturation ratio respectively. The plots show that the clusters of critical size are formed quicker when the temperature is higher or the saturation ratio is higher, vise versa. When the number concentration of the k-mers does not change in more than one order of magnitude for two orders of magnitudes in time and so on, it is considered the clusteris steady. In the region where we are most interested in (where the nucleation rate is the highest), the approximate evolution time scale for clusters to reach the critical size and keeps steady nucleation rate is on the order of $10^{-4}s$. It suggests that the in turbulent flow simulations the turbulent fluctuation time-scale cannot exceed the above time scale to apply for the steady nucleation rate expression. Figure A.2 shows the temporal evolution of nucleation current for the critical sized cluster for the above cases. For Case (a) the nucleation rate becomes stable at around $t = 10^{-4}s$ at low temperature and high

saturation ratio. For higher temperature and low saturation ratio (Case (d)), nucleation rate becomes stable at around $t = 10^{-6}s$. For cases between such two extreme ends, the nucleation rate becomes stable between $t = 10^{-7}s$ and $t = 10^{-5}s$. The above results again proves that for most grids within the flow field, the time scale of nucleation to reach steady state nucleation rate is lower than $t = 10^{-4}s$.

Besides the advantages of validating the nucleation theory in a simple way and monitoring the cluster temporal evolution. Limitations of the above polymerization approach are also significant and mainly result from the assumptions made above. A simulation of all possible combinations of collisions are now possible and in progress. Recent progress of nanoparticle nucleation has found there are certain "magic numbers" for specific materials which might lead to significant variations from about method [94]. If one can get a more accurate Gibbs free energy model from DSMC or statistical mechanics for certain material, it could further improve the accuracy of this method. However the major limitation is the cost of large scale simulations using this method, in practical flows all combinations of thermal and physical properties must be considered and hundreds of dynamic equations need to be solved.

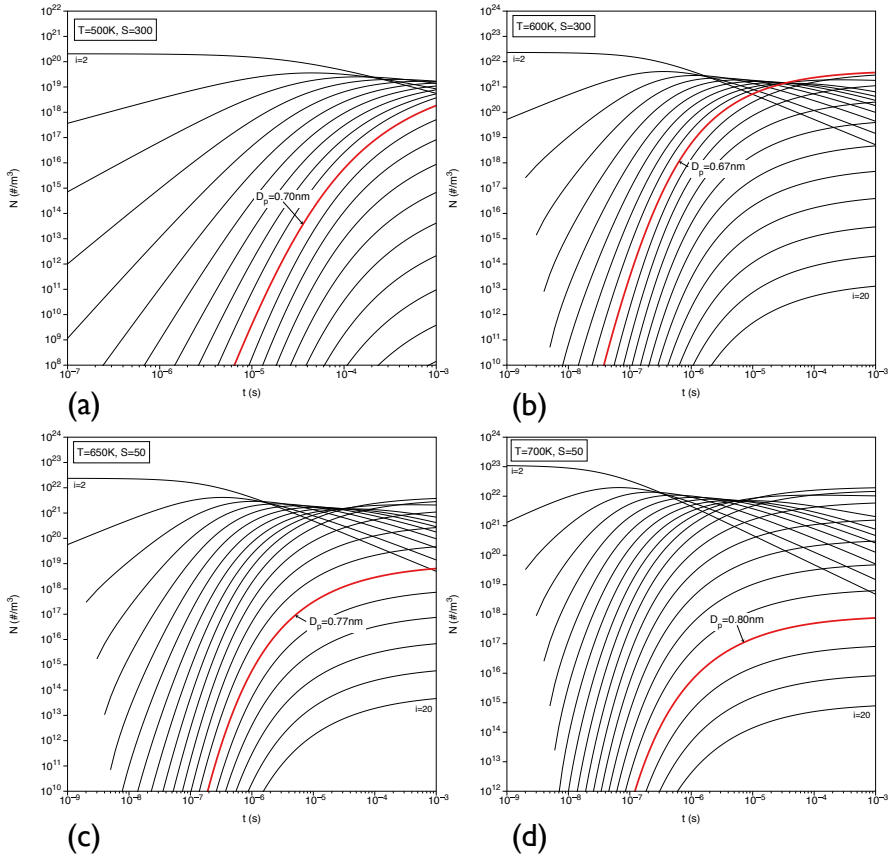

Figure A.1: Temporal evolution of cluster number densities. Red line represents the critical sized cluster. (a) T=500K, S=300; (b) T=600K, S=300; (c) T=600K, S=50; (d) T=700K, S=50.

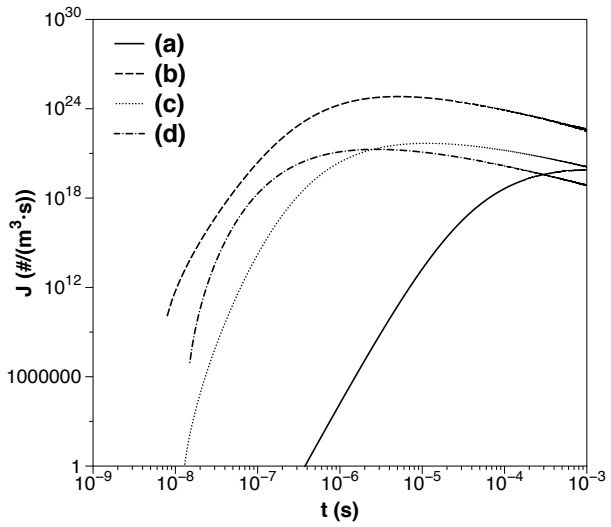

Figure A.2: Temporal evolution of nucleation current for the critical sized cluster. (a) T=500K, S=300; (b) T=600K, S=300; (c) T=600K, S=50; (d) T=700K, S=50.

Appendix B

Effects of flow cooling on metal nucleation with size-dependent surface tension

Numerical simulations of zinc, lithium, and magnesium nucleation are performed to study the effects of size-dependent surface tension on metal homogeneous nucleation. We adopt a size-dependent surface tension nucleation theory (SDNT in three-dimensional laminar round jets, and assess the model performance against classical nucleation theory (CNT. The jet flows consist of high-temperature metal vapor diluted in argon issuing into a cooler particle-free argon stream. We focus only on homogeneous nucleation. While condensation, coagulation etc. are important in the particle formation processes, we are elucidating the modeled nucleation dynamics. The results show that nucleation rates and critical particle sizes predicted by SDNT vary significantly from CNT. More importantly, SDNT predicts that nucleation rate decreases as the flows mix downstream, where CNT shows it will continuously increase. The inclusion of the size-dependent surface tension results in improved model performance, and suggests a dynamics not observed in CNT.

B.1 Introduction

Metal nanoparticles appear in many scientific and industrial processes, because of high surface-to-volume ratio. Especially, they are promising materials for renewable energy generation and storage [5, 39, 40, 96]. In various techniques of metal nanoparticle synthesis, gas-to-particle conversion is favored for its broad industrial applications, in which homogeneous nucleation plays an essential role [42, 25, 97]. The classical nucleation theory (CNT for homogeneous nucleation has been developed for decades [16, 71]. However, its applicability is limited in describing metal nucleation due to unsatisfied accuracy [2, 1, 3]. Scaled nucleation theory and molecular dynamics simulation have been used to improve the accuracy of CNT, however their applications are also limited due to the need of priori critical data, or restricted small length scale [98, 20]. Models which are implementable in engineering calculations with improved physical fidelity are needed.

Recent studies have shown that many material properties vary significantly with particle sizes especially at nano-scale [15, 13, 49]. The surface energy for instance, is not necessarily based on the bulk value of surface tension value [15, 46, 47, 48]. Since surface energy plays an essential role in nucleation processes, a promising approach to improve the accuracy of homogeneous nucleation model is to include the effect of size-dependent surface tension [16, 71, 3, 35]. Especially, based on metal nucleation experiments, Onischuk *et al.* (2006) derived an expression for metal homogeneous nucleation rate with surface tension as a function of particle sizes.

In this work we compare the predictions of CNT and the SDNT for the homogeneous nucleation of metal nanoparticles. Specifically we simulate the nucleation of lithium, zinc, and magnesium nanoparticles in round jets. We analyze the thermal and chemical fields along with the saturation ratio, critical diameter and nucleation rate. We also consider the evolution as the flow develops as well as the dynamics in temperature – mass-fraction space and how such dynamics inform the particle formation rate.

B.2 Formulation

B.2.1 Fluid and scalar transport

The fluid dynamics are governed by explicitly solving the Navier-Stokes equations. The variables are fluid velocity u_i, pressure p, density ρ and enthalpy h.

$$\frac{\partial \rho}{\partial t} + \frac{\partial \rho u_j}{\partial x_j} = 0, \tag{B.1}$$

$$\frac{\partial \rho u_i}{\partial t} + \frac{\partial \rho u_i u_j}{\partial x_j} = -\frac{\partial p}{\partial x_i} + \frac{\partial \tau_{ij}}{\partial x_j}, \tag{B.2}$$

$$\frac{\partial \rho h}{\partial t} + \frac{\partial \rho h u_j}{\partial x_j} = \frac{\partial}{\partial x_j}\left(\frac{k}{C_p}\frac{\partial h}{\partial x_j}\right), \tag{B.3}$$

where τ_{ij} is the viscous stress tensor, k represents the thermal conductivity, and C_p is the constant pressure specific heat. The equations are closed by using the ideal gas relation, $p = \rho RT$ where R is the gas constant. The enthalpy, h, is related to the temperature T via $dh = C_p dT$.

The jet flows consist of a condensing metal vapor diluted in argon. The mass-fraction, Y_i, of the condensing species is governed by

$$\frac{\partial \rho Y_i}{\partial t} + \frac{\partial \rho u_j Y_i}{\partial x_j} = \frac{\partial}{\partial x_j}\left(\rho D_i \frac{\partial Y_i}{\partial x_j}\right) + \dot{\omega}_i, \tag{B.4}$$

where D_i is the diffusion coefficient. The term $\dot{\omega}_i$ represents vapor-to-particle mass conversion, which is given by

$$\dot{\omega}_i = \frac{\pi}{6}\rho_i {d_p}^3 J, \tag{B.5}$$

where ρ_i is density of the condensing species, d_p is the critical particle diameter, and J is the nucleation rate, i.e. the formation rate of nanoparticle from gas phase.

B.2.2 Nucleation modeling

We evaluate the homogeneous nucleation predicted by SDNT and SDNT. The expression for nucleation rate, J, in CNT is given by

$$J_c = \frac{(\rho Y_i)^2}{\rho_i m_i}\sqrt{\frac{2\sigma}{\pi m_i}}\exp\left(-\frac{\pi\sigma {d_p}^2}{3k_B T}\right), \tag{B.6}$$

where m_i is mass per molecule for the condensing species, k_B is the Boltzmann constant, and σ is the surface tension.

Recent studies show that surface tension exhibits significant variation with the curvature of particle sizes [15, 47, 3, 35, 22]. Onischuk *et al.* (2006) derived a homogeneous nucleation rate expression that accounts for the effect of size-dependent surface tension, which is given by

$$J_s = \frac{\rho Y_i}{2m_i \pi R_s} \sqrt{\frac{3 \ln S}{\rho \kappa}} \sqrt{\frac{R_s}{R_e}} \exp\left(-\frac{16\pi m_i^2}{3\rho^2 (\ln S)^2} \left(\frac{\sigma}{k_B T} \right)^3 \right), \tag{B.7}$$

where R_e is the radius of the equimolar surface when size-dependent surface tension is not taken into consideration, R_s is the radius of critical nuclei with SDNT ($R_s = d_p/2$), and κ is isothermal compressibility of the condensing material. The saturation ratio, S, for metal vapor is given by $S = p_i/p_s$, where p_i is the partial pressure of metal vapor and p_s is the saturated pressure. Saturated pressure as a function of temperature for several metal materials is given by $p_s = 133.32 \times 10^{C-D/T}$ in pascal, where C and D are parameters obtained by fitting data from reference books ([3]. Onischuk *et al.* (2006) also derived the size-dependent surface tension expression by

$$\sigma(d_p, T) = \sigma_T(T) \exp\left[-4 \frac{\delta(d_p)}{d_p} \left(1 - \beta \frac{2\delta(d_p)}{d_p} \right) \right], \tag{B.8}$$

where $\sigma_T(T) = C_1 (C_2 - T)$ is the temperature dependent part of surface tension. The enclosed function β is given by

$$\beta = 1 - \frac{1}{2} \left(\delta_o \frac{\delta(3/4 d_p)}{\delta^2(d_p)} \right), \tag{B.9}$$

where

$$\delta(d_p) = \frac{A}{d_p} + \delta_o. \tag{B.10}$$

In the above expression, both δ_o and A are material-related constants. The diameter of the critical nuclei in homogeneous nucleation process, d_p, is given by the Kelvin relation

$$d_p = \frac{4\sigma m_i}{k_B T \rho_i \ln(S)}. \tag{B.11}$$

The values of these parameters mentioned above are listed in table B.1 and a thorough description of the approach is given by Onischuk *et al.* (2006) [3].

B.3 Results

B.3.1 Simulation configuration and physical assumptions

The flows consist of a three-dimensional round jet of nozzle diameter D, with U_o velocity issuing into a co-flowing stream of velocity U_∞. The flows are laminar and the velocity ratio is $U_\infty/U_o = 0.4$. The Reynolds number, Re_D, based on the fluid density ρ, jet diameter D, jet velocity U_o, and viscosity μ is given by $Re = \rho U_o D/\mu$. The hot metal vapor stream at temperature T_o diluted in argon issues into a cooler particle-free argon stream of temperature T_∞, where $T_\infty/T_o = 0.45$. The mass fraction of the metal vapor in the jet is Y_o. A schematic of the flow configuration is shown in Fig. B.1. The thermal, chemical, and transport properties of simulations are listed in table B.2.

Three metal materials are considered – lithium (Li), magnesium (Mg), and zinc (Zn). All physical properties such as viscosity and heat conductivity of fluid mixture are calculated based on local chemical composition, Y_i. Variation of these properties as a function of temperature T is adopted from published empirical curves to ensure higher accuracy [1, 2, 3]. The particle density is taken as condensed phase value and the particle volume v_i is calculated by $v_i = \frac{1}{6}\pi d_p^3$. A typical volume fraction (ratio of the total volume of particles to the volume of fluid mixture) is less than 10^{-7} so that momentum transfer between fluid and particles is negligible. The governing equations for flow, thermal and chemical transport are solved explicitly using a fourth order accurate hybrid MacCormack-based, predictor-corrector scheme [58, 59]. Computations are mainly performed on a domain of $14D \times 8D \times 8D$ in x, y and z directions respectively. The resolution for all simulations is $320 \times 240 \times 240$. The results exhibited grid independence at this resolution as the flows are laminar. Each simulation performed requires roughly 200 CPU-hours.

B.3.2 Nucleation rate and particle size

Saturation ratios act as the bridge between fluid dynamics and particle nucleation. The saturation ratio contours at plane $z = 0$ are shown in Fig. B.2. Fluid mixing processes within the flows are essentially both diluting and cooling of the condensing vapor, where the formal decreases the saturation ratio and the later increases it. Homogeneous nucleation is highly sensitive to local temperature and vapor concentration, which are

provided explicitly by computational fluid dynamics. The results show that metal vapor becomes supersaturated within the shear layer formed between the jet and co-flow. As the jet flow leaves the nozzle, initially, the metal molecules within the jet collide but do not "stick" together as the surface energy of nuclei is not sufficient to bind the kinetic energy of the participating molecules. As the flow travels downstream, the molecules become less energetic caused by cooling effect via thermal diffusion. Super-saturated region spreads in width spatially and saturation ratio increases stream-wise. Stable clusters can be formed within supersaturated metal vapor. Figure B.2(a) shows the highest saturation ratio for lithium is $S = 750$, which is less than zinc ($S = 2000$, Fig. B.2(b)) but greater than magnesium ($S = 120$, Fig. B.2(c)). The results reflect the saturation ratios required to reach steady nucleation rate within laminar flows vary for different metal materials. The interactive effect of nucleation with fluid dynamics has been described by Liu and Garrick [22]. Though nucleation rates are not only related to saturation ratios, but also largely affected by the critical sizes of nuclei, we have coupled fluid dynamics and particle nucleation via computational fluid dynamics to ensure higher simulation fidelity.

Figure B.3 shows the comparison of SDNT with CNT for lithium nucleation. Simulation data are presented for lithium particle's nucleation rate J_s vs. critical particle diameter d_p. Results show that nucleation rates are generally higher and the estimated critical diameters are smaller as predicted by CNT. For example, in CNT the typical value of nucleation rate J_s, where the majority of scalar points are clustered, is $J_s = 10^{26}$ and the corresponded critical particle diameter is $d_p = 0.55$nm. As a result of SDNT, the particle diameter mainly distributed in the region $d_p = 0.9$ to $d_p = 1.3$nm, and the typical nucleation rates distribute from $J_s = 10^8$ to $J_s = 10^{18}$. Results indicate that CNT has over-predicted nucleation rate and under-estimated critical particle diameter for lithium nucleation. Similar variations between CNT and SDNT have been reported for zinc nucleation [22]. The variations are significant in the smaller particle size region ($d_p \leq 1.0$nm), which is natural due to the variations of surface tension for these materials at small sizes.

Scatter plots of metal nucleation rate J_s vs. critical diameter d_p as a function of temperature T are shown in Fig. B.4. Let us consider how the fluid emanating from the jet traverses this space. Position ① corresponds to the region where the temperature

of condensing vapor is still high, i.e. the region near inlet and inside of the jet. Then the flow experiences both diluting and cooling as it travels downstream to position ② and ③, which correspond to the inside (higher temperature) and outside (lower temperature) of the shear layer, respectively. Position ④ corresponds to the region with lower temperature, which locates even further from the shear layer into the co-flow. The effects of fluid cooling can then be observed in the nucleation rate – critical particle diameter space. Figure B.4(a) shows that size of lithium particles varies from $d_p = 0.95$ to 2.1nm. Between position ① and ②, as fluid is cooled down, nucleation rate increases as the critical diameter decreases. However, as the flow further cools down from ② to ③, instead of further increase of nucleation rate with decreasing critical diameter, the nucleation rate actually decreases. Between position ③ and ④ where temperature keeps decreasing, nucleation rate again decreases as the critical particle size increases. Figure B.4(b) shows that zinc nucleation with similar variations. Zinc nanoparticles are formed in the range $0.61 < d_p < 1.4$nm. As the flow is cooled from position ① to ②, zinc nucleation rate increases with decreasing particle size. Between ② and ③ as the flow further cools down, nucleation rate decreases as smaller zinc particles are formed. From position ③ to ④ as temperature decreases, nucleation rate again decreases as the critical particle size increases. Magnesium nucleation is shown in Fig. B.4(c). The critical diameters range from $d_p = 0.85$ to 1.65nm. Unlike zinc and lithium, magnesium nucleation rate increases as the critical diameter decreases when the flow is cooled down from position ① to ②, and the nucleation rate decreases as the critical diameter increases when the flow is cooled down further from position ② to ③. The aforementioned variation, as the nucleation rate decreases with decreasing particle critical diameter when the flow is cooled, is not found.

We provide a view of the spatially-evolving nucleation dynamics by tracing a parcel of fluid emanating from the center of the nozzle ($x/D = 0$ and $r/D = 0$, where $r = \sqrt{y^2 + z^2}$). One such trajectory – for the lithium flow – is shown in Fig. B.5. Along this trajectory, we show the mass-fraction, temperature, nucleation rate, and critical diameter. Figure B.5(a) shows the evolution of the mass-fraction and the temperature. Temperature is normalized by $T^\star = (T - T_\infty)/(T_o - T_\infty)$, and mass fraction is normalized by $Y^\star = Y/Y_o$, both decrease due to dilution and cooling. (The mass-fraction, $Y^\star$, decreases faster than the temperature as the Lewis number is $Le = 0.74$, reflecting the

fact that mass-diffusion is greater than heat conduction.) The evolution of the nucleation rate and the critical diameter are shown in Fig. B.5(b). Results show that along the centerline, no nucleation occurs before or upstream of $x/D = 9$. The nucleation rate using both SDNT and CNT then increase rapidly. In SDNT, the rate of increase of J has begins to slow. This trend continues and by $x/D = 14$ the nucleation rate has stopped increasing in SDNT. The nucleation rate then decreases as the flow travels downstream. However, in CNT the nucleation rate continues to increase even though the rate of increase slows down as the flow travels downstream. The results show that in both approaches, the critical diameters are the same once nucleation begins, $d_p = 1.9$nm. As the jet travels downstream, the critical diameter decreases and the particle size predicted by CNT decreases faster than that predicted by SDNT. By $x/D = 24$, CNT predicts a critical diameter of $d_p = 0.62$ while SDNT predicts $d_p = 1.0$nm. These results suggest that if cooling and dilution were to continue – longer domain or more efficient/rapid mixing – the particle nucleation rate would actually decrease while a significant amount of lithium vapor remains in the flow [22]. This is not what CNT predicts.

B.4 Summary and conclusions

Simulations of lithium, zinc and magnesium nanoparticle nucleation in laminar jets are performed. The jet flows consist of metal vapor diluted in argon issuing into a cooler argon stream. As the flow travels downstream, the metal vapor becomes supersaturated and nanoparticles are formed as a result of homogeneous nucleation. The nanoparticle formation process is modeled using a size-dependent surface tension nucleation theory (SDNT, and compared against the classical nucleation theory (CNT. The intercorrelation of nucleation with fluid dynamics is analyzed by the saturation ratio distribution within the flows. Nucleation occurs in the shear layers where temperature and the metal vapor mass-fraction decreases via molecular transport between the jet and co-flow. The cooling and diluting effects of fluid dynamics reflect the increase and decrease of saturation ratio respectively. The metal nanoparticles are formed at small sizes where the size dependence of surface tension is essential for predicting the nucleation rate. More importantly, the results also show if cooling and dilution were to continue with longer

domain or more efficient/rapid mixing, the particle nucleation rate would actually decrease rather than increase as CNT predicted. The dynamics predicted by SDNT are not observed in CNT.

The size-dependent surface tension nucleation theory is evaluated by comparing with CNT. Previous results show that SDNT promises to be more accurate in correlating the particle production rate with critical saturation ratios, etc. [3, 22]. SDNT also is committed to compatibility, computational efficiency while maintaining the ease with which it can be implemented in computational fluid dynamics.

Table B.1: Nucleation constants and parameters

Species	A (nm^2)	C	D/T	δ_o (nm)	$C_1 \times 10^{-3}$	C_2
Li	-0.389	8.00	8120	0.097	0.140	3300
Mg	-0.406	8.80	7674	0.350	0.254	3128
Zn	-0.45	8.35	6400	0.448	0.167	5430

Table B.2: Thermal, chemical, and transport properties

Species	Mass fraction	T_o (K)	T_∞ (K)	Re	Le
Li	0.02	1615	726	130	0.77
Mg	0.02	1400	630	167	1.52
Zn	0.02	1000	450	224	0.74

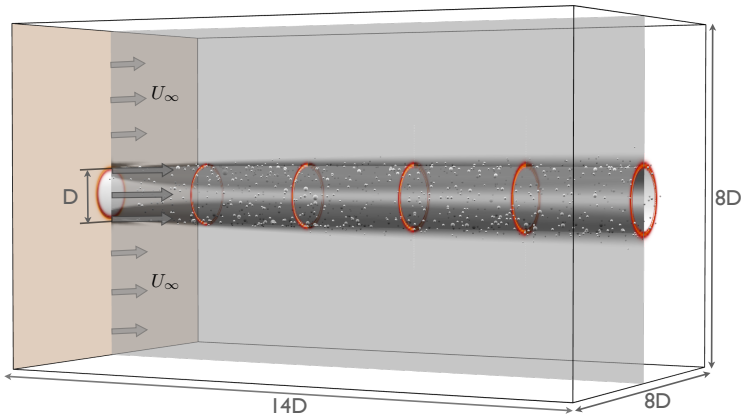

Figure B.1: Simulation configuration. It shows vorticity contour at plane $y = 0$, temperature contour at plane $x = 0$, and nucleation rate contour at five downstream locations. The silver sphere represent zinc nucleation, the sizes are scaled to the actual critical diameter of zinc nuclei and the number density is scaled to the zinc nucleation rate.

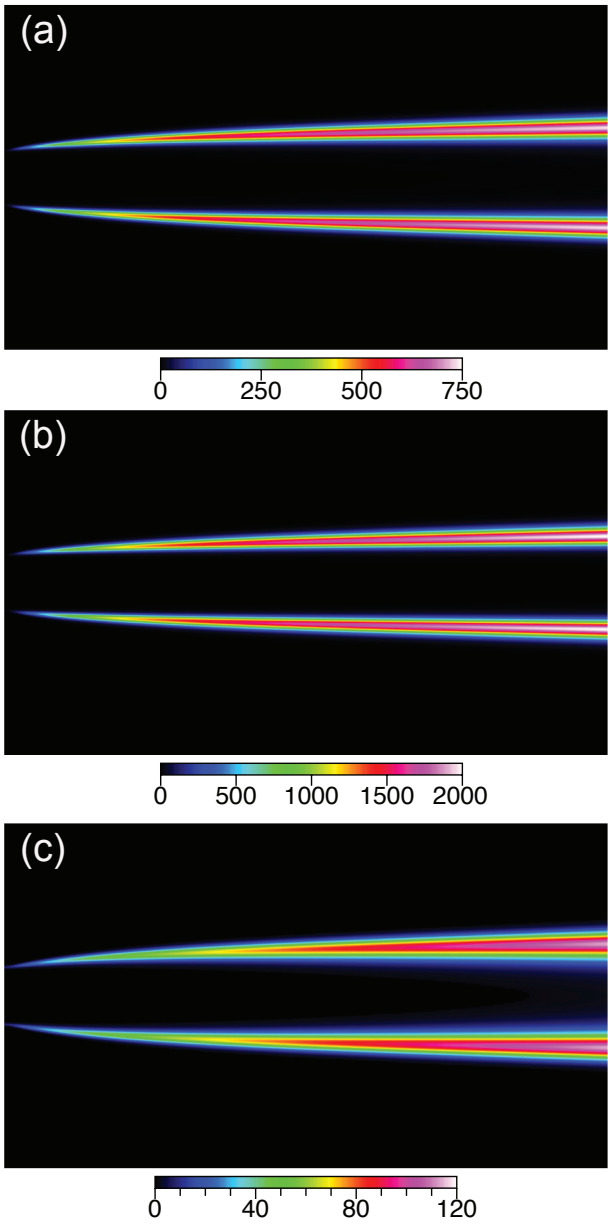

Figure B.2: Contours of the saturation ratio, S, along the plane $z = 0$: (a) lithium; (b) zinc; and (c) magnesium.

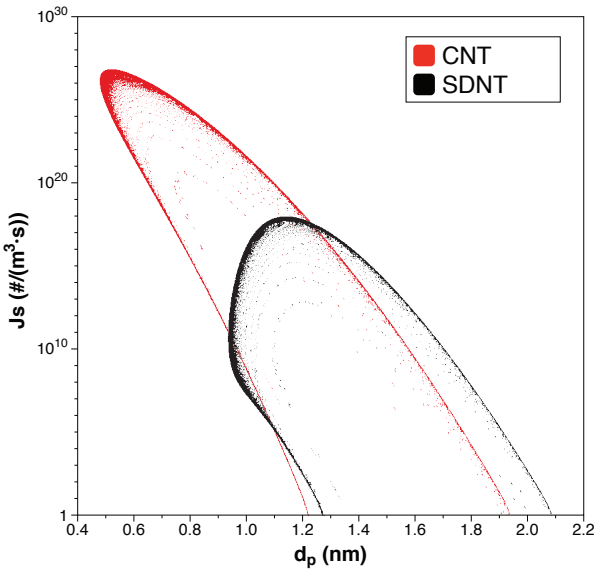

Figure B.3: Nucleation rate J_s vs critical diameter d_p, for lithium nucleation.

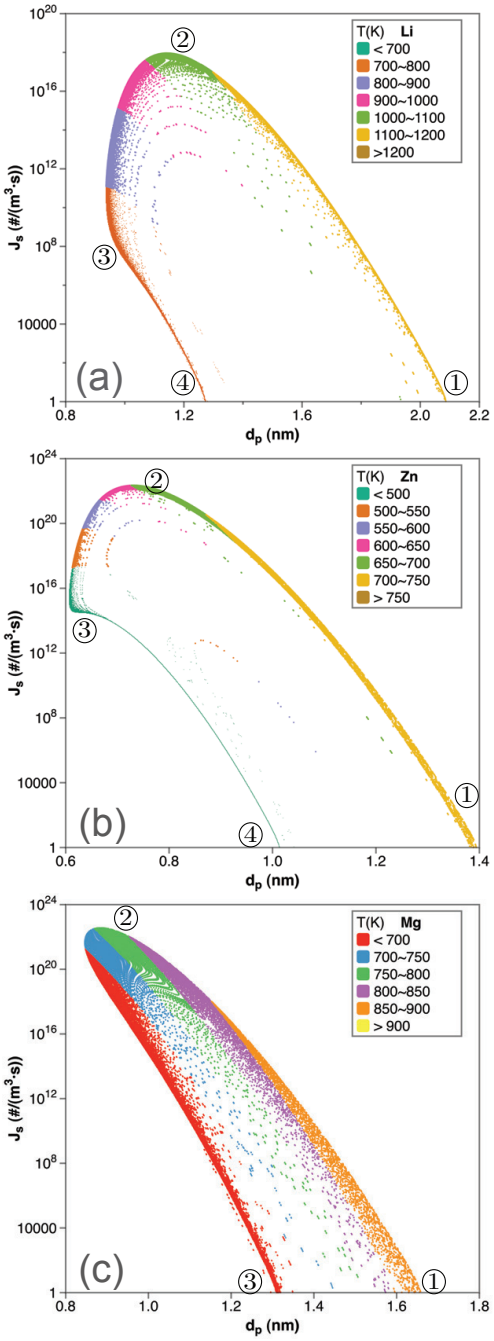

Figure B.4: Scatter plot of nucleation rate J_s vs critical diameter d_p, as a function of temperature T: (a) lithium; (b) zinc; and (c) magnesium.

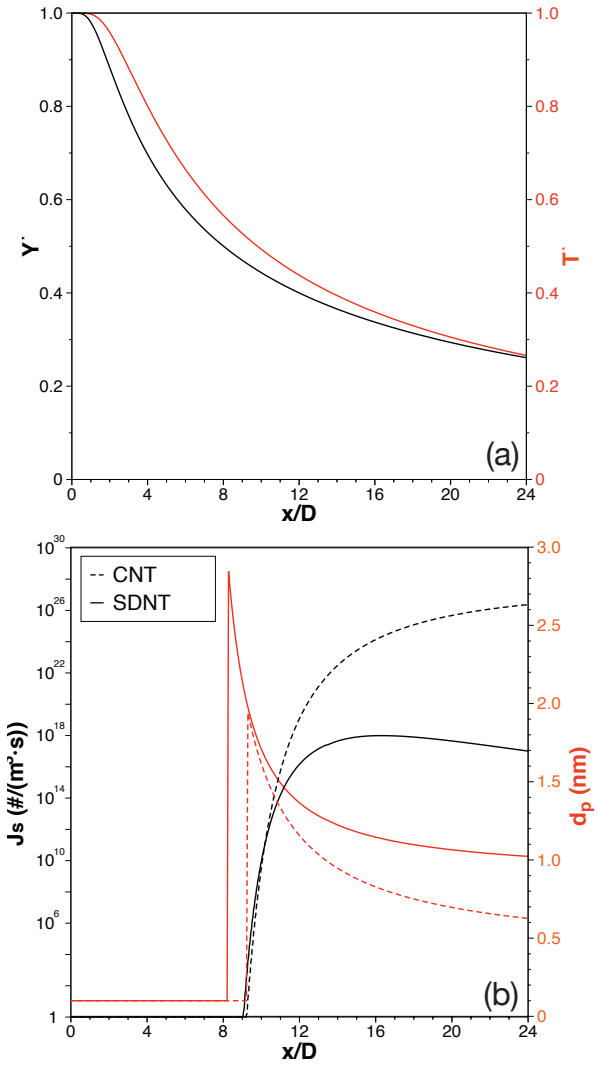

Figure B.5: Trajectory of fluid element at the center of the jet for lithium nucleation: (a) normalized vapor mass fraction $Y^\star$ and temperature $T^\star$; (b) nucleation rate J_s and critical diameter d_p.

Appendix C

Non-dimensionalization

The governing equations in all simulations are non-dimensionalized to simplfy the analysis.

$$x_i^\star = \frac{x_i}{L_o},\ \ u_i^\star = \frac{u_i}{U_o},\ \ \rho^\star = \frac{\rho}{\rho_o},\ \ Y^\star = \frac{Y}{Y_o},\ \ \rho_i^\star = \frac{\rho_i}{\rho_{io}},\ \ \sigma^\star = \frac{\sigma}{\sigma_o}, \tag{C.1}$$

where L_o is the reference length scale, U_o is the reference velocity, ρ_o and ρ_{io} are the reference density for the fluid and resultant particles, respectively. Y_o is the reference value of condensing vapor mass fraction, and σ_o is the reference value of condensing material's surface tension.

The flows under consideration are governed by the compressible Navier-Stokes equations. The primary variables are the non-dimensional fluid density $\rho^\star(\vec{x^\star})$, velocity $u_i^\star(\vec{x^\star})$, pressure $p^\star(\vec{x^\star})$, and the enthalpy $h^\star(\vec{x^\star})$, which are obtained by

$$\frac{\partial \rho^\star}{\partial t^\star} + \frac{\partial \rho^\star u_i^\star}{\partial x_i^\star} = 0, \tag{C.2}$$

$$\frac{\partial \rho^\star u_i^\star}{\partial t^\star} + \frac{\partial \rho^\star u_i^\star u_j^\star}{\partial x_j^\star} = -\frac{\partial p^\star}{\partial x_i^\star} + \frac{\mu^\star}{Re_o}\frac{\partial \tau_{ij}^\star}{\partial x_j^\star}, \tag{C.3}$$

$$\frac{\partial \rho^\star h^\star}{\partial t^\star} + \frac{\partial \rho^\star u_j^\star h^\star}{\partial x_j^\star} = \frac{\mu^\star}{Re_o Pr}\frac{\partial^2 h^\star}{\partial x_j^\star \partial x_j^\star}, \tag{C.4}$$

where $\tau_{ij}^\star$ is the viscous stress tensor for Newtonian fluid.

The non-dimensionalization of the mass conservation equations for the condensing vapor is given by

$$\frac{\partial \rho^\star Y_i^\star}{\partial t^\star} + \frac{\partial \rho^\star u_j^\star Y_i^\star}{\partial x_j^\star} = \frac{\mu^\star}{Re_o Sc}\frac{\partial^2 Y^\star}{\partial x_j^\star \partial x_j^\star} + \dot{\omega^\star}, \tag{C.5}$$

where $\dot{\omega^\star}$ is the source term representing phase conversion between vapor and particles via nucleation.

Generally we have

- $Re_o = \frac{U_o L_o}{\mu_o}$ is the reference Reynolds number;
- $Pr = \frac{\mu C_p}{k}$ is the Prandtl number;
- $Sc = \frac{\mu}{\rho D_o}$ is the Schmidt number of condensing species;
- $Le = \frac{k}{\rho C_p D_o} = \frac{Sc}{Pr}$ is the Lewis number of the condensing species.

where k is the coefficient of thermal conduction, C_p is the specific heat at constant pressure, D_o is the mass diffusivity, μ is the viscosity.